Control of Network Topology in Photopolymer Networks for Additive Manufacturing

by

Ke Qin

B.S. Chemistry, Tsinghua University (2016)

Submitted to the Department of Chemistry
in Partial Fulfillment of the Requirements for the Degree of
Doctor of Philosophy in Chemistry

at the

MASSACHUSETTS INSTITUTE OF TECHNOLOGY

February 2022

Signature of Author:

_____

Department of Chemistry
January 18, 2022

Certified by:

_____

Jeremiah A. Johnson
Professor of Chemistry
Thesis Supervisor

Accepted by:

_____

Adam P. Willard
Associate Professor of Chemistry
Graduate Officer

This doctoral thesis has been examined by a committee of professors from the Department of Chemistry as follows:

Professor Timothy M. Swager:

_____

Thesis Committee Chair

Professor Jeremiah A. Johnson:

_____

Thesis Supervisor

Professor Timothy F. Jamison:

_____

Thesis Committee Member

Control of Network Topology in Photopolymer Networks for Additive Manufacturing

By

Ke Qin

Submitted to the Department of Chemistry on Jan 25, 2022
in Partial Fulfillment of the Requirements for the Degree of Doctor of Philosophy in Chemistry at the Massachusetts Institute of Technology

Abstract

Chapter 1. The introduction provides an overview of additive manufacturing as well as the material systems and photochemical processes that enable additive manufacturing. An emphasis is placed on work done to regulate free radical polymerization via addition-fragmentation chain transfer (AFCT) and reversible addition-fragmentation chain transfer (RAFT), and their applications in photopolymer networks to improve material properties and introduce novel functional materials to additive manufacturing.

Chapter 2. In this work, we incorporate a RAFT agent into a crosslinker to make chain-transferring crosslinkers, or Transferinkers, and investigate their effect on photopolymer networks. Transferinkers were shown to improve the tensile toughness of acrylic photopolymer resins by up to 100% without incurring significant loss in strength. In addition, we exploited the unique reactivity of the RAFT agent to induce accelerated degradation of the thermoset acrylic network. Reduction in kinetic chain length caused by transferinkers is observed experimentally and in simulations. As such, transferinkers are shown to be an effective and translatable strategy for developing sustainable photopolymer networks with improved mechanical properties.

Chapter 3. We report the isolation and structural elucidation of 3,3,8,8-tetramethyl-1-oxa-4,6,9-trithiaspiro [4.4] nonane-2,7-dione, an unexpected product obtained during the synthesis of functionalized trithiocarbonate RAFT agents. A spirocyclic structure was proposed, and confirmed with X-Ray crystallography. This molecule can undergo ring opening when treated with a nucleophilic amine to form a trithiocarbonate, which can be used to mediate RAFT polymerization. Potential applications in synthesizing polymers with defined head groups are also explored.

Chapter 4. We report a new class of supramolecular polymer metal-organic cage (polyMOC) gels based on the assembly of $Cu_{24}L_{24}$ cuboctahedra. We demonstrate how these polyMOCs can be reversibly photoswitched between three oxidation states (Cu(II), Cu(I), and Cu(0)) that each give rise to unique properties. Cu(II) polyMOC can also be applied to direct ink writing (DIW) 3D printing. Cu(II) polyMOC containing polymeric azides and alkynes precursors can be extruded, where the mechanically robust polyMOC serves as a template. Subsequent photoswitching to the Cu(I) state crosslinks the precursors and re-oxidation provides MOC-interpenetrating networks (MINs). In addition, the Cu(II) polyMOC can be completely removed with competing ligands to expose the nascent covalent network.

Thesis Supervisor: Jeremiah A. Johnson

Title: Professor of Chemistry

Acknowledgements

I'd like to start by thanking my Ph.D. Advisor, Professor Jeremiah Johnson for his advice and support for my pursuits over graduate school, as well as care and patience of my shortcomings. Jeremiah's contagious enthusiasm and optimism has urged me on when I am down or in doubt, and I am grateful for his emphasis on sharing his enthusiasm for science and trying to make his group an enjoyable experience as much as possible for all. Words cannot describe how fortunate I feel to have him as my advisor.

My thanks to my thesis committee chair, Professor Timothy Swager, and my thesis committee member Professor Timothy Jamison, for their support and guidance.

My thanks also go to the MIT faculty I had the fortune to learn from and interact with. To Prof. Robert Cohen for running one of the most beginner-friendly polymer physics classes I have had and being responsible for most of the things I know about polymers physics. To Prof. Darrell Irvine and Prof. Alfredo Alexander-Katz, for their care and leadership as head of the PPSM program. Prof. Katharina Ribbeck, Prof. Bradley Olsen, and Prof. Jeffrey Van Humbeck for their guidance.

To Shannon Wagner, Brian Pretti and Eric Vandenburghe for keeping everything running smoothly. To Rebecca Teixeira and Jennifer Weisman at the Chem Ed Office for always being there to help. To John Grimes, Dr. Walt Massefski, and Dr. Bruce Adams at the DCIF for always being knowledgeable and helpful with instrumentation. And to Gang Liu, whom I admire for his unique knowledge and creativity in repairing just about anything.

Being part of the Johnson group gave me the opportunity to work with some of the Dr. Jessica Lamb and Dr. Bin Liu who closely mentored me through the increasingly stressful later years of grad school, in science, career and life. Their knowledge, care and leadership helped me grow as a scientist. I have no doubt they will go on to be great advisors to students. To Dr. Chris Brown for all the chemistry and camera talk, to Dr. Manuel Hartweg for all the hikes and bike rides and his raw enthusiasm; his mere presence cheers me up. To Dr. Nate Oldenhuis for his beaming optimism and his ability to always find the funny side of things. To Dr. Samantha Kristufek for always being considerate. To Dr. Matt Golder for his steadfast leadership in the upkeep of the lab. To Dr. Bo Qiao for teaching me DFT and letting me pet his cat. (To the Snow the cat) To Dr. Farrukh Vohidov for introducing me to the gym. To Dr. Eileen Burke for all the flow chemistry talk. To Dr. Junpeng Wang for bringing Ellery to lab who was the source of joy for everyone. To Dr. Gavin Kiel for always being in the basement late night when I go check on the GPC. And to Dr. Wenxu Zhang, Dr. Mingjun Huang, Dr. Megan Hill, Dr. Elisabeth Prince, Prof. Ellane Park,

Dr. Yoshiki Shibuya, Dr. Xiaojuan Liao, Dr. Sipei Li, and Dr. Peyton Shieh for their friendship and assistance.

My thanks to Deborah Ehrlich for her incomparable kindness and generosity, and being someone I feel I could always look up for advice and support. To Dr. Yuwei Gu for always having an insightful response for science questions. To Dr. Hung Nguyen for all the chats, chemistry and else, over fried chicken. To Dr. Yivan Jiang for showing me how to do things properly when I started out. To Dr. Julia Zhao for alpha testing my printed violins and all the cat memes and grad-school-late-night struggle sessions. To Dr. Ken Kawamoto, whose hood I inherited, for the noir comic strips on the sash. To Dr. Michelle Macleod for her candor.

And to whomever it was that drew Professor Snape on the basement lab window.

To Wencong Wang for writing a Chinese scroll on my hood sash (which translates into: Hard work from morning into night; Many papers as spring turn into autumn). To Sachin Bhagchandani for all the meals at dining halls and Matthew Pearson for all the political debates. To Allie Sourakov for showing me the hidden gems on MIT's campus, and for encouragements on all the random and interesting things to try. To David Lundberg for coming up with creative decorations in lab and office. To Michael Stolberg for keeping the lab safe. To Landon Kilgallon and Martin Henriksen for quality time spent digging through electronics waste. To Keith Husted for always being a great party host. To Abraham Herzog-Arbeitman to alpha testing my printed cello. To Leticia Costa and Alayna Johnson for joining me in the fun and intense hobby of GPC fixing. And best of luck as well. To Aiden Wang for taking over the mantle of 3D printers to which I also feel personally attached. To Yasmeen Alfaraj for being a caring friend and the shared interest in machine learning. To Hadiqa Zafar for the intriguing murals by the prep-GPC and dissipating my ignorance of Drake. And to Khrystofor Khokhlov, Valerie Lensch, Zehao Sun, Julian Grundler, Lori Won, and Foli Amazio.

To people outside the Johnson group whom I worked with: To Dr. Weizhong Zou and Prof. Brad Olsen for assisting with computations. To Dr. Saswata Chakraborty, Dr. Guy Joly and Dr. Cathy Bothof at 3M for supporting my project financially and intellectually. To David Ibbett, Prof. Steven Craig and all the MONET Art of Polymers crew for making this concert happen and giving me the opportunity to build and showcase a printable cello.

To Celestine Hong and Shayna Hilburg for sharing the PPSM office in the first year and all the random jokes cracked then and since. To Josh Kubiak for being the superstar at organizing everything and having a Pusheen gif for every occasion. To Yanpu He for the sailing sessions.

To MITOC and MITFC for giving me the opportunity to make friends on trails and in hangars with some of the most interesting people I know. And the opportunity to see the world from very different perspectives: high above and… high above.

I am thankful for Prof. Xi Zhang and Prof. Yan-Mei Li at Tsinghua University who gave me the opportunity to be part of their labs and learn more about their research projects, and for Prof. Jeffrey Moore at University of Illinois at Urbana-Champaign for the opportunity to visit his lab in summer 2015. I value these experience as they have all shaped my path forward. I would also like to thank Dr. Zehuan Huang, Yunhao Bai, Dr. Timothy Moneypenny and Dr. Yang Song for their mentorship and friendship.

I want to close by thanking my parents, Prof. Chuanguang Qin and Yan Ding, for everything. I could not be where I am today if not for their love and sacrifice.

Preface

The thesis has been adapted from the following articles co-written by the author:

Peer-reviewed:

Oldenhuis, N. J.; **Qin, K. P**.; Wang, S.; Ye, H.; Alt, E. A.; Willard, A. P.; Van Voorhis, T.; Craig, S. L.; Johnson, J. A. Photoswitchable Sol–Gel Transitions and Catalysis Mediated by Polymer Networks with Coumarin-Decorated $Cu_{24}L_{24}$ Metal–Organic Cages as Junctions. *Angew. Chemie Int. Ed.* 2020, 59 (7), 2784–2792.

In preparation:

Qin, K. P.; Zou, W.; Chakraborty, S; Kristufek, S.L.; Husted, K.E.L; Joly, G.D; Olsen, B.D; Johnson, J. A. Trithiocarbonate-Bearing Crosslinkers for Tough and Degradable Photopolymer Networks. *In preparation*.

Qin, K. P.; Brown, C. M.; Wang, W.; Liu, B.; Johnson, J. A. On-Demand Control of Polymerization with a Novel Trithiocarbonate Precursor. *In preparation*.

Respective contributions

This thesis describes work that resulted from collaborative efforts of the author with other colleagues at MIT. The specific contributions of the author and collaborators are delineated below.

Chapter 1. The introduction is written by the author.

Chapter 2. Work presented in Chapter 2 was performed by the author.

Chapter 3. Work presented in Chapter 3 was a collaborative effort between the author and Dr. Chris M. Brown. Dr. Chris M. Brown obtained the single crystal of the 3,3,8,8-tetramethyl-1-oxa-4,6,9-trithiaspiro [4.4] nonane-2,7-dione and the crystallographic data.

Chapter 4. Work presented in Chapter 4 was a was a collaborative effort between the author and Prof. Nathan J. Oldenhuis. Prof. Nathan J. Oldenhuis prepared and characterized the gels. The author scaled up material synthesis, modified the 3D printer and adapted the gel to 3D printing.

Table of Contents

Chapter 1 Introduction: Application of Addition-Fragmentation Chain Transfer (AFCT) in Additive Manufacturing

1.1 A general introduction to Additive Manufacturing

Additive manufacturing (AM), or more colloquially known as 3D Printing (3DP), has in the recent decade emerged from a specialized tool for prototyping into a versatile platform for rapid manufacturing of functional objects. AM allows for fast transformation of digital models into real-world, functional objects, made of polymers, ceramics and metals, without the need for overheads like molds or jigs that are necessary for conventional means of fabrication. The original advantage of AM was its ability to manufacture parts with little to no lead time, simplifying logistics and reducing supply chain dependency. More recently, AM processes have also been used for their own unique advantages, such as in the production of parts with complex geometries inaccessible to other means of manufacturing, or the fabrication of objects with multiple materials[1–3] or even continuously varying material properties.[4]

AM is defined in relation to "subtractive" means of manufacturing such as machining and sculpting, and "formative" means of manufacturing, such as casting and injection molding.[5] In subtractive manufacturing, material is successively removed from a matrix to form a new part of desired geometry; with formative manufacturing, some kind of mold is required (usually made from subtractive manufacturing) to cast a molten material into shape. In contrast, additive manufacturing processes successively apply material to a matrix, usually in a layer-by-layer fashion, until the desired geometry is achieved.

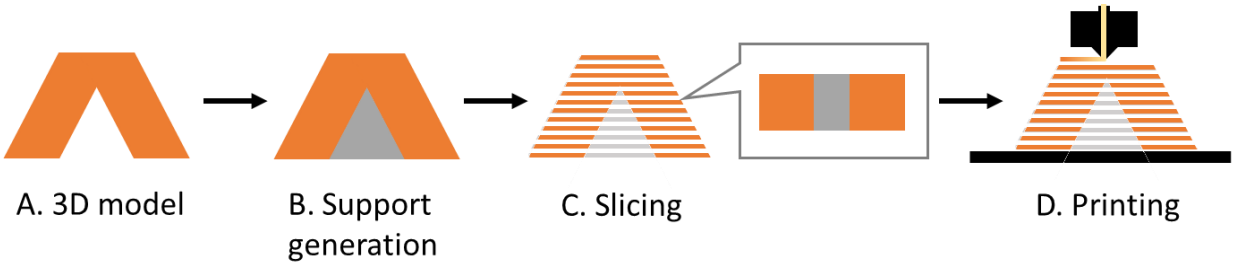

Figure 1-1 Schematic showing the general workflow in AM. A) 3D model to be printed. B) Generation of support structures where necessary. C) Slicing, or processing the 3D model into layer-by-layer instruction for the printer. Inset shows individual layer. D) The printer prints the model according to the instruction.

AM translates digital models into real-world objects (**Figure 1-1**). The first step is always "Slicing", or the processing of a 3D model into 2D slices for layer-by-layer processes. The 2D slices are then further processed into specific instructions for the printer, such as toolpaths. In many newly introduced AM processes that deviate from the layer-by-layer paradigm,[6] the process is still called "slicing".

Due to the layer by layer nature of most additive manufacturing processes, they work best when each layer is completely supported by the layer below. A pyramid, for example, is extremely easy to print. However, it is difficult, if not impossible, for most AM processes to print in mid-air. In models with complex geometric shapes, some geometries are translated into features that are more difficult to print than others. To validate a printing process to be useful in a variety of applications, benchmark parts are often designed that encompass a wide range of features (**Figure 1-2**).[7]

An overhang is a common feature encountered in AM where an edge or surface on the object is angled so layer above is larger than the layer below (**Figure 1-2**). In some cases, the overhanging part tends to sag down due to gravity as it is not completely supported, but in some cases the overhanging part tends to curl up. In processes involving melting (such as Fused Deposition Modelling[8] and Selective Laser Sintering[9]) this is driven by the thermal contraction of the material as it cools down. In photopolymer-based processes, it is often driven by polymerization-induced shrinkage in (meth)acrylic systems commonly used in these processes[10]. Most processes have a threshold overhang angle which defines the shallowest overhang that can be printed without the need for support structures.

Another feature commonly found in AM is a bridge, in which the layer above hangs over a gap in the layer below, but is supported on both ends (**Figure 1-2**). Although bridges are technically 90° overhangs, many processes can print some bridges without support structures as both ends of the bridge are supported, and the same issues that cause overhangs to curl up (such as thermal contraction) actually provides tension on the bridge to counteract sagging.

Clever design and orientation of the model can often minimize the amount of difficult features encountered, but in some cases it is unavoidable that part of the model has no connection

whatsoever to the build substrate or other parts of the model. Therefore, support structures are used to provide structural support for these parts during the print, similar to how scaffolding is used in construction. Support structures are also used for shallow overhangs and long bridges to prevent sagging and curling. Support structures can be built into the model during design, but in most cases they are automatically generated during slicing. They can be printed using the same material as the model, and are designed to have minimal contact with the model so they can be easily broken off with a little force post-print. In more advanced printers that are capable of printing more than one material, support structures are often printed with a soluble material to facilitate the removal process.

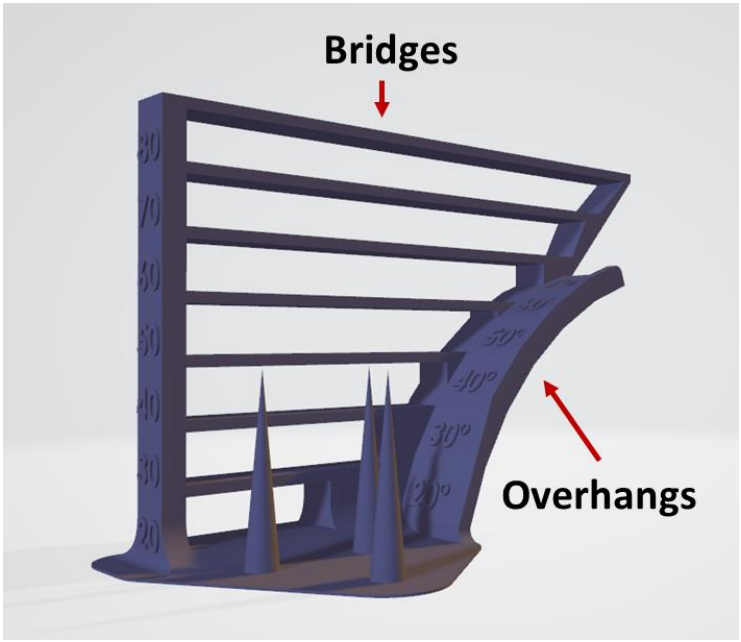

Figure 1-2 A benchmark model showing bridge and overhang features.[11]

In most AM processes a post-processing step is necessary after printing to obtain a functional part.[12–16] This may involve removing of support material, thermal treatment and/or surface treatment. In many AM processes, conditions optimized for printing a part within a reasonable timeframe is often not optimal for maximizing the mechanical potential of the material being printed. This can sometimes be rectified in post processing. For example, most metal AM processes call for an annealing process. Post processing also allows a different set of conditions to

be applied to the part (e.g. heat vs. light) over longer periods of time so more complex reactions can take place. In more and more cases, the initial printing step is used only to form a scaffold to maintain the geometry of the part, and most of the material property is dictated by post processing. More complex material systems can be programmed to change their shapes in response to new stimuli introduced in post-printing processes, leading to a related field known as "4D printing". [17–19]

1.1.1 AM processes and their variations

There is a huge and growing variety of methods to realize AM and there is no universally agreed upon standard to categorize them. In the interest of focus, an emphasis will be put on AM processes that involve photopolymerization.[20] An interesting phenomenon in the field is that each minute variation of AM technologies has one or more acronyms. For example, Fused Deposition Modelling (FDM),[8] Fused Filament Fabrication (FFF)[21], and Plastic Jet Printing (PJP)[22] are used by different groups but refer to essentially the same technology. While it is understandable for reasons related to intellectual property and marketing, it does introduce unnecessary complications and confusion.

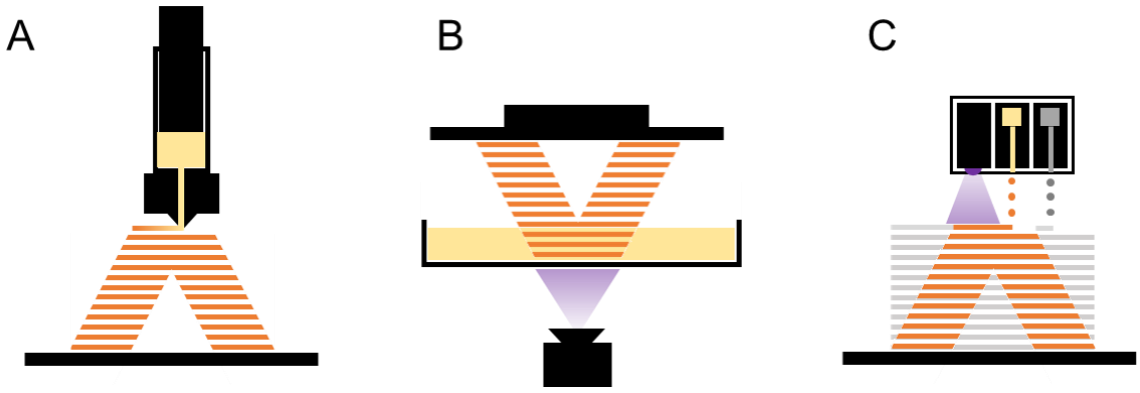

Figure 1-3 Schematic demonstration of the working principle of select AM processes. A) Material extrusion; B) Vat photopolymerization (Digital light processing); C) Material jetting.

1.1.1.1 Material extrusion

In a material extrusion 3D printer, material is fed into a nozzle and deposited in a layer by layer fashion (**Figure 1-3**A).[5] The position of the nozzle is controlled by a mechanical motion system. Material extrusion is the simplest and currently the most prolific form of AM. Material extrusion printers have been adapted to print a wide variety of materials, from thermoplastic polymers to hydrogels to concrete.[23,24] By switching between different material feeds, parts made from multiple materials can be printed. However, despite significant improvements in print quality and resolution afforded by advancements in hardware and software, material extrusion printers in general lag in these regards compared to other methods to be introduced later.

As precise linear actuation (with resolution as low as 0.05mm) can be achieved with inexpensive and readily available parts such as stepper motors, timing belts, and threaded rods, material extrusion 3D printers with reasonable precision can be built with little to no specialized knowledge or custom hardware.[25] The wide availability of user-friendly single board computers (SBCs) such as Arduino and Raspberry Pi in recent years has made it possible to achieve better print quality without resorting to more expensive hardware by overcoming mechanical deficiencies such as misalignment and vibration through software correction.[26,27]

Another key aspect of material extrusion printing is the process of material extrusion itself.[28,29] The material needs to flow through the nozzle in a reasonable timescale, and then gain enough strength to maintain its shape once out of the nozzle.[30] This can be accomplished in a variety of ways, which also differentiates the variations among material extrusion printers.

1.1.1.1.1 Fused deposition modelling (FDM)

Although the FDM process does not usually involve photopolymerization, it deserves mention here as it is currently by far the most popular and well-known form of 3D printing.[5,8] FDM printers use thermoplastic polymers that are fed into a heated nozzle, melted, and deposited. Once out of the nozzle, the thermoplastic cools down and solidifies. The vast majority of FDM printers take

raw material in the form of filaments ranging in diameter from 1.75 mm to 3 mm, but examples are known that use other feed such as pellets. [31]

A variety of commercial thermoplastic material can be used. Acrylonitrile butadiene styrene (ABS) was adopted first, but material such as (polylactic acid) PLA and (polyethylene terephthalate glycol) PETG that are easier to print (due to having lower thermal expansion constant) quickly gained popularity. Other thermoplastics such as acrylonitrile styrene acrylate (ASA), polyvinyl alcohol (PVA), Nylon 12, high-density polyethylene (HDPE), polypropylene (PP) are also amenable to this approach.

1.1.1.1.2 Direct Ink Writing (DIW)

DIW is a broad term used to define a wide range of material extrusion processes that are not FDM. Typically, in a DIW process, the raw material (ink) is loaded in syringes and mechanically extruded through a nozzle. [32]

DIW places unique requirements on the ink material: 1) The viscosity needs to be low enough for successful extrusion; 2) The material needs to rapidly gain mechanical strength upon extrusion to maintain its extruded shape, either through a rapid increase in viscosity or a sol-gel transition; 3) The mechanical and chemical properties of the material should be easily tunable via formulation or chemical modification to enable a range of desired applications. Such requirements limit the scope of materials amenable to 3D printing.[33] The need for low viscosity precludes the extrusion of permanently crosslinked materials, as they would fracture instead of flow in response to the shear forces present during extrusion. In addition, not all transiently crosslinked materials can regain viscosity rapidly enough to maintain their shapes after being extruded. DIW is uniquely suited to printing a variety of hydrogel-based materials as it can deposit materials in very mild conditions (ambient temperature, low shear, aqueous matrix, low or low intensity irradiation, etc.) compared to other processes.[34,35] Therefore, it has often been employed in the 3D printing of biomaterials, in which case it is often called bioprinting.[36–38]

1.1.1.2 Vat photopolymerization

In essence, vat photopolymerization involves a tank (or "vat") of liquid photopolymer resin and a patterned light source (**Figure 1-3**B). The light source selectively irradiates part of a thin layer of the photopolymer resin in the tank, causing it to cure into an insoluble solid. A mechanical build platform then moves the cured layer away from the interface to expose a fresh layer of uncured photopolymer to irradiation. The process is repeated through the entire height of the part.

Printers that utilize vat photopolymerization can be generally divided into two categories depending on the orientation of the printed model. In "upright" machines, the light source is placed above the tank the model is printed upright. Polymerization takes place at the resin-air interface, as the printed model is gradually lowered into the resin tank (**Figure 1-4** A). While conceptually and mechanically simple, these machines require excess amount of resin as the entirety of the model needs to be submerged. As such, this kind of design in found in older and large scale printers. In "inverted" machines, the bottom of the resin tank is a transparent window and the light source is placed underneath the tank (**Figure 1-4** B and C). Polymerization takes place at the window-resin interface. The model is printed upside down and gradually lifted up out of the resin tank, which means the resin tank no longer has to submerge the model, thus only has to hold resin equivalent in volume to the model, allowing machines with smaller footprint to be built. As polymerization takes place at the window-resin interface, care must be taken to prevent the cured photopolymer from fusing with the window. Most commercial machines still employ some kind of mechanical "peeling" process to ensure separation of the cured part from the window. In some machines, a glass window is used with polydimethylsiloxane (PDMS) coating.[39,40] In recent years, fluorinated ethylene propylene (FEP) membranes have become the material of choice for the window.[41] FEP allows diffusion of air from the outside into the tank, creating a thin "dead zone" where the oxygen concentration inhibits polymerization and shifting the polymerization interface away from the window.[42] While the application of FEP membranes has made the peeling process much more simple and reliable, machines using FEP membranes as the window material are limited in build volume as larger FEP membranes require more tension to prevent flexing, and limited in speed as FEP membranes cannot efficiently dissipate heat generated at the printing

interface. To address these limitations, machines using a liquid immiscible with the photopolymer resin as the interface material have been described in literature.[43,44]

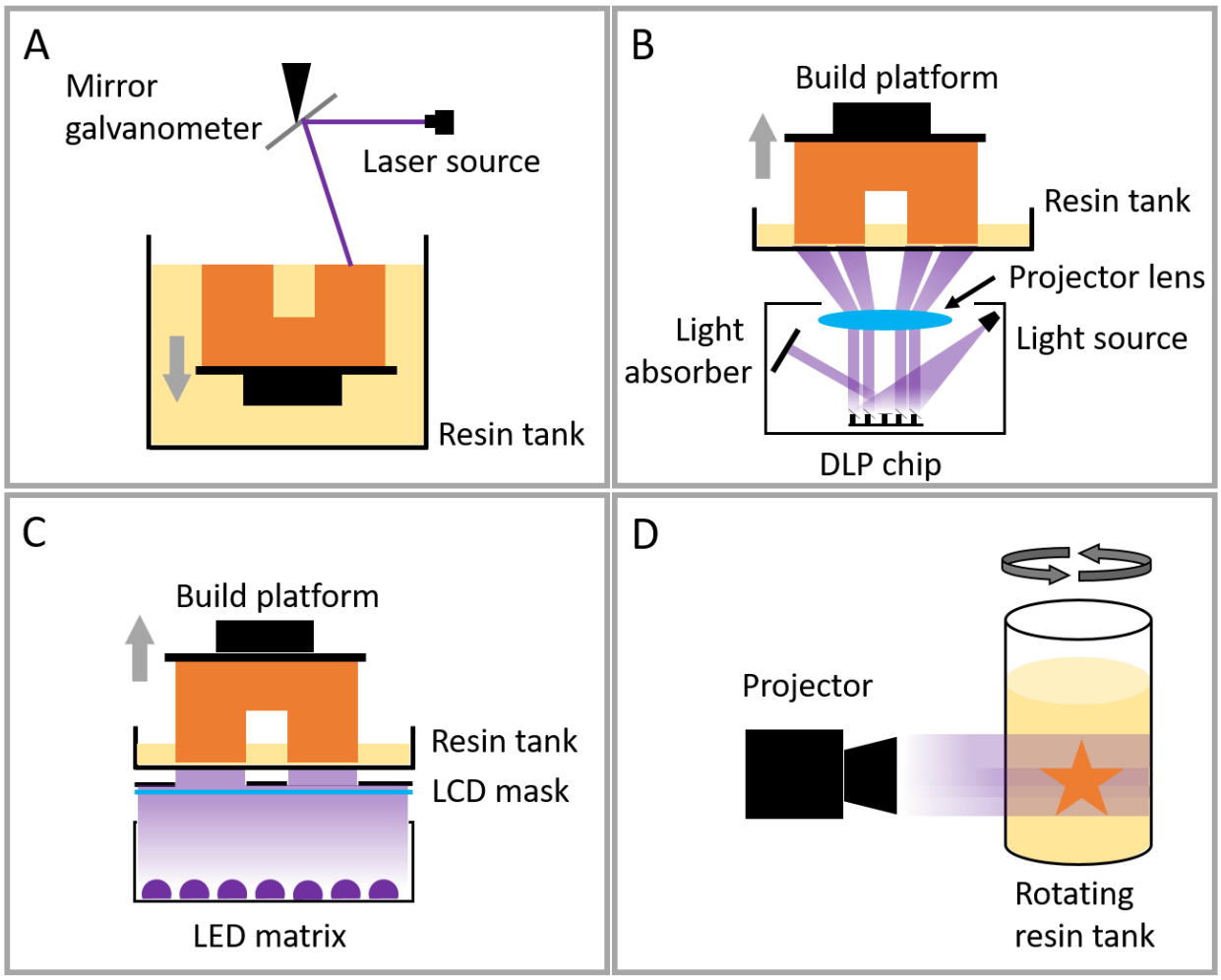

Figure 1-4 Schematic demonstrating the working principles of different variations to vat photopolymerization. Grey arrows indicate the movement of the build platform as printing progresses. A) Stereolithography (SLA); B) Digital light processing (DLP); C) Masked SLA (MSLA); D) Computed Axial Lithography (CAL)

Many vat photopolymerization processes are capable of achieving much higher resolution compared to material extrusion processes such as FDM.[5,45] Some variants have even become

affordable enough to rival FDM systems. One inherent weakness of vat photopolymerization is that it is very difficult to achieve multimaterial printing, as the entire process takes place in a homogenous resin bath. Other limitations include limited build volume, and material properties that still fall short of thermoplastics.

There are many variations to vat photopolymerization, mostly related to the variation in light source, which will be introduced below.

1.1.1.2.1 Stereolithography (SLA)

Originally named "Rapid Prototyping"(RP) in the 1980s, SLA is the first kind of additive manufacturing to be developed.[46] The acronym SLA stands for Stereo Lithography Apparatus, derived from the first 3D printer prototype. In SLA machines, a laser is paired with a mirror galvanometer to create a point of light on the polymerization interface that renders 2D patterns in each layer via raster scanning (**Figure 1-4** A). SLA machines can be scaled without sacrificing resolution as the size of the light dot remains the same, however its print speed is dependent upon the size and complexity of the model. As the light point has to "draw" the 2D slice on every layer, larger and geometrically complex parts take longer to print.

1.1.1.2.2 Digital light processing (DLP)

DLP 3D printers use a projector as their light source and derive their name from the DLP projectors that they use.[47] DLP projectors use a DLP chip, which contains an array of small mirrors to reflect or deflect light from a lamp to create an image with light or dark pixels on the polymerization interface (**Figure 1-4** B).[48] In contrast to SLA printers, DLP printers spend the same amount of time on each layer regardless of size and complexity, as the entirety of the 2D slice is generated simultaneously. The resolution of DLP prints is limited by the projector as it only provides a finite amount of pixels. The larger the print volume, the bigger the pixels, the lower the resolution.

Continuous liquid interface polymeration[42] (CLIP, and its commercial name, Digital Light Synthesis or DLS) is a variation of DLP which takes the full advantage of the dead zone provided

by the FEP windows and eliminates the peeling process. This allows the model to be sliced into more and thinner layers without a penalty in print time. Pushed to the extreme, it allows continuous layer-less printing, where the 2D light pattern is updated and the build platform is raised in a continuous, stepless fashion. This process greatly increases print speed and mitigates issues as layer lines and anisotropy that are associated with a layer-by-layer process.

1.1.1.2.3 Masked SLA (MSLA)

MSLA printers uses a backlight and a light mask to generate a 2D pattern, similar to a backlit LCD screen. In fact, the light source in most MSLA printers are LCD screens with their backlight removed and replaced with a powerful matrix of LED lamps. As such, they are also called LCD printers (**Figure 1-4** C). MSLA printers shares similar pros and cons with DLP printers: their speed is not affected by the size and complexity of the model, and their build volume and resolution are limited by the LCD panels available. As these printers can be built with relatively inexpensive and widely available parts, they have drastically reduced the barrier of entry to vat photopolymerization, and have been immensely popular among artists, makers, and researchers.

1.1.1.2.4 Computed Axial Lithography (CAL)[49]

CAL is unique in that it is not a layer-by-layer process. In a layer-by-layer process, layers comprise 2D exposures. In contrast, the CAL process creates a volumetric 3D exposure inside the resin volume by projecting intensity-modulated light from different angles (**Figure 1-4** D). The superposition of these light projections results in a 3D region in the resin volume where the aggregated light intensity is sufficient to induce crosslinking and gelation. This process has the potential to be faster than conventional layer-by-layer processes and eliminate the need for support structures. However, light penetration depth and diffusion issues limit the print volume, and current computational algorithms cannot guarantee that an exposure solution can be generated for all geometric shapes.

1.1.1.2.5 Two-photon Polymerization (2PP)

Two-photon polymerization[50,51] exploits two-photon absorption (TPA), a process in which two photons are absorbed simultaneously. In contrast with normal, "one-photon" processes in which the probability is directly related to light intensity, the probability of TPA is proportional to the square of light intensity.[51,52] If a beam of light is focused into a point in a volume of resin, conventional photopolymerization takes place at all depths where there is light penetration, whereas 2PP only takes place near the focal plane where light intensity is high enough. This allows for precise control in the Z axis by controlling the focal plane of the optical system. The same principle is used in microscopes to achieve resolution below the diffraction limit and Z-axis resolution.

As 2PP only takes place in a very small volume, it is capable of achieving sub-micron resolution. In return 2PP processes are usually confined to very small build volumes no more than a few millimeters in dimension. Combined with the requirement for very high intensity lasers to produce the light intensity needed for TPA, 2PP is limited to a number of niche applications.[53–56] However, recent reports[57] of using triplet-triplet annihilation (TTA) instead of TPA as the upconversion process has shown potential to drastically lower the requirement for light intensity, opening up the possibility of using 2PP to print macroscale objects.

1.1.1.3 Material jetting

As its name implies, material jetting employs an inkjet printhead similar or identical to those found in color printers (**Figure 1-3** C).[38] A printhead contains an array of hundreds of nozzles tens of microns in diamater. Each nozzle is individually controlled by a piezo or a heating element that forces the ink out in droplets when turned on. In a material jetting process, the raw material itself, usually a photopolymer or a wax or a mix thereof, is jetted from the printhead. 2D patterns are created in an identical fashion to printing on paper. The printhead is equipped with a UV lamp to cure the photopolymer in place, and 3D objects are printed in a layer-by-layer fashion. By combining multiple printheads jetting different inks, multi-material or even gradient material printing can be achieved. Due to the low viscosity of the inks typically used in this process, no

overhang or bridge is possible without a support material. The support material is usually a wax that can be melted or dissolved away.[5]

Material jetting is capable of achieving precision and resolution that equal or exceed that of vat photopolymerization processes, while being able to print multiple or gradient material. However, it is currently limited by the fact that inkjet printheads are expensive to manufacture, the complexity of components involved, and the stringent requirements they put on ink development, among which is the need for very low viscosity inks, much lower than that required by vat photopolymerization or DIW. As a result, material selection and material properties for this process still leave much to be desired.

1.2 Material systems used in AM processed based on photopolymerization

Polymer resins that cure in response to light are called photopolymer resins or photopolymers. More fundamentally, the curing process is the joining of individual molecules, or crosslinkers, in the resin into a network. This can be done by using light to induce individual reactions between crosslinkers via photochemical reactions such as photocycloadditions[58]. However, for purposes of AM it is much more preferable to use light to initiate a chain reaction or activate a catalyst that can mediate multiple crosslinking reactions, as it is generally much faster and requires less intense light sources. Photoinitiated free radical polymerization, therefore, is the most commonly used system in photopolymer resins in AM.[59]

1.2.1 Free radical polymerization(FRP)

Most radical photoinitators rely on Norrish reaction of ketones and can therefore be generally classified as Type I or Type II. Type I photoinitiators are single component systems in which the excited photoinitiator molecule undergo homolytic cleavage into two radicals (**Figure 1-5** A). Examples of such photoinitiators are benzyl ketal derivitives and acyl phosphine oxides (such as TPO and BAPO).[5]

Type II photoinitiation systems are two component systems compose of a photoinitiator that absorbs the light and a co-initiator or a hydrogen donor (**Figure 1-5** B). The excited photoinitiator abstracts a hydrogen atom from the co-initiator, resulting two radicals.[60] As the ketone radical is resonance stabilized, the radical on the co-initiator is typically the one that initiates polymerization.[61–63] An example of a Type II system involves benzophenone as the photoinitiator and ethyl-4-(dimethylamino)benzoate (EDMAB) as the co-initiator. Tertiary amines are efficient co-initiators, although in radical-cationic dual-cure systems they may inhibit cationic polymerization.

Acrylates are favored in AM processes due to their fast curing kinetics that gives the printed object good "green strength" to maintain its geometric shape in a short time.[5] This allows faster printing and minimizes loss of resolution due to material and light diffusion. Slower to cure, methacrylates are often used in conjunction with acrylates to mitigate shrinking and distortion.

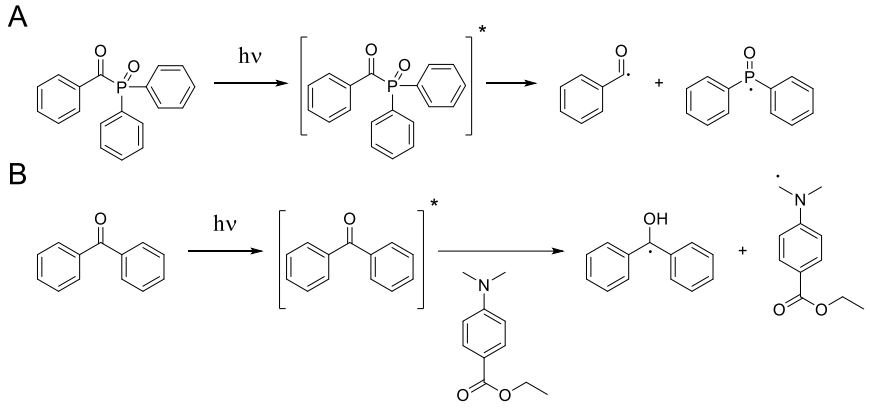

Figure 1-5 Mechanism of radical generation for A) TPO, a Norrish type I photoinitiator and B) Benzophenone and EDMAB, a type II photoinitiation system

Commercial photopolymer formulations for AM usually contain some mixture of mono- and multi-functional (meth)acrylates, urethane acrylates, and/or (meth)acrylate oligomers.[64] Crosslinkers with higher molecular weights result in polymer networks with higher molecular weight between crosslinks and more entanglements, and therefore better mechanical properties. However, higher molecular weight crosslinkers are usually too viscous for many AM processes.

Inkjets need less viscous resins than those used in vat photopolymerization, and material extrusion processes can handle even higher viscosities. High viscosity crosslinkers can be diluted with lower weight components called reactive diluents. Another way to mitigate the influence of viscosity is by heating. Advanced vat photopolymerization and material jetting machines have heating elements for their vats and nozzles, respectively, to be able to print materials with higher performance.

(Meth)acrylate photopolymers form topologically inhomogeneous networks. The high rate of propagation means that highly crosslinked nanogel fragments are formed at the beginning of the polymerization process with high contents of topological defects such as loops and intramolecular crosslinks. As the process is irreversible, when these nanogel fragments eventually crosslink with each other, these topological defects are preserved in the network.[65]

The fast gelation of (Meth)acrylate networks quickly lowers the mobility of all species in the system, leading to more network defects such as dangling chain ends and intramolecular crosslinks as the curing proceeds.[66,67] In addition, further crosslinking past gelation causes significant shrinkage in the system as the network can no longer rearrange to relax the geometric and volumetric changes brought about by the polymerization reaction.[68] In addition to geometric inaccuracies and warping of unsupported overhangs, inhomogeneous shrinkage also causes internal stress buildup in the network, further degrading its mechanical performance.

Even (meth)acrylate networks without topological defects on longer length scales are still inhomogeneous on a smaller scale. On the molecular level, (meth)acrylate networks (and indeed all networks formed via chain growth polymerization) can be considered as long vinyl backbones linked together by crosslinker molecules. In networks with high loadings of multifunctional crosslinkers, there is a crosslinking point every three carbon atoms along the polymer backbone, whereas along individual crosslinker molecules the distance between crosslinking points is the length of the crosslinker molecule, which can be ten or more carbon atoms. Therefore, the backbone is much less capable of dissipating energy than the crosslinkers, leading to brittleness of the network[5,69].

1.2.1.1 Thermoplastic systems

Most photopolymers accomplish the liquid-to-solid transition by crosslinking and forming insoluble fractions, resulting in a crosslinked, thermoset network. Tao and co-workers[70] envisaged that a fast linear polymerization system which yields high molecular weight polymers insoluble in the monomer bath can also be used for AM. They demonstrated this concept by DLP printing of linear 4-acryloylmorpholine(ACMO). As poly-4-acryloylmorpholine is soluble in water, the printed objects are also water soluble as they are not crosslinked.

1.2.2 Thiol-ene chemistry

A widely used alternative to (meth)acrylic systems is thiol-ene or thiol-yne chemistry (**Figure 1-6**).[71] Thiols can be considered as chain transfer agents in free radical polymerization, but as they attach themselves onto vinyl chains, multivinyl crosslinkers and multifunctional thiol compounds can also form a crosslinked network. [72–75]

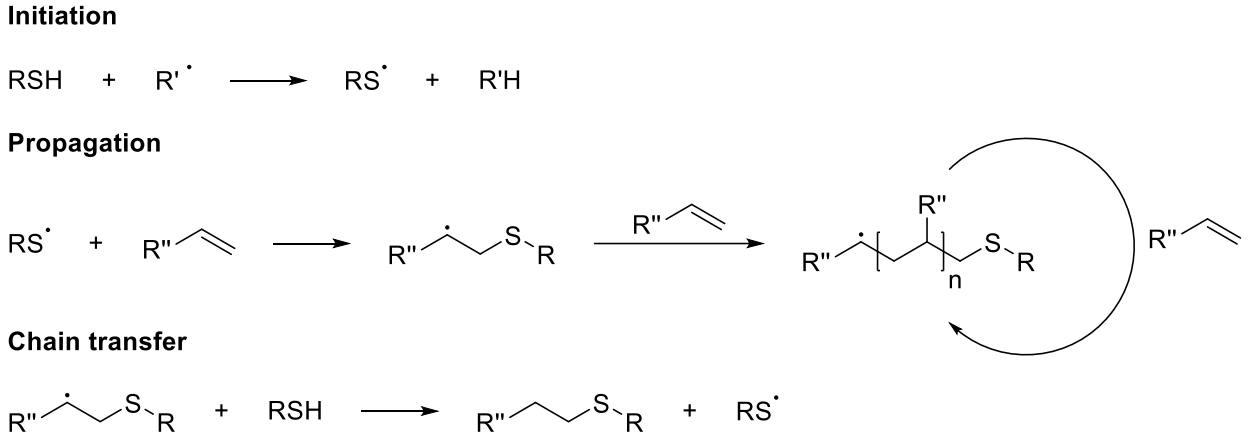

Figure 1-6 Thiol-ene reactions

The important feature of thiol-ene systems is that they are step-growth in mechanism, which has two implications. First, thiol-ene systems experience significantly less polymerization induced shrinkage than their (meth)acrylic counterparts, as the step growth mechanism shortens the kinetic chain lengths and in turn delays the gel point.[76] As the shrinkage and stress buildup occurs

primarily past the gel point, they are less prevalent in thiol-ene systems. Secondly, the step-growth-like "model network" architecture in thiol-ene networks are more homogenous and therefore more effective at dissipating stress than the ladder-like architecture of (meth)acrylic systems[69]. Therefore, thiol-ene networks tend to be less brittle than acrylate networks[77].

Another aspect of thiol-ene chemistry is its better tolerance to oxygen compared to free radical systems, which results in lower light dosage required for curing[78]. However, this also precludes its use in processes that depend on oxygen inhibition such as CLIP.

Thiol-ene chemistry is limited by the stability and odor of the thiol component, as well as its tendency to yellow over time.[79] Thiol-ene networks, while less brittle, tend to be soft due to the flexibility of the thiol linkages.[69]

1.2.2.1 Thiol-Michael addition

The anionic counterpart to thiol-ene reaction, the thiol-Michael addition reaction has also been used in the synthesis of polymer networks[80]. A thiol-Michael addition reaction is catalyzed by a base, which can be produced by a photobase generator (PBG)[81,82], making the reaction sensitive to light. While not yet realized to our knowledge, this class of reaction also has potential for application in AM.

1.2.3 Cationic polymerization

Another important system used in photopolymerization-based is cationic polymerization initiated by a photoacid generator (PAG). Monomers such as epoxides, oxetanes and vinyl ethers are commonly used.[5] While propagating radicals can be terminated by oxygen in the atmosphere, the only atmospheric component that interacts with cations is moisture, which acts not as a terminator but as a chain transfer agent.[83] Therefore, cationic systems can continue to cure after light is removed (dark cure), which can be advantageous or disadvantageous depending on the application.[84,85] Cationic systems also shrink less and are less brittle.[5,86]

Typical PAGs are diaryl iodonium salts ($Ar_2I^+X^-$)[87] or triaryl sulfonium(TAS) salts ($Ar_3S^+X^-$)[88] with non-nucleophilic counterions such as BF_4^- or SbF_6^-. These compounds upon irradiation with UV irradiation decompose into a mixture of cations, radical cations and radicals that eventually result in the generation of a superacid which is the principal initiator of cationic polymerization (**Figure 1-7**). Diaryliodonium salts and triarylsulfonium salts generally absorb below around 300nm.[89] For activation with longer wavelengths, they can also be sensitized with another dye up to 400nm[5,90]. Initiation of cationic polymerization by visible light can also be achieved via radical initiated cationic polymerization by using diaryliodonium salts in conjunction with Type II radical photointiators (such as camphorquinone).[91–94] In these systems, radicals generated by the radical photoinitiator oxidize the diaryliodonium salt to produce cations. This is more difficult with triarylsulfonium due to its higher reduction potential.[95]

Most commonly found cationic crosslinkers are epoxides such as diglycidyl ether derivatives of bisphenol A (DGEBA), 3,4-epoxycyclohexylmethyl-3,4-epoxycyclohexanecarboxylate (ECC), and epoxidized soy bean oil (ESBO). Photoresists developed for electronics lithography are also frequently translated to additive manufacturing, such as SU-8.[96] Epoxides often polymerize very slowly and are therefore mostly used in conjunction with a faster polymerizing cationic system such as oxetanes and vinyl ethers in a similar manner for a purely cationic system. Alcohols act as chain transfer agents for cationic polymerization. Similar to multifunctional thiols in thiol-ene chemistry, long chain diols are sometimes added to cationic formulations to tune their mechanical properties.[5]

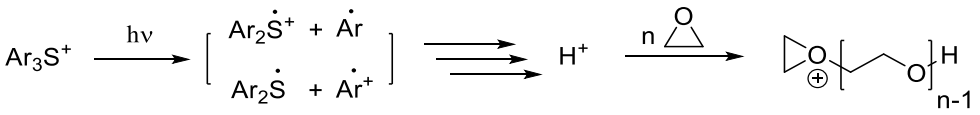

Figure 1-7 Mechanism of cationic polymerization of epoxides

1.2.4 Hybrid and composite formulations

Many photopolymer formulations contain multiple curing components, often a fast-curing component that facilitates fast printing and slower-curing component that generally leads to better material properties.[69] A variety of combination can be found, such as (meth)acrylate/epoxy[97,98] and (meth)acrylate/polyurethanes.[99,100] In both cases, the (meth)acrylate component is cured first during the printing process, and the other component activated by heat during a thermal post-cure process.

Hybrid formulations have also been used to impart spatial control over material properties in vat photopolymerization processes. As has been discussed before, multimaterial printing is difficult for vat photopolymerization as the liquid resin inside the vat is homogenous. However, by clever design a homogenous resin can cure into materials of different properties in response to different wavelength or intensity of light. Hawker[101] and Boydston[102] separately demonstrated using two wavelengths of light to achieve different curing outcomes in a radical-cationic dual cure system. As photoinitiators that absorb at longer wavelengths usually have some absorption at shorter wavelengths, in both systems the acrylic network is cured at longer wavelengths, while both networks are cured when shorter wavelength is used. By using crosslinkers of different length and rigidity for the two systems, the mechanical property of the material can be tuned by curing one or both networks. A common issue with this kind of system is the dark cure propensity of the cationic composition, which means the unreacted cationic crosslinkers need to be removed with swelling otherwise they will eventually cure. It has also been demonstrated that crosslinking density can be controlled in vat photopolymerization system by modulating the intensity of light used for irradiation.[103,104] Lower irradiation intensity leads to lower crosslinking density and thus softer networks. Fang and co-workers[103] cleverly used a diamine crosslinker and took advantage of a thermal post-cure process to consume unreacted acrylate moieties by Michael addition reactions and permanently preserve the variation in crosslinking density.

Composite formulations, in which insoluble particles or fibers are suspended in the resins, are also commonly used in photopolymer formulations for AM.[105–108] In fact, most commercial AM resins can be considered composites as they include pigment particles that are insoluble. Photopolymer

resins can also be filled with glass, ceramic, metal oxide, or other inorganic fillers to imbue them with improved mechanical or electrical properties. [69,108–110]

1.2.5 Materials for Direct Ink Writing (DIW)

While materials used for other photopolymerization-based AM processes are fundamentally similar and sometimes translatable between platforms, materials used for DIW is usually unique so they will be discussed separately. The material extrusion process places unique requirements on the ink material[33,111]: 1) The viscosity needs to be low enough for successful extrusion; 2) The material needs to rapidly gain mechanical strength upon extrusion to maintain its extruded shape, either through a rapid increase in viscosity or a sol-gel transition; 3) As DIW printing is commonly used to fabricate soft materials for biomedical applications, tunable and biocompatible materials are highly desirable. Such requirements limit the scope of materials amenable to this process. The need for low viscosity precludes the extrusion of permanently crosslinked materials, as they would fracture instead of flow in response to the shear forces present during extrusion. In addition, not all transiently crosslinked materials can regain viscosity rapidly enough to maintain their shapes after being extruded. Thus the majority of reported materials are physically crosslinked hydrogels based on supramolecular interactions between biopolymers, such as gelatin[112], collagen[34], alginate[113–117], fibrin[34], hyaluronic acid[118–121] (HA), chitosan[122,123], peptides[124] and nucleic acids[125]. While these materials are suitable for transient scaffolds, a covalently crosslinked gel is desirable for more permanent applications, such as sensors or actuators[115,126–128].

To fabricate covalently crosslinked networks via extrusion-based 3D printing, supramolecular gels composed of photocrosslinkable moieties are often employed, such as gelatin methacrylate (GelMA)[129–133], methacrylated hyaluronic acid (MeHA)[134], PEG diacrylate (PEGDA)[135] or composites thereof[136,137]. A post-print irradiation process is required to induce photocrosslinking. These methods tap into materials proven to be suitable towards extrusion-based 3D printing in order to provide a template for the crosslinked network, but are also limited in that the properties of the final material are still influenced by those of the template material, as it is difficult to remove the large biopolymers from which the template is constructed. Template-free printing of crosslinkable soft matter can be achieved only through a more complex 3D printing setup (such as

a modified extrusion 3D printer with an in-line irradiation device[35], or printing into a sacrificial template[138,139].

1.3 Application of addition-fragmentation chain transfer (AFCT) and reversible addition-fragmentation chain transfer (RAFT) in photopolymer networks

Addition-fragmentation chain transfer (AFCT) and reversible addition-fragmentation chain transfer (RAFT) have long been used to regulate the growth of linear polymers, but only recently have they been applied in controlling the curing of photopolymer networks, especially in the context of additive manufacturing.

1.3.1 Addition-fragmentation chain transfer (AFCT)

Compared to most conventional chain transfer agents such as thiols that mediate chain transfer via hydrogen transfer, AFCT agents mediate chain transfer in a slightly different manner. AFCT agents usually contain a reactive double bond that adds to propagating radicals similar to a normal monomer, and a leaving group L that is cleaved to generate a new reactive radical after fragmentation (**Figure 1-8**). The first step in the AFCT process is the addition of a radical onto the double bond of the chain transfer agent, forming an intermediate radical. The intermediate radical then undergoes fragmentation, which is a β-scission process in which either the original radical is cleaved to form the starting components, or the leaving group is cleaved to form a different reactive radical, completing the chain transfer.[69] The rate of the fragmentation step is influenced by the stability of the intermediate radicals. As intermediate radicals usually do not undergo propagation due to steric hindrance, stable intermediate radicals that take longer to fragment can lead to retardation of the polymerization reaction which is usually undesirable.[69]

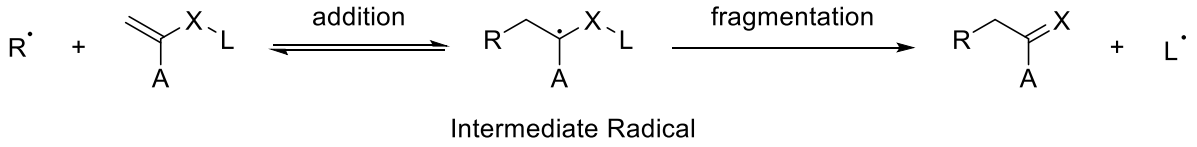

Figure 1-8 General mechanism for addition–fragmentation chain transfer (AFCT)

Similar to thiol-ene systems, AFCT agents can also regulate the polymerization of (meth)acrylate systems by promoting more homogenous chain growth and delaying the gel point, thus reducing shrinkage stress by allowing the network to relax. From a topological perspective, AFCT disrupts the ladder-like structure typical of chain growth networks and renders the network more step-growth-like.

To properly regulate a homopolymerization process, the reactivity of irreversible AFCT agents needs to be carefully tuned in relation to the monomer. The relative reactivity of a chain transfer agent and the monomer can be described by the chain transfer constant C_{tr}, which is the ratio between the rate constant of chain transfer k_{tr} and the rate constant of propagation k_p for the propagating radical. If too active ($C_{tr} >> 1$), the AFCT agent will dominate the beginning of the polymerization process and lead to retardation, but once depleted it will offer no control over the polymerization afterwards and most of the polymerization process will remain unregulated. If too inactive ($C_{tr} << 1$), the AFCT agent will not render any regulation until most of the monomers are depleted. Therefore, for an AFCT agent to successfully regulate a homopolymerization throughout the entire process, it needs to react at a similar rate to that of the monomer ($C_{tr} \sim 1$).[69]

For methacrylic systems, β-allyl sulfones (**Figure 1-9**, MAS) were reported by Liska and coworkers to be suitable AFCT agents.[140–142] β-Allyl sulfones have very similar reactivities to methacrylic monomers ($C_{tr} \sim 1$) and therefore react homogenously. An additional benefit of β-allylsulfones is that they do not suffer from odor or instability as many sulfur-containing reagents do. When β-allyl sulfones were incorporated into methacrylic networks in place of monofunctional diluents, the resulting network exhibited lower shrinkage stress and sharper glass transition, indicating the formation of a more homogenous network. Mono-functional and di-functional β-allyl sulfones (MAS and DAS, respectively) were both synthesized and incorporated into networks, with T_g for the latter slightly higher than the former as the latter acts as a crosslink.[140] DAS has also been incorporated into purely dimethacrylate systems with no monofunctional diluents. Compared to a dithiol with similar structure (which regulates polymerization via thiol-ene mechanism), networks made with DAS see a similar improvement in impact resistance, but does not suffer from significant loss in modulus and hardness as dithiol networks do.[141]

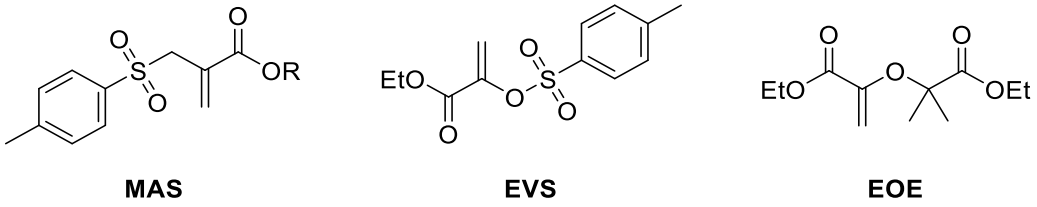

Figure 1-9 Structure of irreversible AFCT agents β-allyl sulfones (MAS), ester-activated vinyl sulfonate ester (EVS), and Ester-Activated Vinyl Ether (EOE)

Despite being able to regulate network formation and improve mechanical properties in methacrylic photopolymer systems, β-allyl sulfones still causes retardation to polymerization kinetics.[69] This is partially due to the fact that the AFCT agent fragments into a methacrylate derivative, which is capable of being attacked by the leaving radical, resulting in non-propagation reactions.[140] To address this, AFCT reagents based on vinyl sulfone esters (**Figure 1-9**, EVS) were developed by Liska and coworkers.[143] By changing the carbon atom between the vinyl and the sulfur into an oxygen, the fragmentation product is changes into an α-ketoester which does not participate further in radical reactions. This results in networks with similar improvements in homogeneity and impact resistance, yet much faster curing kinetics, comparable to unmodified methacrylate networks.[144,145] The fast curing kinetics lends to formulations containing vinyl sulfone ester capable of being 3D printed on a DLP system, with improvements in mechanical properties compared to conventional resin formulations.[143,146] Following a similar concept, another class of AFCT agents known as ester-activated vinyl ethers (EOEs)[147] were also developed based on methyl methacrylate dimers (**Figure 1-9**, EOE).[148] They exhibited similar efficacy in regulation methacrylate network formation without causing significant retardation.

AFCT reagents are an effective strategy to regulate (meth)acrylate photopolymerization without some of the weaknesses of thiol-ene chemistry. Judicious design of irreversible AFCT agents can lead to photopolymer networks with improved homogeneity and impact resistance while avoiding significant retardations.[69] It must be noted that the AFCT agents reviewed here are only those already used in the context of photopolymer networks. A wide variety of AFCT reagents, such as

halides and phosphonates[149–151] have been known and applied to linear polymerization systems, and they present opportunities for novel modifications and applications in photopolymers.

1.3.2 Reversible addition-fragmentation chain transfer (RAFT)

A special case of AFCT is reversible addition-fragmentation chain transfer (RAFT), in which the attacking radical and the fragmented radical are both carbon-centered and the fragmentation step is reversible. Commonly used RAFT agents are thio compounds such as dithioesters, dithiocarbamates, trithiocarbonates, and xanthates (**Figure 1-10**). Similar to the mechanism of AFCT, a propagating radical adds to the C=S double bond in the RAFT agent to form a stabilized intermediate radical, which then undergoes scission of the weakest C-S bond to generate a new propagating radical and a new C=S double bond. In contrast to irreversible AFCT processes, the products of this chain transfer process are qualitatively and energetically identical to the starting species (the RAFT agent is regenerated, and a carbon centered propagating radical is consumed and produced), therefore this process is also called "degenerate chain transfer" (**Figure 1-12**A), with "degenerate" indicating multiple states with equal energy.[152,153] As the regenerated RAFT agent is also capable of reacting with a propagating radical, the entire process is reversible.

An external radical source is still needed to initiate the chain reaction in a RAFT system. In photopolymers a photoinitiator is typically used. Notably, as RAFT agents cannot mediate chain termination, a small number of chains are always irreversibly terminated at the end of the polymerization process, i.e. there is a small number of dead chains, equal to the number of initiators consumed. However, as the number of polymer chains typically equals to the number of RAFT agents, the vast majority of chains would be "alive" and capable of reinititation.

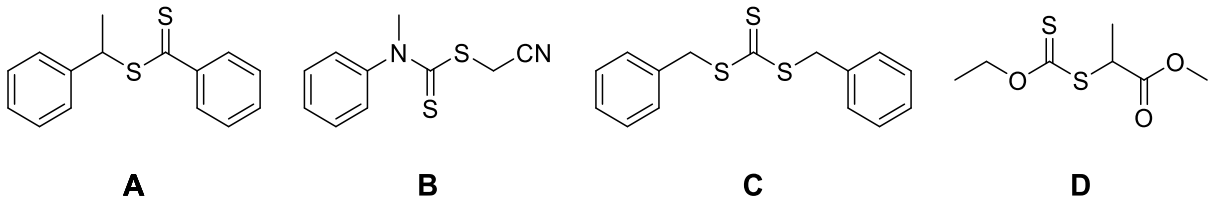

Figure 1-10 Examples of RAFT agents: A) a dithioester; B) a dithiocarbamate; C) a trithiocarbonate; D) a xanthate

Compared to irreversible AFCT agents, RAFT agents will never be depleted; their concentration remain constant throughout the polymerization process, which means they can provide ongoing regulation. Even after the polymerization is completed, they remain attached to polymer chains as dormant end groups which can be reinitiated if a new radical source is provided. This leads to a variety of possibilities for post-functionalization, such as surface modification and the incorporation of new monomers on demand. However, this comes at the cost of causing retardation to the polymerization process.[69]

RAFT agents have been extensively used in gels to introduce the opportunity for modification and self-healing.[154–156] Bowman and co-workers synthesized difunctional methacrylate crosslinkers with a trithiocarbonate core[157] and demonstrated that the inclusion of a small fraction of such crosslinkers in a purely methacrylic system can reduce shrinkage stress and introduce photoplasticity.[158] This crosslinker was also used in model glass-filled methacrylate dental resin and it was demonstrated that it can also reduce stress and improve the toughness of the material.[159]

Allyl sulfides (**Figure 1-11** A) are another example of RAFT agents used in thio-ene systems, reported by Bowman and co-workers.[157,158] Allyl sulfides are capable of undergoing a reversible or irreversible AFCT with a thiyl radical, but its reaction with a carbon radical is strictly irreversible.[160] In practice, they have been demonstrated to reduce shrinkage stress in, and improve mechanical performance of, thiol-ene and thiol-yne systems.[77,161] Due to the reversibility of allyl sulfides, thiol-ene networks incorporated with allyl sulfides are covalent adaptable networks (CANs).[162,163] CANs are defined as thermoset networks in which covalent bonds can rearrange

under certain conditions, such as light irradiation, to adapt to external stress. In this case, residual photoinitiators in the network are activated to produce new radicals, which undergo RAFT process mediated by allyl sulfides to allow the network to rearrange and relax to "adapt" to external stress.[164,165] As no functional groups are consumed during the chain transfer process, this process can be repeated as long as there is still residual photoinitiators.

However, as the AFCT process between allyl sulfides and carbon radicals are not fully reversible (**Figure 1-11** B), most allyl sulfides are less effective in (meth)acrylate homopolymerization networks due to the mismatch in reactivities between the monomers and the AFCT agent which means AFCT is not taking place throughout most of the reaction.[69,160]

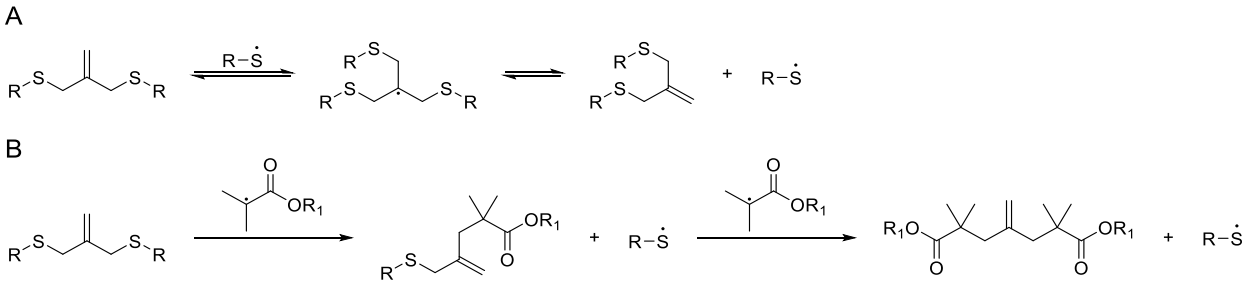

Figure 1-11 A) Reversible AFCT reaction of β-allyl sulfides with thiyl radicals and B) Irreversible AFCT reaction with carbon-centered radicals[160]

1.3.3 Photoiniferters

In addition to acting solely as chain transfer agents, many RAFT agents are also capable of acting as initiator and terminator.(**Figure 1-12**B) In this role they are known as iniferters (initiator-transfer-agent-terminators).[166] In fact, the use of iniferters in polymerization was reported prior to the introduction of RAFT polymerization. Iniferters can be activated thermally or photochemically; in the latter case they are called photoiniferters.[167] Commonly used photoiniferters such as thiocarbonylthio, trithiocarbonates, and disulfides can upon UV irradiation undergo cleavage of one of their C-S bonds to form a carbon-centered propagating radical, leaving behind a sulfur-centered iniferter radical. Uncleaved iniferters can then act as RAFT agents to regulate the

propagation of the propagating radicals via degenerate chain transfer. At the end of the process, the propagating radical can recombine with an iniferter radical to regenerate the iniferter. As no exogenous radical source is used in the process, iniferter polymerization can ideally proceed with complete reversibility with all the radicals recombining with iniferter radicals. Therefore, no dead chains are generated, as opposed to photoinitated RAFT polymerization in which a small fraction of dead chains is unavoidable.

Bowman and co-workers[168,169] reported using a methacrylated dithiocarbamate as a photoiniferter to polymerize a crosslinked acrylic network in which dithiocarbamate moieties can be found on the surface and throughout the material. After fabrication of the crosslinked material, the dithiocarbamate moieties can be addressed with light to reinitiate polymerization and introduce new monomers into the network. Densely crosslinked networks do not swell well with monomers, thus only surface modification is achieved; in less densely crosslinked networks monomers can be inserted throughout the network. With a photomask, photopatterning can be achieved on surfaces. It is interesting to note that as the dithiocarbamate used is a N,N-dialkyldithiocarbamate, which has very low RAFT activity towards (meth)acrylates[170]. Therefore, its role is more or less limited to being an "initer", which mediates initiation and termination, but not chain transfer. Based on this system, the same group developed a primitive 3D printing system called contact liquid photolithographic polymerization (CLiPP) in which a photopolymer resin is photopatterned and cured in a layer by layer fashion[171,172]. The photopolymer resin comprises of multifunctional vinyl crosslinkers, methacrylated photoiniferters, and additional photoinitiators to increase speed. Similar to 3D printing, the photopolymer resin is deposited in thin layers, cured through a photomask, and the uncured monomers were washed off and the cavities refilled with a wax support material. A new layer is deposited on top and the process is repeated. In this case the photoiniferter is used to increase layer adhesion, as they will be present on the surface of an underlying layer, ready to bond to a new layer of cured resin. Fabrication of microfluidic devices were demonstrated. Johnson and co-workers functionalized a trithiocarbonate photoiniferter with norbornenes and fabricated an end-linked network with trithiocarbonates uniformly incorporated into every strand[173]. This "primary gel" can then be swollen with another monomer (NiPAAM) and irradiated with light to activate the trithiocarbonate photoiniferters. Ideally, as both ends of

most trithiocarbonates are bound in the network, monomers can be thought to be inserted into the network strands. Rearrangement of the strands happen but only changes the topology without changing the overall architecture. The ability of tritioncarbonates to undergo aminolysis allows the new network to be degraded to quantify monomer insertion.

Jin and co-workers[16] demonstrated that iniferter polymerization can be realized on a commercial MSLA printer with 405nm light source. PEG diacrylate was used as the monomer and 4-cyano-4-[(dodecylsulfanylthiocarbonyl) sulfanyl] pentanoic acid (CDTPA) or dibenzyl trithiocarbonate (DBTTC), both trithiocarbonates, were uses as the iniferter. The print speed is severely limited by initiation efficiency and the RAFT process, and is more than 100 times slower compared to typical print speeds achieved with an uncontrolled radical photopolymerization system. The long irradiation times required for the method also resulted in significant reduction in resolution, due to both material diffusion and light diffusion out of the irradiated areas. However, the presence of trithiocarbonates in the system allow post modification via insertion of new monomers, as demonstrated by modifying the printed object with a fluorescent monomer.

1.3.4 Photoredox-catalyzed iniferter polymerization

In conventional photoiniferter polymerization systems, activation of a thio-based photoiniferter is achieved with direct photolysis by exciting the π- π^* transition of the iniferter with a UV light source[173–175], or the n- π^* transition with visible light[176–178]. Alternatively, a photoredox catalyst can be used reduce the thio compound into an unstable radical anion that undergoes fragmentation to produce a propagating radical.(**Figure 1-12**C) The propagating radical can undergo propagation and degenerate chain transfer, before recombining with the thio compound and reducing the photocatalyst back to its ground state, completing the catalytic cycle. In some cases, the activation is completed via a triplet state energy transfer rather than an electron transfer[179,180]. Examples of typical photoredox catalysts used are $Ir(ppy)_3$, eosin Y (EY), and erythrosin B (EB).

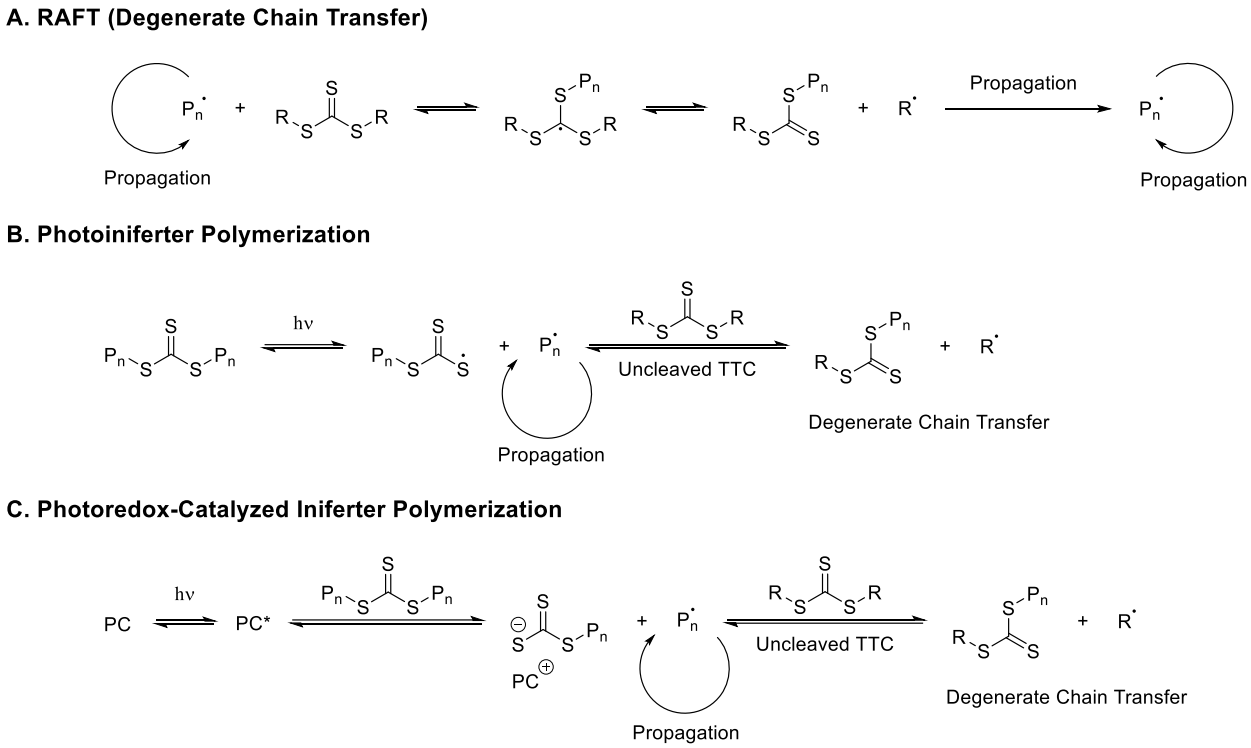

Figure 1-12 Difference in mechanism between RAFT, photoiniferter polymerization and photoredox-catalyzed iniferter polymerization

Boyer and co-workers demonstrated that the use of a photocatalyst in an iniferter-based AM system can drastically improve the print speed to within the same order of magnitude as uncontrolled radical systems.[181] The fabrication of materials with complex geometry and nanostructure was demonstrated[182,183]. A variety of tritioncarbonates, xanthates and dithiocarbamates were used, and it was found that xanthates and asymmetrical trithiocarbonates outperformed the rest in terms of speed and the stiffness of the material produced. The addition of more thio compounds generally lead to slower cure.[184] The presence of trithiocarbonate moieties throughout the material allows a variety of strategies for post-print modifications to demonstrated. The trithiocarbonates can be addressed as RAFT agents by mediating monomer insertion to modify surface properties[185], or cleaved via aminolysis to expose thiols onto which molecules can be attached via thiol-ene reactions[184]. The group also recently demonstrated that the trithiocarbonates can be re-activated with UV light to mediate self-healing.[186]

1.3.5 Photoredox-catalyzed controlled radical polymerization

The photoredox activation of thio compounds is not limited to radical polymerization. The Fors group demonstrated that certain some dithiocarbamates and trithiocarbonates can also be oxidized with an oxidative photocatalyst to initiate and control the cationic polymerization of vinyl ethers[187]. On-Off control with light as well as control over molecular weight and dispersity is achieved[188]. Its postulated mechanism is similar to that of its radical counterpart, except a cationic species is generated in lieu of a radical. Eventually the propagating cation recombines with the iniferter to reversibly terminate. An important feature of this method is that it avoids the propensity for uncontrolled cationic systems to dark cure. The same group later demonstrated a mixed system with an oxidizing photocatalyst and a reducing photocatalyst , which can switch between radical and cationic polymerization of acrylates and vinyl ethers, respectively, depending on the wavelength of light[189]. This is later applied to photopolymer networks to fabricate thermoset materials with spatiotemporally controlled crosslinking densities through photopatterning[190].

References

(1) Skylar-Scott, M. A.; Mueller, J.; Visser, C. W.; Lewis, J. A. Voxelated Soft Matter via Multimaterial Multinozzle 3D Printing. *Nature* **2019**, *575* (7782), 330–335. https://doi.org/10.1038/s41586-019-1736-8.

(2) Sitthi-Amorn, P.; Ramos, J. E.; Wang, Y.; Kwan, J.; Lan, J.; Wang, W.; Matusik, W. MultiFab. *ACM Trans. Graph.* **2015**, *34* (4). https://doi.org/10.1145/2766962.

(3) Prusa Knowledge Base | MMU2S and soluble materials (PVA/BVOH) https://help.prusa3d.com/en/article/mmu2s-and-soluble-materials-pva-bvoh_162860/ (accessed Jan 11, 2022).

(4) Müller, M.; Huynh, Q.-U.; Uhlmann, E.; Wagner, M. H. Study of Inkjet Printing as Additive Manufacturing Process for Gradient Polyurethane Material. https://doi.org/10.1007/s11740-013-0504-0.

(5) Ligon, S. C.; Liska, R.; Stampfl, J.; Gurr, M.; Mülhaupt, R. Polymers for 3D Printing and Customized Additive Manufacturing. *Chemical Reviews*. 2017, pp 10212–10290. https://doi.org/10.1021/acs.chemrev.7b00074.

(6) Nayyeri, P.; Kourosh Zareinia, ·; Bougherara, H. Planar and Nonplanar Slicing Algorithms for Fused Deposition Modeling Technology: A Critical Review. *Int. J. Adv. Manuf. Technol. 2021* **2022**, 1–26. https://doi.org/10.1007/S00170-021-08347-X.

(7) The 3D Benchy "torture test" that pushes 3D printers to the limit - 3D Printing Industry https://3dprintingindustry.com/news/3d-benchy-torture-test-pushes-3d-printers-limit-103662/ (accessed Jan 11, 2022).

(8) FDM 3D Printer Fused Deposition Modeling Technology for 3D Printing | Stratasys https://www.stratasys.com/fdm-technology (accessed Jan 11, 2022).

(9) Deckard, C. R. .; Beaman, J. J. .; Darrah, J. F. Method and Apparatus for Producing Parts by Selective Sintering. *U.S. Pat. 4,863,538* **1992**, 12.

(10) Paul, F. J. *Rapid Prototyping & Manufacturing: Fundamentals of Stereolithography - Paul Francis Jacobs - Google Books*; 1992.

(11) Download Bridging And Overhang Test design 3D print https://3dmixers.com/m/54722-bridging-and-overhang-test (accessed Jan 13, 2022).

(12) Green, B. J.; Guymon, C. A. Modification of Mechanical Properties and Resolution of Printed Stereolithographic Objects through RAFT Agent Incorporation. *Addit. Manuf.* **2019**, *27*, 20–31. https://doi.org/10.1016/j.addma.2019.02.008.

(13) Dizon, J. R. C.; Gache, C. C. L.; Cascolan, H. M. S.; Cancino, L. T.; Advincula, R. C. Post-Processing of 3D-Printed Polymers. *Technologies* **2021**, *9* (3), 61. https://doi.org/10.3390/technologies9030061.

(14) Impens, D.; Urbanic, R. J. Assessing the Impact of Post-Processing Variables on Tensile and Compression Characteristics for 3D Printed Components. *IFAC-PapersOnLine* **2015**, *48* (3), 652–657. https://doi.org/10.1016/J.IFACOL.2015.06.156.

(15) Khosravani, M. R.; Schüürmann, J.; Berto, F.; Reinicke, T. On the Post-Processing of 3d-Printed Abs Parts. *Polymers (Basel).* **2021**, *13* (10), 1559. https://doi.org/10.3390/polym13101559.

(16) Bagheri, A.; Engel, K. E.; Bainbridge, C. W. A.; Xu, J.; Boyer, C.; Jin, J. 3D Printing of Polymeric Materials Based on Photo-RAFT Polymerization. *Polym. Chem.* **2020**, *11* (3), 641–647.

(17) Momeni, F.; M.Mehdi Hassani.N, S.; Liu, X.; Ni, J. A Review of 4D Printing. *Mater. Des.* **2017**, *122*, 42–79. https://doi.org/10.1016/J.MATDES.2017.02.068.

(18) del Barrio, J.; Sánchez-Somolinos, C.; del Barrio, J.; Sánchez-Somolinos, C. *Light to Shape the Future: From Photolithography to 4D Printing*; 2019; Vol. 7, p 1900598.

(19) Tibbits, S. 4D Printing: Multi-Material Shape Change. *Archit. Des.* **2014**, *84* (1), 116–121. https://doi.org/10.1002/AD.1710.

(20) Zhang, J.; Xiao, P. 3D Printing of Photopolymers. *Polymer Chemistry*. Royal Society of Chemistry April 7, 2018, pp 1530–1540. https://doi.org/10.1039/c8py00157j.

(21) What is FFF?: Fused filament fabrication technology for 3D printing https://ultimaker.com/learn/what-is-fff-fused-filament-fabrication-technology-for-3d-printing (accessed Jan 11, 2022).

(22) Fused Deposition Modeling Plastic Jet Printing (PJP) | 3D Systems https://www.3dsystems.com/fused-deposition-modeling (accessed Jan 11, 2022).

(23) Kirchmajer, D. M.; Gorkin, R.; In Het Panhuis, M. An Overview of the Suitability of Hydrogel-Forming Polymers for Extrusion-Based 3D-Printing. *J. Mater. Chem. B* **2015**, *3* (20), 4105–4117. https://doi.org/10.1039/C5TB00393H.

(24) Buswell, R. A.; Leal de Silva, W. R.; Jones, S. Z.; Dirrenberger, J. 3D Printing Using Concrete Extrusion: A Roadmap for Research. *Cem. Concr. Res.* **2018**, *112*, 37–49. https://doi.org/10.1016/J.CEMCONRES.2018.05.006.

(25) Jones, R.; Haufe, P.; Sells, E.; Iravani, P.; Olliver, V.; Palmer, C.; Bowyer, A. RepRap – the Replicating Rapid Prototyper. *Robotica* **2011**, *29* (1), 177–191. https://doi.org/10.1017/S026357471000069X.

(26) Overview - Klipper documentation https://www.klipper3d.org/Overview.html (accessed Jan 11, 2022).

(27) Home | Marlin Firmware https://marlinfw.org/ (accessed Jan 11, 2022).

(28) McIlroy, C.; Seppala, J. E.; Kotula, A. P. Combining Modeling and Measurements To Predict Crystal Morphology in Material Extrusion. In *ACS Symposium Series*; American Chemical Society, 2019; Vol. 1315, pp 85–113. https://doi.org/10.1021/bk-2019-1315.ch006.

(29) Mollah, M. T.; Comminal, R.; Serdeczny, M. P.; Pedersen, D. B.; Spangenberg, J. Stability and Deformations of Deposited Layers in Material Extrusion Additive Manufacturing. *Addit. Manuf.* **2021**, *46*, 102193. https://doi.org/10.1016/J.ADDMA.2021.102193.

(30) Truby, R. L.; Lewis, J. A. Printing Soft Matter in Three Dimensions. *Nat. 2016 5407633* **2016**, *540* (7633), 371–378. https://doi.org/10.1038/nature21003.

(31) Alexandre, A.; Cruz Sanchez, F. A.; Boudaoud, H.; Camargo, M.; Pearce, J. M. Mechanical Properties of Direct Waste Printing of Polylactic Acid with Universal Pellets Extruder: Comparison to Fused Filament Fabrication on Open-Source Desktop Three-Dimensional Printers. *3D Print. Addit. Manuf.* **2020**, *7* (5), 237–247. https://doi.org/10.1089/3dp.2019.0195.

(32) Lewis, J. A. Direct Ink Writing of 3D Functional Materials. *Adv. Funct. Mater.* **2006**, *16* (17), 2193–2204. https://doi.org/10.1002/ADFM.200600434.

(33) Li, L.; Lin, Q.; Tang, M.; Duncan, A. J. E.; Ke, C. Advanced Polymer Designs for Direct-Ink-Write 3D Printing. *Chem. – A Eur. J.* **2019**, *25* (46), 10768–10781. https://doi.org/10.1002/chem.201900975.

(34) Lee, Y. B.; Polio, S.; Lee, W.; Dai, G.; Menon, L.; Carroll, R. S.; Yoo, S. S. Bio-Printing of Collagen and VEGF-Releasing Fibrin Gel Scaffolds for Neural Stem Cell Culture. *Exp. Neurol.* **2010**, *223* (2), 645–652. https://doi.org/10.1016/j.expneurol.2010.02.014.

(35) Ouyang, L.; Highley, C. B.; Sun, W.; Burdick, J. A.; Ouyang, L.; Highley, C. B.; Burdick, J. A.; Sun, W. A Generalizable Strategy for the 3D Bioprinting of Hydrogels from Nonviscous Photo-Crosslinkable Inks. *Adv. Mater.* **2017**, *29* (8), 1604983.

(36) Dababneh, A. B.; Ozbolat, I. T. Bioprinting Technology: A Current State-of-the-Art Review. *J. Manuf. Sci. Eng. Trans. ASME* **2014**, *136* (6). https://doi.org/10.1115/1.4028512/377608.

(37) Mobaraki, M.; Ghaffari, M.; Yazdanpanah, A.; Luo, Y.; Mills, D. K. Bioinks and Bioprinting: A Focused Review. *Bioprinting* **2020**, *18*, e00080. https://doi.org/10.1016/J.BPRINT.2020.E00080.

(38) Gudapati, H.; Dey, M.; Ozbolat, I. A Comprehensive Review on Droplet-Based Bioprinting: Past, Present and Future. *Biomaterials* **2016**, *102*, 20–42. https://doi.org/10.1016/J.BIOMATERIALS.2016.06.012.

(39) Gross, B.; Lockwood, S. Y.; Spence, D. M. Recent Advances in Analytical Chemistry by 3D Printing. *Anal. Chem.* **2016**, *89* (1), 57–70. https://doi.org/10.1021/ACS.ANALCHEM.6B04344.

(40) autodesk_ember:autodesk_ember [Instructions] http://www.formlab.schoolofarts.be/instructions/doku.php?id=autodesk_ember:autodesk_ember (accessed Jan 11, 2022).

(41) Teflon™ AF Amorphous Fluoropolymer Resins https://www.teflon.com/en/products/resins/amorphous-fluoropolymer (accessed Jan 11, 2022).

(42) Tumbleston, J. R.; Shirvanyants, D.; Ermoshkin, N.; Janusziewicz, R.; Johnson, A. R.; Kelly, D.; Chen, K.; Pinschmidt, R.; Rolland, J. P.; Ermoshkin, A.; Samulski, E. T.; DeSimone, J. M. Continuous Liquid Interface Production of 3D Objects. *Science* **2015**, *347* (6228), 1349–1352. https://doi.org/10.1126/science.aaa2397.

(43) WO2015164234A1 - Continuous three dimensional fabrication from immiscible liquids - Google Patents https://patents.google.com/patent/WO2015164234A1/en (accessed Jan 12, 2022).

(44) Walker, D. A.; Hedrick, J. L.; Mirkin, C. A. Rapid, Large-Volume, Thermally Controlled 3D Printing Using a Mobile Liquid Interface. *Science* **2019**, *366* (6463), 360–364. https://doi.org/10.1126/science.aax1562.

(45) What Does Resolution Mean in 3D Printing? https://formlabs.com/blog/3d-printer-resolution-meaning/ (accessed Jan 12, 2022).

(46) US4575330A - Apparatus for production of three-dimensional objects by stereolithography - Google Patents https://patents.google.com/patent/US4575330A/en (accessed Jan 12, 2022).

(47) Schweiger, J.; Edelhoff, D.; Güth, J. F. 3D Printing in Digital Prosthetic Dentistry: An Overview of Recent Developments in Additive Manufacturing. *J. Clin. Med. 2021, Vol. 10, Page 2010* **2021**, *10* (9), 2010. https://doi.org/10.3390/JCM10092010.

(48) Lee, B. Chapter 1 Introduction to ±12 Degree Orthogonal Digital Micromirror Devices (DMDs) Introduction to ±12 Degree Orthogonal Digital Micromirror Devices (DMDs). **2008**.

(49) Kelly, B. E.; Bhattacharya, I.; Heidari, H.; Shusteff, M.; Spadaccini, C. M.; Taylor, H. K. Volumetric Additive Manufacturing via Tomographic Reconstruction. *Science* **2019**, *363* (6431), 1075–1079.

(50) Oakdale, J. S.; Ye, J.; Smith, W. L.; Biener, J. Post-Print UV Curing Method for Improving the Mechanical Properties of Prototypes Derived from Two-Photon Lithography. *Opt. Express* **2016**, *24* (24), 27077. https://doi.org/10.1364/oe.24.027077.

(51) Two-Photon Polymerization: A New Approach to Micromachining | Features | Oct 2006 | Photonics Spectra https://www.photonics.com/Articles/Two-Photon_Polymerization_A_New_Approach_to/a26907 (accessed Jan 1, 2022).

(52) Ye, C.; Zhou, L.; Wang, X.; Liang, Z. Photon Upconversion: From Two-Photon Absorption (TPA) to Triplet–Triplet Annihilation (TTA). *Phys. Chem. Chem. Phys.* **2016**, *18* (16), 10818–10835. https://doi.org/10.1039/C5CP07296D.

(53) LaFratta, C. N.; Li, L. Making Two-Photon Polymerization Faster. *Three-Dimensional Microfabr. Using Two-phot. Polym. Fundam. Technol. Appl.* **2016**, 221–241. https://doi.org/10.1016/B978-0-323-35321-2.00011-X.

(54) Xiong, W.; Zhou, Y. S.; He, X. N.; Gao, Y.; Mahjouri-Samani, M.; Jiang, L.; Baldacchini, T.; Lu, Y. F. Simultaneous Additive and Subtractive Three-Dimensional Nanofabrication Using Integrated Two-Photon Polymerization and Multiphoton Ablation. *Light Sci. Appl. 2012 14* **2012**, *1* (4), e6–e6. https://doi.org/10.1038/lsa.2012.6.

(55) Lin, Y.; Xu, J. Microstructures Fabricated by Two-Photon Polymerization and Their Remote Manipulation Techniques: Toward 3D Printing of Micromachines. *Adv. Opt. Mater.* **2018**, *6* (8), 1701359. https://doi.org/10.1002/ADOM.201701359.

(56) Carlotti, M.; Mattoli, V.; Carlotti, M.; Mattoli, V. Functional Materials for Two-Photon Polymerization in Microfabrication. *Small* **2019**, *15* (40), 1902687. https://doi.org/10.1002/SMLL.201902687.

(57) Sanders, S. N.; Schloemer, T. H.; Gangishetty, M. K.; Anderson, D.; Seitz, M.; Gallegos, A. O.; Stokes, R. C.; Congreve, D. N. Triplet Fusion Upconversion Nanocapsules for Volumetric 3D Printing. **2021**.

(58) Kabb, C. P.; O'Bryan, C. S.; Deng, C. C.; Angelini, T. E.; Sumerlin, B. S. Photoreversible Covalent Hydrogels for Soft-Matter Additive Manufacturing. *ACS Appl. Mater. Interfaces* **2018**, *10* (19), 16793–16801.

(59) Bagheri, A.; Jin, J. Photopolymerization in 3D Printing. *ACS Appl. Polym. Mater.* **2019**, *1* (4), 593–611. https://doi.org/10.1021/acsapm.8b00165.

(60) Liu, S.; Brunel, D.; Sun, K.; Xu, Y.; Morlet-Savary, F.; Graff, B.; Xiao, P.; Dumur, F.; Lalevée, J. A Monocomponent Bifunctional Benzophenone–Carbazole Type II Photoinitiator for LED Photoinitiating Systems. *Polym. Chem.* **2020**, *11* (21), 3551–3556. https://doi.org/10.1039/D0PY00644K.

(61) Allushi, A.; Kutahya, C.; Aydogan, C.; Kreutzer, J.; Yilmaz, G.; Yagci, Y. Conventional Type II Photoinitiators as Activators for Photoinduced Metal-Free Atom Transfer Radical

Polymerization. *Polym. Chem.* **2017**, *8* (12), 1972–1977. https://doi.org/10.1039/C7PY00114B.

(62) Von Raumer, M.; Suppan, P.; Haselbach, E. Photoreduction of Triplet Benzophenone by Tertiary Amines: Amine Molecular Structure and Ketyl Radical Yield. *Helv. Chim. Acta* **1997**, *80* (3), 719–724. https://doi.org/10.1002/HLCA.19970800309.

(63) Viswanathan, K.; Hoyle, C. E.; Jönsson, E. S.; Nason, C.; Lindgren, K. Effect of Amine Structure on Photoreduction of Hydrogen Abstraction Initiators. *Macromolecules* **2002**, *35* (21), 7963–7967. https://doi.org/10.1021/MA0120308.

(64) Autodesk Releases Ember's 3D Printing Resin as Open Source (Between the Lines) https://autodesk.blogs.com/between_the_lines/2015/03/autodesk-releases-embers-3d-printing-resin-as-open-source.html (accessed Jan 2, 2022).

(65) Gu, Y.; Zhao, J.; Johnson, J. A. Polymer Networks: From Plastics and Gels to Porous Frameworks. *Angew. Chemie Int. Ed.* **2020**, *59* (13), 5022–5049. https://doi.org/10.1002/anie.201902900.

(66) Schamboeck, V.; Kryven, I.; Iedema, P. D. Acrylate Network Formation by Free-Radical Polymerization Modeled Using Random Graphs. *Macromol. Theory Simulations* **2017**, *26* (6), 1700047. https://doi.org/10.1002/MATS.201700047.

(67) Karnes, J. J.; Weisgraber, T. H.; Oakdale, J. S.; Mettry, M.; Shusteff, M.; Biener, J. On the Network Topology of Cross-Linked Acrylate Photopolymers: A Molecular Dynamics Case Study. *J. Phys. Chem. B* **2020**, *124* (41), 9204–9215. https://doi.org/10.1021/acs.jpcb.0c05319.

(68) Cunha, L. G.; Alonso, R. C. B.; De Souza, E. J. C.; Neves, A. C. E. C.; Correr-Sobrinho, L.; Sinhoreti, M. A. C. Influence of the Curing Method on the Post-Polymerization

Shrinkage Stress of a Composite Resin. *J. Appl. Oral Sci.* **2008**, *16* (4), 266–270. https://doi.org/10.1590/S1678-77572008000400007.

(69) Ligon-Auer, S. C.; Schwentenwein, M.; Gorsche, C.; Stampfl, J.; Liska, R. Toughening of Photo-Curable Polymer Networks: A Review. *Polym. Chem.* **2015**, *7* (2), 257–286. https://doi.org/10.1039/C5PY01631B.

(70) Deng, S.; Wu, J.; Dickey, M. D.; Zhao, Q.; Xie, T.; Deng, S.; Wu, J.; Zhao, Q.; Xie, T.; Dickey, M. D. Rapid Open-Air Digital Light 3D Printing of Thermoplastic Polymer. *Adv. Mater.* **2019**, *31* (39), 1903970. https://doi.org/10.1002/ADMA.201903970.

(71) Hoyle, C. E.; Bowman, C. N.; Bowman, C. N.; Hoyle, C. E. Thiol–Ene Click Chemistry. *Angew. Chemie Int. Ed.* **2010**, *49* (9), 1540–1573. https://doi.org/10.1002/ANIE.200903924.

(72) Holger Leonards, al; Engelhardt, S.; Hoffmann, A.; Pongratz, L.; Schriever, S.; Bläsius, J.; Wehner, M. M.; Gillner, A.; Leonards, H.; Wehner, M. Advantages and Drawbacks of Thiol-Ene Based Resins for 3D-Printing. *https://doi.org/10.1117/12.2081169* **2015**, *9353* (16), 52–58. https://doi.org/10.1117/12.2081169.

(73) Wang, C.; Wang, C.; Li, Z. Thiol-Ene-Acrylate Ternary Photosensitive Resins for DLP 3D Printing. *J. Photopolym. Sci. Technol.* **2020**, *33* (3), 285–290. https://doi.org/10.2494/PHOTOPOLYMER.33.285.

(74) Navaruckiene, A.; Kasetaite, S.; Ostrauskaite, J. Vanillin-Based Thiol-Ene Systems as Photoresins for Optical 3D Printing. *Rapid Prototyp. J.* **2020**, *26* (2), 402–408. https://doi.org/10.1108/RPJ-03-2019-0076.

(75) Sycks, D. G.; Wu, T.; Park, H. S.; Gall, K. Tough, Stable Spiroacetal Thiol-Ene Resin for 3D Printing. *J. Appl. Polym. Sci.* **2018**, *135* (22), 46259. https://doi.org/10.1002/APP.46259.

(76) Ye, S.; Cramer, N. B.; Smith, I. R.; Voigt, K. R.; Bowman, C. N. Reaction Kinetics and Reduced Shrinkage Stress of Thiol–Yne–Methacrylate and Thiol–Yne–Acrylate Ternary Systems. *Macromolecules* **2011**, *44* (23), 9084–9090. https://doi.org/10.1021/ma2018809.

(77) Lee, T. Y.; Carioscia, J.; Smith, Z.; Bowman, C. N. Thiol−Allyl Ether−Methacrylate Ternary Systems. Evolution Mechanism of Polymerization-Induced Shrinkage Stress and Mechanical Properties. *Macromolecules* **2007**, *40* (5), 1473–1479. https://doi.org/10.1021/ma0624954.

(78) Ligon, S. C.; Husár, B.; Wutzel, H.; Holman, R.; Liska, R. Strategies to Reduce Oxygen Inhibition in Photoinduced Polymerization. *Chemical Reviews*. American Chemical Society January 8, 2014, pp 577–589. https://doi.org/10.1021/cr3005197.

(79) Chen, L.; Wu, Q.; Wei, G.; Liu, R.; Li, Z. Highly Stable Thiol–Ene Systems: From Their Structure–Property Relationship to DLP 3D Printing. *J. Mater. Chem. C* **2018**, *6* (43), 11561–11568. https://doi.org/10.1039/C8TC03389G.

(80) Zhang, X.; Xi, W.; Wang, C.; Podgórski, M.; Bowman, C. N. Visible-Light-Initiated Thiol-Michael Addition Polymerizations with Coumarin-Based Photobase Generators: Another Photoclick Reaction Strategy. *ACS Macro Lett.* **2016**, *5* (2), 229–233. https://doi.org/10.1021/acsmacrolett.5b00923.

(81) Zhang, X.; Xi, W.; Gao, G.; Wang, X.; Stansbury, J. W.; Bowman, C. N. *O* -Nitrobenzyl-Based Photobase Generators: Efficient Photoinitiators for Visible-Light Induced Thiol-Michael Addition Photopolymerization. *ACS Macro Lett.* **2018**, *7* (7), 852–857. https://doi.org/10.1021/acsmacrolett.8b00435.

(82) Zhang, X.; Wang, X.; Chatani, S.; Bowman, C. N. Phosphonium Tetraphenylborate: A Photocatalyst for Visible-Light-Induced, Nucleophile-Initiated Thiol-Michael Addition

Photopolymerization. *ACS Macro Lett.* **2021**, *10* (1), 84–89. https://doi.org/10.1021/acsmacrolett.0c00809.

(83) Upul Ranaweera, R. A. A.; Schuman, T. P.; Wang, R.; Miller, B. D.; Kilway, K. V. Effect of Moisture on Cationic Polymerization of Silicone Epoxy Monomers. *J. Appl. Polym. Sci.* **2015**, *132* (15), 41831. https://doi.org/10.1002/app.41831.

(84) Sipani, V.; Scranton, A. B. Dark-Cure Studies of Cationic Photopolymerizations of Epoxides: Characterization of the Active Center Lifetime and Kinetic Rate Constants. *J. Polym. Sci. Part A Polym. Chem.* **2003**, *41* (13), 2064–2072. https://doi.org/10.1002/POLA.10750.

(85) Decker, C.; Bianchi, C.; Decker, D.; Morel, F. Photoinitiated Polymerization of Vinyl Ether-Based Systems. *Prog. Org. Coatings* **2001**, *42* (3–4), 253–266. https://doi.org/10.1016/S0300-9440(01)00203-X.

(86) Stanford, J. L.; Ryan, A. J.; Yang, Y. Photoinitiated Cationic Polymerization of Epoxides. *Polym. Int.* **2001**, *50* (9), 986–997. https://doi.org/10.1002/PI.730.

(87) Crivello, J. V. The Discovery and Development of Onium Salt Cationic Photoinitiators. *J Polym Sci A Polym Chem* **1999**, *37*, 4241–4254. https://doi.org/10.1002/(SICI)1099-0518(19991201)37:23.

(88) Crivello, J. V.; Lam, J. H. W. Photoinitiated Cationic Polymerization with Triarylsulfonium Salts. *J. Polym. Sci. Polym. Chem. Ed.* **1979**, *17* (4), 977–999. https://doi.org/10.1002/POL.1979.170170405.

(89) Crivello, J. V. Cationic Polymerization — Iodonium and Sulfonium Salt Photoinitiators. *Initiat. — Poly-Reactions — Opt. Act.* **1984**, 1–48. https://doi.org/10.1007/BFB0024034.

(90) Crivello, J. V.; Lam, J. H. W. Dye-Sensitized Photoinitiated Cationic Polymerization. The System: Perylene–Triarylsulfonium Salts. *J. Polym. Sci. Polym. Chem. Ed.* **1979**, *17* (4), 1059–1065. https://doi.org/10.1002/POL.1979.170170411.

(91) Crivello, J. V. Radical-Promoted Visible Light Photoinitiated Cationic Polymerization of Epoxides. *J. Macromol. Sci. Part A Pure Appl. Chem.* **2009**, *46* (5), 474–483. https://doi.org/10.1080/10601320902797707.

(92) and, J. V. C.; Liu, S. Free Radical Induced Acceleration of Cationic Photopolymerization. **1998**. https://doi.org/10.1021/CM980494N.

(93) Crivello, J. V; Liu, S.; and, J. V. C.; Liu, S.; Crivello, J. V; Liu, S. Free Radical Induced Acceleration of Cationic Photopolymerization. **1998**. https://doi.org/10.1021/cm980494n.

(94) Durmaz, Y. Y.; Moszner, N.; Yagci, Y. Visible Light Initiated Free Radical Promoted Cationic Polymerization Using Acylgermane Based Photoinitiator in the Presence of Onium Salts. *Macromolecules* **2008**, *41* (18), 6714–6718. https://doi.org/10.1021/MA801208N.

(95) Crivello, J. V. Redox Initiated Cationic Polymerization: Reduction of Triarylsulfonium Salts by Silanes. https://doi.org/10.1007/s12633-009-9007-1.

(96) Ovsianikov, A.; Ostendorf, A.; Chichkov, B. N. Three-Dimensional Photofabrication with Femtosecond Lasers for Applications in Photonics and Biomedicine. *Appl. Surf. Sci.* **2007**, *253* (15), 6599–6602. https://doi.org/10.1016/J.APSUSC.2007.01.058.

(97) Cui, Y.; Yang, J.; Lei, D.; Su, J. 3D Printing of a Dual-Curing Resin with Cationic Curable Vegetable Oil. *Ind. Eng. Chem. Res.* **2020**, *59* (25), 11381–11388. https://doi.org/10.1021/acs.iecr.0c01507.

(98) Uzcategui, A. C.; Muralidharan, A.; Ferguson, V. L.; Bryant, S. J.; McLeod, R. R. Understanding and Improving Mechanical Properties in 3D Printed Parts Using a Dual-Cure Acrylate-Based Resin for Stereolithography. *Adv. Eng. Mater.* **2018**, *20* (12), 1800876. https://doi.org/10.1002/ADEM.201800876.

(99) Bachmann, J.; Gleis, E.; Fruhmann, G.; Riedelbauch, J.; Schmölzer, S.; Hinrichsen, O. Investigation of the Temperature Influence on the Dual Curing Urethane-Methacrylate Resin Rigid Polyurethane 70 (RPU 70) in Digital Light Synthesis (DLS). *Addit. Manuf.* **2021**, *37*, 101677. https://doi.org/10.1016/J.ADDMA.2020.101677.

(100) Li, X.; Yu, R.; He, Y.; Zhang, Y.; Yang, X.; Zhao, X.; Huang, W. Self-Healing Polyurethane Elastomers Based on a Disulfide Bond by Digital Light Processing 3D Printing. *ACS Macro Lett.* **2019**, *8* (11), 1511–1516. https://doi.org/10.1021/acsmacrolett.9b00766.

(101) Dolinski, N. D.; Page, Z. A.; Benjamin Callaway, E.; Eisenreich, F.; Garcia, R. V; Chavez, R.; Bothman, D. P.; Hecht, S.; Zok, F. W.; Hawker, C. J.; Dolinski, N. D.; Callaway, E. B.; Zok, F. W.; Hawker, C. J.; Page, Z. A.; Eisenreich, F.; Garcia, R. V; Chavez, R.; Hecht, S.; Bothman, D. P. Solution Mask Liquid Lithography (SMaLL) for One-Step, Multimaterial 3D Printing. *Adv. Mater.* **2018**, *30* (31), 1800364. https://doi.org/10.1002/ADMA.201800364.

(102) Schwartz, J. J.; Boydston, A. J. Multimaterial Actinic Spatial Control 3D and 4D Printing. **2019**, *10* (1). https://doi.org/10.1038/s41467-019-08639-7.

(103) Kuang, X.; Wu, J.; Chen, K.; Zhao, Z.; Ding, Z.; Hu, F.; Fang, D.; Qi, H. J. Grayscale Digital Light Processing 3D Printing for Highly Functionally Graded Materials. *Sci. Adv.* **2019**, *5* (5). https://doi.org/10.1126/sciadv.aav5790.

(104) Peterson, G. I.; Schwartz, J. J.; Zhang, D.; Weiss, B. M.; Ganter, M. A.; Storti, D. W.; Boydston, A. J. Production of Materials with Spatially-Controlled Cross-Link Density via Vat Photopolymerization. **2016**. https://doi.org/10.1021/acsami.6b09768.

(105) Joo, H.; Cho, S. Comparative Studies on Polyurethane Composites Filled with Polyaniline and Graphene for DLP-Type 3D Printing. *Polym. 2020, Vol. 12, Page 67* **2020**, *12* (1), 67. https://doi.org/10.3390/POLYM12010067.

(106) Li, V. C. F.; Kuang, X.; Mulyadi, A.; Hamel, C. M.; Deng, Y.; Qi, H. J. 3D Printed Cellulose Nanocrystal Composites through Digital Light Processing. *Cellulose* **2019**, *26* (6), 3973–3985. https://doi.org/10.1007/s10570-019-02353-9.

(107) Zhao, J.; Li, Q.; Jin, F.; He, N. Digital Light Processing 3D Printing Kevlar Composites Based on Dual Curing Resin. *Addit. Manuf.* **2021**, *41*, 101962. https://doi.org/10.1016/J.ADDMA.2021.101962.

(108) Al Rashid, A.; Ahmed, W.; Khalid, M. Y.; Koç, M. Vat Photopolymerization of Polymers and Polymer Composites: Processes and Applications. *Additive Manufacturing*. Elsevier November 1, 2021, p 102279. https://doi.org/10.1016/j.addma.2021.102279.

(109) Asif, S.; Chansoria, P.; Shirwaiker, R. Ultrasound-Assisted Vat Photopolymerization 3D Printing of Preferentially Organized Carbon Fiber Reinforced Polymer Composites. *J. Manuf. Process.* **2020**, *56*, 1340–1343. https://doi.org/10.1016/J.JMAPRO.2020.04.029.

(110) Malas; Isakov; Couling; Gibbons. Fabrication of High Permittivity Resin Composite for Vat Photopolymerization 3D Printing: Morphology, Thermal, Dynamic Mechanical and Dielectric Properties. *Materials (Basel).* **2019**, *12* (23), 3818. https://doi.org/10.3390/ma12233818.

(111) Kyle, S.; Jessop, Z. M.; Al-Sabah, A.; Whitaker, I. S. *'Printability'' of Candidate Biomaterials for Extrusion Based 3D Printing: State-of-the-Art';* Wiley-VCH Verlag, 2017; Vol. 6, p 1700264. https://doi.org/10.1002/adhm.201700264.

(112) Ouyang, L.; Yao, R.; Mao, S.; Chen, X.; Na, J.; Sun, W. Three-Dimensional Bioprinting of Embryonic Stem Cells Directs Highly Uniform Embryoid Body Formation. *Biofabrication* **2015**, *7*, 44101. https://doi.org/10.1088/1758-5090/7/4/044101.

(113) Narayanan, L. K.; Huebner, P.; Fisher, M. B.; Spang, J. T.; Starly, B.; Shirwaiker, R. A. 3D-Bioprinting of Polylactic Acid (PLA) Nanofiber-Alginate Hydrogel Bioink Containing Human Adipose-Derived Stem Cells. *ACS Biomater. Sci. Eng.* **2016**, *2* (10), 1732–1742. https://doi.org/10.1021/acsbiomaterials.6b00196.

(114) Hong, S.; Sycks, D.; Chan, H. F.; Lin, S.; Lopez, G. P.; Guilak, F.; Leong, K. W.; Zhao, X. 3D Printing of Highly Stretchable and Tough Hydrogels into Complex, Cellularized Structures. *Adv. Mater.* **2015**, *27* (27), 4035–4040. https://doi.org/10.1002/adma.201501099.

(115) Bakarich, S. E.; Gorkin, R.; Panhuis, M. in het; Spinks, G. M. 4D Printing with Mechanically Robust, Thermally Actuating Hydrogels. *Macromol. Rapid Commun.* **2015**, *36* (12), 1211–1217. https://doi.org/10.1002/marc.201500079.

(116) Bootsma, K.; Fitzgerald, M. M.; Free, B.; Dimbath, E.; Conjerti, J.; Reese, G.; Konkolewicz, D.; Berberich, J. A.; Sparks, J. L. 3D Printing of an Interpenetrating Network Hydrogel Material with Tunable Viscoelastic Properties. *J. Mech. Behav. Biomed. Mater.* **2017**, *70*, 84–94. https://doi.org/10.1016/j.jmbbm.2016.07.020.

(117) Khalil, S.; Sun, W. Bioprinting Endothelial Cells with Alginate for 3D Tissue Constructs. *J. Biomech. Eng.* **2009**, *131* (11). https://doi.org/10.1115/1.3128729.

(118) Loebel, C.; Rodell, C. B.; Chen, M. H.; Burdick, J. A. Shear-Thinning and Self-Healing Hydrogels as Injectable Therapeutics and for 3D-Printing. *Nat. Protoc.* **2017**, *12* (8), 1521–1541. https://doi.org/10.1038/nprot.2017.053.

(119) Skardal, A.; Zhang, J.; McCoard, L.; Oottamasathien, S.; Prestwich, G. D. Dynamically Crosslinked Gold Nanoparticle - Hyaluronan Hydrogels. *Adv. Mater.* **2010**, *22* (42), 4736–4740. https://doi.org/10.1002/adma.201001436.

(120) Rodell, C. B.; Kaminski, A.; Burdick, J. A. Rational Design of Network Properties in Guest-Host Assembled and Shear-Thinning Hyaluronic Acid Hydrogels. https://doi.org/10.1021/bm401280z.

(121) Pescosolido, L.; Schuurman, W.; Malda, J.; Matricardi, P.; Alhaique, F.; Coviello, T.; Van Weeren, P. R.; Dhert, W. J. A.; Hennink, W. E.; Vermonden, T. Hyaluronic Acid and Dextran-Based Semi-IPN Hydrogels as Biomaterials for Bioprinting. *Biomacromolecules* **2011**, *12* (5), 1831–1838. https://doi.org/10.1021/bm200178w.

(122) Liu, I.-H.; Chang, S.-H.; Lin, H.-Y. Chitosan-Based Hydrogel Tissue Scaffolds Made by 3D Plotting Promotes Osteoblast Proliferation and Mineralization. *Biomed. Mater.* **2015**, *10* (3), 035004. https://doi.org/10.1088/1748-6041/10/3/035004.

(123) Yi, H.; Wu, L. Q.; Bentley, W. E.; Ghodssi, R.; Rubloff, G. W.; Culver, J. N.; Payne, G. F. Biofabrication with Chitosan. *Biomacromolecules*. November 2005, pp 2881–2894. https://doi.org/10.1021/bm050410l.

(124) Echalier, C.; Levato, R.; Mateos-Timoneda, M. A.; Castaño, O.; Déjean, S.; Garric, X.; Pinese, C.; Noël, D.; Engel, E.; Martinez, J.; Mehdi, A.; Subra, G. Modular Bioink for 3D Printing of Biocompatible Hydrogels: Sol–Gel Polymerization of Hybrid Peptides and Polymers. *RSC Adv.* **2017**, *7* (20), 12231–12235. https://doi.org/10.1039/C6RA28540F.

(125) Li, C.; Faulkner-Jones, A.; Dun, A. R.; Jin, J.; Chen, P.; Xing, Y.; Yang, Z.; Li, Z.; Shu, W.; Liu, D.; Duncan, R. R. Rapid Formation of a Supramolecular Polypeptide-DNA Hydrogel for In Situ Three-Dimensional Multilayer Bioprinting. *Angew. Chemie* **2015**, *127* (13), 4029–4033. https://doi.org/10.1002/ange.201411383.

(126) Lei, Z.; Wang, Q.; Wu, P. A Multifunctional Skin-like Sensor Based on a 3D Printed Thermo-Responsive Hydrogel. *Mater. Horizons* **2017**, *4* (4), 694–700. https://doi.org/10.1039/c7mh00262a.

(127) Zolfagharian, A.; Kouzani, A. Z.; Khoo, S. Y.; Moghadam, A. A. A.; Gibson, I.; Kaynak, A. Evolution of 3D Printed Soft Actuators. *Sensors and Actuators, A: Physical*. Elsevier B.V. October 15, 2016, pp 258–272. https://doi.org/10.1016/j.sna.2016.09.028.

(128) Zolfagharian, A.; Kouzani, A. Z.; Khoo, S. Y.; Gibson, I.; Kaynak, A. 3D Printed Hydrogel Soft Actuators. In *IEEE Region 10 Annual International Conference, Proceedings/TENCON*; Institute of Electrical and Electronics Engineers Inc., 2017; pp 2272–2277. https://doi.org/10.1109/TENCON.2016.7848433.

(129) Skardal, A.; Zhang, J.; McCoard, L.; Xu, X.; Oottamasathien, S.; Prestwich, G. D. Photocrosslinkable Hyaluronan-Gelatin Hydrogels for Two-Step Bioprinting. *Tissue Eng. - Part A* **2010**, *16* (8), 2675–2685. https://doi.org/10.1089/ten.tea.2009.0798.

(130) Pereira, R. F.; Bártolo, P. J. 3D Bioprinting of Photocrosslinkable Hydrogel Constructs. *Journal of Applied Polymer Science*. John Wiley and Sons Inc. December 1, 2015. https://doi.org/10.1002/app.42458.

(131) Liu, W.; Heinrich, M. A.; Zhou, Y.; Akpek, A.; Hu, N.; Liu, X.; Guan, X.; Zhong, Z.; Jin, X.; Khademhosseini, A.; Zhang, Y. S. Extrusion Bioprinting of Shear-Thinning Gelatin Methacryloyl Bioinks. *Adv. Healthc. Mater.* **2017**, *6* (12). https://doi.org/10.1002/adhm.201601451.

(132) Lee, B. H.; Shirahama, H.; Cho, N. J.; Tan, L. P. Efficient and Controllable Synthesis of Highly Substituted Gelatin Methacrylamide for Mechanically Stiff Hydrogels. *RSC Adv.* **2015**, *5* (128), 106094–106097. https://doi.org/10.1039/c5ra22028a.

(133) Lim, K. S.; Schon, B. S.; Mekhileri, N. V.; Brown, G. C. J.; Chia, C. M.; Prabakar, S.; Hooper, G. J.; Woodfield, T. B. F. New Visible-Light Photoinitiating System for Improved Print Fidelity in Gelatin-Based Bioinks. *ACS Biomater. Sci. Eng.* **2016**, *2* (10), 1752–1762. https://doi.org/10.1021/acsbiomaterials.6b00149.

(134) Ouyang, L.; Highley, C. B.; Rodell, C. B.; Sun, W.; Burdick, J. A. 3D Printing of Shear-Thinning Hyaluronic Acid Hydrogels with Secondary Cross-Linking. *ACS Biomater. Sci. Eng.* **2016**, *2* (10), 1743–1751.

(135) Montheil, T.; Maumus, M.; Valot, L.; Lebrun, A.; Martinez, J.; Amblard, M.; Noël, D.; Mehdi, A.; Subra, G. Inorganic Sol-Gel Polymerization for Hydrogel Bioprinting. *ACS Omega* **2020**. https://doi.org/10.1021/acsomega.9b03100.

(136) Skardal, A.; Zhang, J.; Prestwich, G. D. Bioprinting Vessel-like Constructs Using Hyaluronan Hydrogels Crosslinked with Tetrahedral Polyethylene Glycol Tetracrylates. *Biomaterials* **2010**, *31* (24), 6173–6181. https://doi.org/10.1016/j.biomaterials.2010.04.045.

(137) Bertassoni, L. E.; Cecconi, M.; Manoharan, V.; Nikkhah, M.; Hjortnaes, J.; Cristino, A. L.; Barabaschi, G.; Demarchi, D.; Dokmeci, M. R.; Yang, Y.; Khademhosseini, A. Hydrogel Bioprinted Microchannel Networks for Vascularization of Tissue Engineering Constructs. *Lab Chip* **2014**, *14* (13), 2202–2211. https://doi.org/10.1039/c4lc00030g.

(138) O'Bryan, C. S.; Bhattacharjee, T.; Niemi, S. R.; Balachandar, S.; Baldwin, N.; Ellison, S. T.; Taylor, C. R.; Sawyer, W. G.; Angelini, T. E. Three-Dimensional Printing with Sacrificial Materials for Soft Matter Manufacturing. *MRS Bull.* **2017**, *42* (8), 571–577. https://doi.org/10.1557/mrs.2017.167.

(139) Lee, A.; Hudson, A. R.; Shiwarski, D. J.; Tashman, J. W.; Hinton, T. J.; Yerneni, S.; Bliley, J. M.; Campbell, P. G.; Feinberg, A. W. 3D Bioprinting of Collagen to Rebuild Components of the Human Heart. *Science* **2019**, *365* (6452), 482–487. https://doi.org/10.1126/science.aav9051.

(140) Gorsche, C.; Griesser, M.; Gescheidt, G.; Moszner, N.; Liska, R. β-Allyl Sulfones as Addition–Fragmentation Chain Transfer Reagents: A Tool for Adjusting Thermal and Mechanical Properties of Dimethacrylate Networks. *Macromolecules* **2014**, *47* (21), 7327–7336. https://doi.org/10.1021/ma501550b.

(141) Gorsche, C.; Koch, T.; Moszner, N.; Liska, R. Exploring the Benefits of β-Allyl Sulfones for More Homogeneous Dimethacrylate Photopolymer Networks. *Polym. Chem.* **2015**, *6* (11), 2038–2047. https://doi.org/10.1039/C4PY01582G.

(142) Lamparth, I.; Wottawa, D.; Angermann, J.; Fässler, P.; Liska, R.; Catel, Y. Synthesis of Allyl Sulfones Bearing Urethane Groups as Efficient Addition-Fragmentation Chain Transfer Agents for the Development of Low-Shrinkage Composites. *Eur. Polym. J.* **2021**, *158*, 110672. https://doi.org/10.1016/J.EURPOLYMJ.2021.110672.

(143) Gorsche, C.; Seidler, K.; Knaack, P.; Dorfinger, P.; Koch, T.; Stampfl, J.; Moszner, N.; Liska, R. Rapid Formation of Regulated Methacrylate Networks Yielding Tough Materials for Lithography-Based 3D Printing. *Polym. Chem.* **2016**, *7* (11), 2009–2014. https://doi.org/10.1039/C5PY02009C.

(144) Gorsche, C.; Seidler, K.; Harikrishna, R.; Kury, M.; Koch, T.; Moszner, N.; Liska, R. Difunctional Vinyl Sulfonate Esters for the Fabrication of Tough Methacrylate-Based Photopolymer Networks. *Polymer* **2018**, *158*, 149–157. https://doi.org/10.1016/J.POLYMER.2018.10.024.

(145) Schoerpf, S.; Catel, Y.; Moszner, N.; Gorsche, C.; Liska, R. Enhanced Reduction of Polymerization-Induced Shrinkage Stress via Combination of Radical Ring Opening and

Addition Fragmentation Chain Transfer. *Polym. Chem.* **2019**, *10* (11), 1357–1366. https://doi.org/10.1039/C8PY01540F.

(146) Griesser, M.; arkus Kury, M.; Harikrishna, R.; Dorfinger, P.; Koch, T.; Svirkova, A.; Marchetti-Deschmann, M.; Stampfl, J.; Moszner, N.; hristian Gorsche, C.; Robert Liska, and; Seidler, D.; Kury, M.; Harikrishna, R.; Gorsche, D.; Liska, R.; Griesser, D.; Dorfinger, D.; Koch, D. T.; Stampfl, J.; Svirkova, A.; Marchetti-Deschmann, M.; Moszner, N.; Harikrishna, D. R.; orsche, D. Vinyl Sulfonate Esters: Efficient Chain Transfer Agents for the 3D Printing of Tough Photopolymers without Retardation. *Angew. Chemie Int. Ed.* **2018**, *57* (29), 9165–9169. https://doi.org/10.1002/ANIE.201803747.

(147) Peer, G.; Eibel, A.; Gorsche, C.; Catel, Y.; Gescheidt, G.; Moszner, N.; Liska, R. Ester-Activated Vinyl Ethers as Chain Transfer Agents in Radical Photopolymerization of Methacrylates. *Macromolecules* **2019**, *52* (7), 2691–2700. https://doi.org/10.1021/acs.macromol.9b00085.

(148) Moad, C. L.; Moad, G.; Rizzardo, E.; Thang, S. H. Chain Transfer Activity of ω-Unsaturated Methyl Methacrylate Oligomers. *Macromolecules* **1996**, *29* (24), 7717–7726. https://doi.org/10.1021/ma960852c.

(149) Moad, G.; Rizzardo, E.; Thang, S. H. Radical Addition–Fragmentation Chemistry and RAFT Polymerization. *Ref. Modul. Mater. Sci. Mater. Eng.* **2016**. https://doi.org/10.1016/B978-0-12-803581-8.01349-7.

(150) Meijs, G. F.; Rizzardo, E.; Thang, S. H. Chain Transfer Activity of Some Activated Allylic Compounds. *Polym. Bull. 1990 245* **1990**, *24* (5), 501–505. https://doi.org/10.1007/BF00395571.

(151) Sato, E.; Uehara, I.; Horibe, H.; Matsumoto, A. One-Step Synthesis of Thermally Curable Hyperbranched Polymers by Addition–Fragmentation Chain Transfer Using Divinyl

Monomers. *Macromolecules* **2014**, *47* (3), 937–943. https://doi.org/10.1021/MA402300Z.

(152) Moad, G. Terminology in Reversible Deactivation Radical Polymerization (RDRP) and Reversible Addition–Fragmentation Chain Transfer (RAFT) Polymerization. In *RAFT Polymerization*; John Wiley & Sons, Ltd, 2021; pp 15–24. https://doi.org/10.1002/9783527821358.ch2.

(153) Penczek, S.; Moad, G.; Barón, M.; Hatada, K.; Hess, M.; Jenkins, A. D.; Jones, R. G.; Kahovec, J.; Kratochvíl, P.; Kubisa, P.; Maréchal, E.; Stepto, R. F. T.; Vairon, J. P.; Vohlídal, J.; Wilks, E. S. Glossary of Terms Related to Kinetics, Thermodynamics, and Mechanisms of Polymerization (IUPAC Recommendations 2008). *Pure Appl. Chem.* **2008**, *80* (10), 2163–2193. https://doi.org/10.1351/PAC200880102163/MACHINEREADABLECITATION/RIS.

(154) Amamoto, Y.; Kamada, J.; Otsuka, H.; Takahara, A.; Matyjaszewski, K.; Amamoto, Y.; Kamada, J.; Matyjaszewski, K.; Otsuka, H.; Takahara, A. Repeatable Photoinduced Self-Healing of Covalently Cross-Linked Polymers through Reshuffling of Trithiocarbonate Units. *Angew. Chemie Int. Ed.* **2011**, *50* (7), 1660–1663. https://doi.org/10.1002/ANIE.201003888.

(155) Cuthbert, J.; Zhang, T.; Biswas, S.; Olszewski, M.; Shanmugam, S.; Fu, T.; Gottlieb, E.; Kowalewski, T.; Balazs, A. C.; Matyjaszewski, K. Structurally Tailored and Engineered Macromolecular (STEM) Gels as Soft Elastomers and Hard/Soft Interfaces. *Macromolecules* **2018**, *51* (22), 9184–9191. https://doi.org/10.1021/acs.macromol.8b01880.

(156) Shanmugam, S.; Cuthbert, J.; Flum, J.; Fantin, M.; Boyer, C.; Kowalewski, T.; Matyjaszewski, K. Transformation of Gels via Catalyst-Free Selective RAFT Photoactivation. *Polym. Chem.* **2019**, *10* (19), 2477–2483. https://doi.org/10.1039/C9PY00213H.

(157) Fenoli, C. R.; Bowman, C. N. Synthesis of Novel Trithiocarbonate and Allyl Sulfide Containing Monomers. *Polym. Chem.* **2013**, *5* (1), 62–68. https://doi.org/10.1039/C3PY00709J.

(158) Fenoli, C. R.; Wydra, J. W.; Bowman, C. N. Controllable Reversible Addition–Fragmentation Termination Monomers for Advances in Photochemically Controlled Covalent Adaptable Networks. *Macromolecules* **2014**, *47* (3), 907–915. https://doi.org/10.1021/MA402548E.

(159) Park, H. Y.; Kloxin, C. J.; Fordney, M. F.; Bowman, C. N. Stress Relaxation of Trithiocarbonate-Dimethacrylate-Based Dental Composites. *Dent. Mater.* **2012**, *28* (8), 888–893. https://doi.org/10.1016/j.dental.2012.04.016.

(160) Park, H. Y.; Kloxin, C. J.; Abuelyaman, A. S.; Oxman, J. D.; Bowman, C. N. Stress Relaxation via Addition-Fragmentation Chain Transfer in High T g, High Conversion Methacrylate-Based Systems. *Macromolecules* **2012**, *45* (14), 5640–5646. https://doi.org/10.1021/ma300228z.

(161) Park, H. Y.; Kloxin, C. J.; Fordney, M. F.; Bowman, C. N. Stress Reduction and T g Enhancement in Ternary Thiol-Yne-Methacrylate Systems via Addition-Fragmentation Chain Transfer. *Macromolecules* **2012**, *45* (14), 5647–5652. https://doi.org/10.1021/ma300225q.

(162) Kloxin, C. J.; Bowman, C. N. Covalent Adaptable Networks: Smart, Reconfigurable and Responsive Network Systems. *Chem. Soc. Rev.* **2013**, *42* (17), 7161–7173. https://doi.org/10.1039/C3CS60046G.

(163) Fang, H.; Guymon, C. A. Recent Advances to Decrease Shrinkage Stress and Enhance Mechanical Properties in Free Radical Polymerization: A Review. *Polym. Int.* **2021**. https://doi.org/10.1002/PI.6341.

(164) Scott, T. F.; Schneider, A. D.; Cook, W. D.; Bowman, C. N. Chemistry: Photoinduced Plasticity in Cross-Linked Polymers. *Science* **2005**, *308* (5728), 1615–1617. https://doi.org/10.1126/science.1110505.

(165) Sowan, N.; Song, H. B.; Cox, L. M.; Patton, J. R.; Fairbanks, B. D.; Ding, Y.; Bowman, C. N. Light-Activated Stress Relaxation, Toughness Improvement, and Photoinduced Reversal of Physical Aging in Glassy Polymer Networks. *Adv. Mater.* **2021**, *33* (5), 2007221. https://doi.org/10.1002/adma.202007221.

(166) Otsu, T.; Yoshida, M.; Kuriyama, A. Living Radical Polymerizations in Homogeneous Solution by Using Organic Sulfides as Photoiniferters. *Polym. Bull. 1982 71* **1982**, *7* (1), 45–50. https://doi.org/10.1007/BF00264156.

(167) Otsu, T. Iniferter Concept and Living Radical Polymerization. *J. Polym. Sci., Part A Polym. Chem* **2000**, *38* (12), 2121–2136. https://doi.org/10.1002/(SICI)1099-0518(20000615)38:12.

(168) Luo, N.; Metters, A. T.; Hutchison, J. B.; Bowman, C. N.; Anseth, K. S. A Methacrylated Photoiniferter as a Chemical Basis for Microlithography: Micropatterning Based on Photografting Polymerization. *Macromolecules* **2003**, *36* (18), 6739–6745. https://doi.org/10.1021/MA0344341.

(169) Luo, N.; Brian Hutchison, J.; Anseth, K. S.; Bowman, C. N. Synthesis of a Novel Methacrylic Monomer Iniferter and Its Application in Surface Photografting on Crosslinked Polymer Substrates. *J. Polym. Sci. Part A Polym. Chem.* **2002**, *40* (11), 1885–1891. https://doi.org/10.1002/POLA.10272.

(170) Moad, G. A Critical Survey of Dithiocarbamate Reversible Addition-Fragmentation Chain Transfer (RAFT) Agents in Radical Polymerization. *J. Polym. Sci. Part A Polym. Chem.* **2019**, *57* (3), 216–227. https://doi.org/10.1002/POLA.29199.

(171) Hutchison, J. B.; Haraldsson, K. T.; Good, B. T.; Sebra, R. P.; Luo, N.; Anseth, K. S.; Bowman, C. N. Robust Polymer Microfluidic Device Fabrication via Contact Liquid Photolithographic Polymerization (CLiPP). *Lab Chip* **2004**, *4* (6), 658–662. https://doi.org/10.1039/B405985A.

(172) Haraldsson, K. T.; Hutchison, J. B.; Sebra, R. P.; Good, B. T.; Anseth, K. S.; Bowman, C. N. 3D Polymeric Microfluidic Device Fabrication via Contact Liquid Photolithographic Polymerization (CLiPP). *Sensors Actuators B Chem.* **2006**, *113* (1), 454–460. https://doi.org/10.1016/J.SNB.2005.03.096.

(173) Zhou, H.; Johnson, J. A. Photo-Controlled Growth of Telechelic Polymers and End-Linked Polymer Gels. *Angew. Chemie Int. Ed.* **2013**, *52* (8), 2235–2238. https://doi.org/10.1002/ANIE.201207966.

(174) Otsu, T.; Yoshida, M.; Tazaki, T. A Model for Living Radical Polymerization. *Die Makromol. Chemie, Rapid Commun.* **1982**, *3* (2), 133–140. https://doi.org/10.1002/MARC.1982.030030209.

(175) Quinn, J. F.; Barner, L.; Barner-Kowollik, C.; Rizzardo, E.; Davis, T. P. Reversible Addition−Fragmentation Chain Transfer Polymerization Initiated with Ultraviolet Radiation. *Macromolecules* **2002**, *35* (20), 7620–7627. https://doi.org/10.1021/ma0204296.

(176) Lamb, J. R.; Qin, K. P.; Johnson, J. A. Visible-Light-Mediated, Additive-Free, and Open-to-Air Controlled Radical Polymerization of Acrylates and Acrylamides. *Polym. Chem.* **2019**, *10* (13). https://doi.org/10.1039/c9py00022d.

(177) Fu, Q.; Xie, K.; McKenzie, T. G.; Qiao, G. G. Trithiocarbonates as Intrinsic Photoredox Catalysts and RAFT Agents for Oxygen Tolerant Controlled Radical Polymerization. *Polym. Chem.* **2017**, *8* (9), 1519–1526. https://doi.org/10.1039/C6PY01994C.

(178) Li, J.; Ding, C.; Zhang, Z.; Pan, X.; Li, N.; Zhu, J.; Zhu, X. Visible Light-Induced Living Radical Polymerization of Butyl Acrylate: Photocatalyst-Free, Ultrafast, and Oxygen Tolerance. *Macromol. Rapid Commun.* **2017**, *38* (13), 1600482. https://doi.org/10.1002/MARC.201600482.

(179) Xu, J.; Shanmugam, S.; Fu, C.; Aguey-Zinsou, K. F.; Boyer, C. Selective Photoactivation: From a Single Unit Monomer Insertion Reaction to Controlled Polymer Architectures. *J. Am. Chem. Soc.* **2016**, *138* (9), 3094–3106. https://doi.org/10.1021/jacs.5b12408.

(180) Bellotti, V.; Simonutti, R. New Light in Polymer Science: Photoinduced Reversible Addition-Fragmentation Chain Transfer Polymerization (PET-RAFT) as Innovative Strategy for the Synthesis of Advanced Materials. *Polym. 2021, Vol. 13, Page 1119* **2021**, *13* (7), 1119. https://doi.org/10.3390/POLYM13071119.

(181) Bagheri, A.; Bainbridge, C. W. A.; Engel, K. E.; Qiao, G. G.; Xu, J.; Boyer, C.; Jin, J. Oxygen Tolerant PET-RAFT Facilitated 3D Printing of Polymeric Materials under Visible LEDs. *ACS Appl. Polym. Mater.* **2020**, *2* (2), 782–790. https://doi.org/10.1021/acsapm.9b01076.

(182) Bobrin, V. A.; Lee, K.; Zhang, J.; Corrigan, N.; Boyer, C.; Bobrin, V. A.; Lee, K.; Corrigan, N.; Boyer, C.; Zhang, J. Nanostructure Control in 3D Printed Materials. *Adv. Mater.* **2021**, 2107643. https://doi.org/10.1002/ADMA.202107643.

(183) Xiaobing Shi; Jin Zhang; Nathaniel Corrigan; Cyrille Boyer. Controlling Mechanical Properties of 3D Printed Polymer Composites through Photoinduced Reversible Addition–Fragmentation Chain Transfer (RAFT) Polymerization. *Polym. Chem.* **2021**, *13* (1), 44–57. https://doi.org/10.1039/D1PY01283E.

(184) Zhang, Z.; Corrigan, N.; Boyer, C. Effect of Thiocarbonylthio Compounds on Visible-Light-Mediated 3D Printing. *Macromolecules* **2021**, *54* (3), 1170–1182. https://doi.org/10.1021/acs.macromol.0c02691.

(185) Zhang, Z.; Corrigan, N.; Bagheri, A.; Jin, J.; Boyer, C. A Versatile 3D and 4D Printing System through Photocontrolled RAFT Polymerization. **2019**, No. 50.

(186) Zhang, Z.; Corrigan, N.; Boyer, C. A Photoinduced Dual-Wavelength Approach for 3D Printing and Self-Healing of Thermosetting Materials. *Angew. Chemie Int. Ed.* **2021**. https://doi.org/10.1002/ANIE.202114111.

(187) Kottisch, V.; Michaudel, Q.; Fors, B. P. Cationic Polymerization of Vinyl Ethers Controlled by Visible Light. *J. Am. Chem. Soc.* **2016**, *138* (48), 15535–15538. https://doi.org/10.1021/jacs.6b10150.

(188) Michaudel, Q.; Kottisch, V.; Fors, B. P. Photocontrolled Polymerization Cationic Polymerization:F Rom Photoinitiation to Photocontrol. https://doi.org/10.1002/ange.201701425.

(189) Kottisch, V.; Michaudel, Q.; Fors, B. P. Photocontrolled Interconversion of Cationic and Radical Polymerizations. *J. Am. Chem. Soc.* **2017**, *139* (31), 10665–10668. https://doi.org/10.1021/jacs.7b06661.

(190) Ma, Y.; Kottisch, V.; McLoughlin, E. A.; Rouse, Z. W.; Supej, M. J.; Baker, S. P.; Fors, B. P. Photoswitching Cationic and Radical Polymerizations: Spatiotemporal Control of Thermoset Properties. *J. Am. Chem. Soc.* **2021**, *143* (50), 21200–21205. https://doi.org/10.1021/JACS.1C09523.

Chapter 2 Tough and Degradable 3D Printed Acrylic Photopolymer Resins with Crosslinkers Capable of Mediating Reversible Addition–Fragmentation Chain Transfer (RAFT)

2.1 Introduction

Acrylic photopolymer resins are an important class of material that plays relevant roles in a variety of industries, such as coatings,[1–3] adhesives[4–7] and, more recently, additive manufacturing[8–16]. Resins with low viscosity when uncured and high toughness when cured are highly desirable for a range of applications, especially additive manufacturing[17]. However, this combination of properties remains a challenge as the need for low viscosity calls for low molecular weight monomers and crosslinkers, which tends to cure into highly crosslinked and brittle networks. In addition, acrylic photopolymer networks possess inhomogeneous features that also negatively impact their mechanical properties.[18–21] Acrylic moieties can form high molecular weight vinyl chains in the early stages of the photopolymerization process, resulting in domains with high crosslinking density, while polymerization in later stages of the curing process is severely limited by slow diffusion due to gelation.[18,22] Such irregularities in the network also impacts the toughness of the network, as not all the polymer chains are stressed uniformly and some fail sooner than others.

To mitigate these irregularities, chain transfer agents (CTAs) have been incorporated in photopolymers to control the rate and kinetic chain length during curing.[23,24] Controlling the fast growth of long vinyl chains serves to discourage the formation of domains of high crosslinking density and low elasticity, resulting in a more homogenous network that can better distribute stress. Specifically, addition fragmentation chain transfer (AFCT) reagents such as β-allyl sulfides have been employed in photopolymer networks with great success for reducing shrinkage stress and improve toughness.[25–27]

Reversible addition–fragmentation chain transfer (RAFT) [28–30]is a special case of AFCT in which, instead of being single-use, the CTAs are capable of undergoing multiple reversible AFT events, rendering living characteristics to the system. RAFT has the benefit of maintaining continuous control throughout the polymerization process (as opposed to irreversible AFCT agents which can be depleted). In addition, the introduction of RAFT agents into the network allows for the dynamic rearrangement of the network under certain conditions, giving rise to properties such as stress reduction and photoplasticity.[31–33] RAFT agents in the network can also act as reaction handles for

further modification to the network, such as functionalization, monomer insertion, and degradation.[10,34,35]

In most reports so far the introduction of RAFT agents into a photopolymer network is achieved by adding the reagent as a standalone additive.[10,19,35,36] Another compelling strategy for the insertion of RAFT agents is by functionalizing them with reactive moieties, making them RAFT-capable crosslinkers. These crosslinkers, while retaining all the functions of the RAFT agent, can also introduce interesting new topological features into the network. A topological effect of the RAFT process is that monomers are inserted between the RAFT agent and its side chain(s), which causes the reactive moieties on either ends of the crosslinker to move away from each other, which may have implications on the molecular weight between crosslinks in the network. This class of RAFT-capable crosslinkers has been studied by Bowman and co-workers. in the context of methacrylic and thiol-acrylic photopolymer resins.[32,37,38] They demonstrated that with a low loading (<10% wt) of the RAFT-capable crosslinkers in the system, stress relaxation can be achieved in the network through AFCT-induced chain rearrangement during and after the photopolymerization process. However, the effect of these crosslinkers on network topology, especially at higher loadings, and the subsequent implications on the mechanical properties of the materials remain open and relevant questions.

Herein we used a symmetric trithiocarbonate with acrylate side chains as a model to study the behavior of crosslinkers capable of mediating RAFT in an acrylic photopolymer resin. As it possesses properties of both a CTA and a crosslinker, it will be referred to as a “transferinker” (TFK). We employed kinetic Monte Carlo simulation to describe the effect of TFKs on network topology, and the downstream impact of TFKs on the mechanical and degradation properties of the cured resins is investigated experimentally.

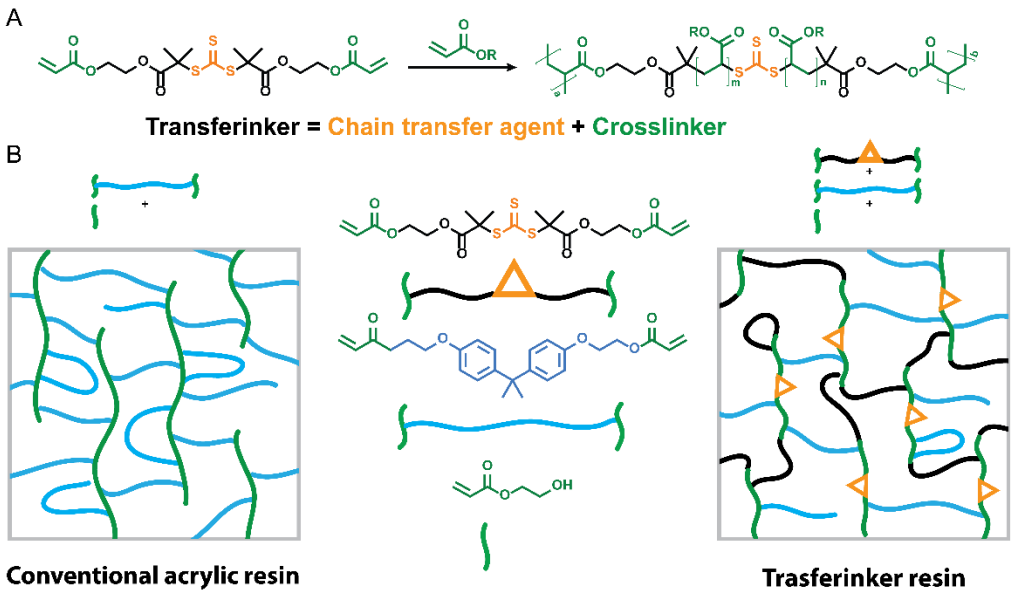

Figure 2-1 A transferinker(TFK) is a crosslinker bearing a moiety capable of mediating chain transfer. A) Proposed working mechanism of a model TFK bearing a trithiocarbonate moiety and B) the altered network architecture in a photopolymer resin formulated with TFKs.

2.2 Results and discussion

2.2.1 Synthesis and formulation of TFK and TTC resins

The TFK molecule **TFKDA** was designed and synthesized as described in **Figure 2-2**A. For control studies, **TTCDG**, a trithiocarbonate analogue without acrylates on its side chains was also designed and synthesized (**Figure 2-2**B). To study the effect of TFKs in acrylic photopolymer resins, we gradually replaced the crosslinkers with **TFKDA** in an acrylic photopolymer formulation(**Table 2-1**). The base resin was formulated with bisphenol A ethoxylate diacrylate (BPAEDA, Avg.MW 512) as the crosslinker and hydroxyethyl acrylate (HEA) as the functional diluent. BPAEDA was chosen as it is commonly used in photopolymer resins, and has a similar molecular weight to **TFKDA**, therefore replacing it with the latter will not cause a significant change in acrylate concentration and glass transition temperature. Phenylbis(2,4,6-trimethylbenzoyl) phosphine oxide (BAPO) was used as photoinitiator. TFK resins were

formulated by replacing 5%, 15% or 25% of BPAEDA with **TFKDA**. They are correspondingly named **TFK5**, **TFK15**, and **TFK25**.

As control, TTC resins are formulated by adding non-crosslinkable **TTCDG** into the base resin such that the molar ratio between the monoacrylate and diacrylate species and the molar ratio between TTCs and acrylates matches a given TFK resin. For example, **TFK25** resin and **TTC25** resin both have a 1:1 ratio of monoacrylate and diacrylate species, and an 85:1000 ratio of TTCs to acrylates.

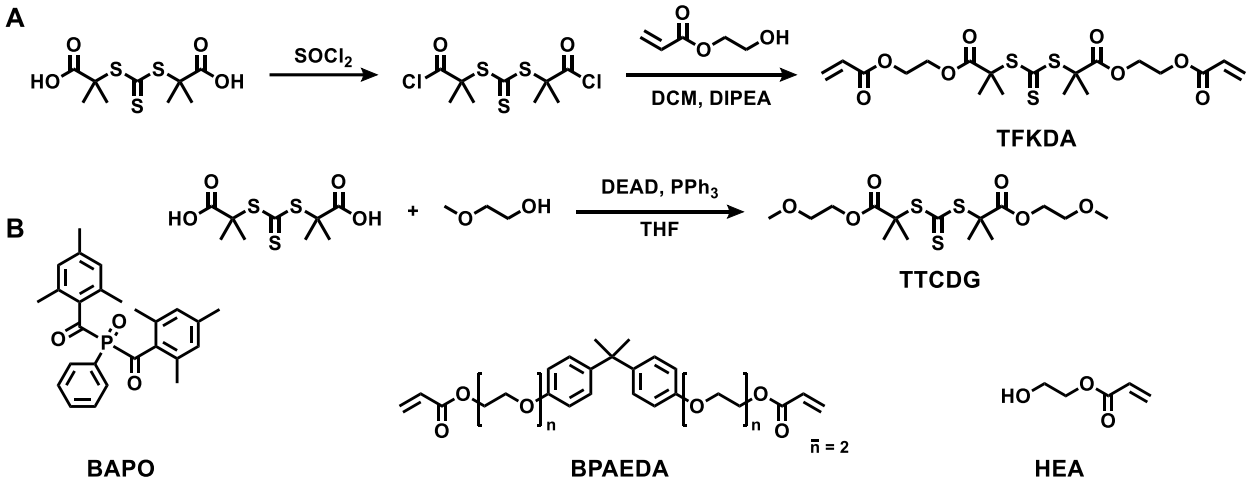

Figure 2-2 Chemical species used in this study. A) Synthesis of transferinker **TFKDA** and a non-polymerizable analogue **TTCDG**. B) Structure of the photoinitiator (Phenylbis(2,4,6-trimethylbenzoyl) phosphine oxide, BAPO), crosslinker (Bisphenol A ethoxylate diacrylate, BPAEDA, avg. M_n ~ 512), and functional diluent (2-Hydroxyethyl acrylate, HEA) used in TFK and TTC resin formulations.

Table 2-1 Formulation of TFK and TTC resins

Resin	Monomer	:	Crosslinker	:	BAPO	:	TFKDA	:	TTCDG
TFK0	80	:	80	:	1	:	0	:	0
TFK5	80	:	76	:	1	:	4	:	0
TFK15	80	:	68	:	1	:	12	:	0
TFK25	80	:	60	:	1	:	20	:	0
TTC0	80	:	80	:	1	:	0	:	0
TTC5	80	:	80	:	1	:	0	:	4
TTC15	80	:	80	:	1	:	0	:	12
TTC25	80	:	80	:	1	:	0	:	20

2.2.2 Curing kinetics of TFK resins

Chain transfer agents such as TTCs are known to cause retardation to curing of acrylic systems. The curing kinetics of the TFK resins were studied with FTIR under a 405nm LED light source with a light intensity of 1.95mW/cm^2.(**Figure 2-11**) The rate of polymerization for **TFK5** was similar to that for **TFK0**. Vinyl bond conversion for both increased rapidly immediately upon irradiation, before reaching a plateau of around 80% at 3min. **TFK15** and **TFK25** showed a noticeable inhibition period indicated by slow initial increase in conversion. **TFK15** and **TFK25** resin reached plateaus in conversion after 7min an 11min, respectively. Final conversion of **TFK15** (81%) and **TFK25** (85%) were slightly lower than that for **TFK0** and **TFK5** (87%). The inhibition effect of TTC compounds could be ascribed to the low initiation ability of the initial leaving group from the TTC compound, as well as the fragmentation of the TTC radical and the light absorbance of the TTC compounds.

2.2.3 Mechanical properties of TFK resins

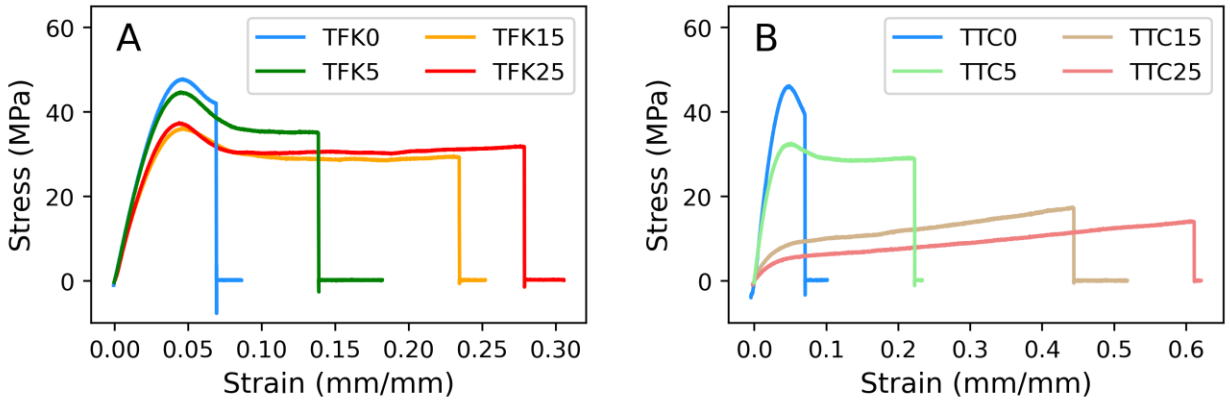

Figure 2-3 Representative stress-strain curve of samples cured from A) TFK resins and B) TTC resins.

TFK resins were cast into dogbone shaped samples and their mechanical properties were characterized with tensile testing. Stress-strain curves of TFK resins are shown in Figure 2-3. Young's Modulus of **TFK0** resin is ~1500 MPa which is typical for acrylic resins of similar composition. Modulus for **TFK5** resin is of a similar value. **TFK15** and **TFK25** have slightly lower moduli at ~1200 MPa, representing a 20% decrease. Ultimate tensile strength follows a similar trend, with **TFK0** and **TFK5** having similar performance at 45MPa, while **TFK15** and **TFK25** retain 80% of that value. In contrast, TTC resins lose much more of their stiffness. **TTC5** samples show a 14% loss in modulus and 17% loss in ultimate tensile strength compared to **TTC0**/**TFK0**, consistent with previous observations in similar systems.[39] **TTC15** and **TTC25** samples have less than half the ultimate tensile strengths and less than 20% the moduli compared to their respective TFK counterparts. This could be attributed to the increased amount of dangling chains in TTC resins as observed in simulations *(vide infra)*. The dilution effect of TTCs may also play a role as, unlike TFKs, TTCs are added into the formulation without removing other components.

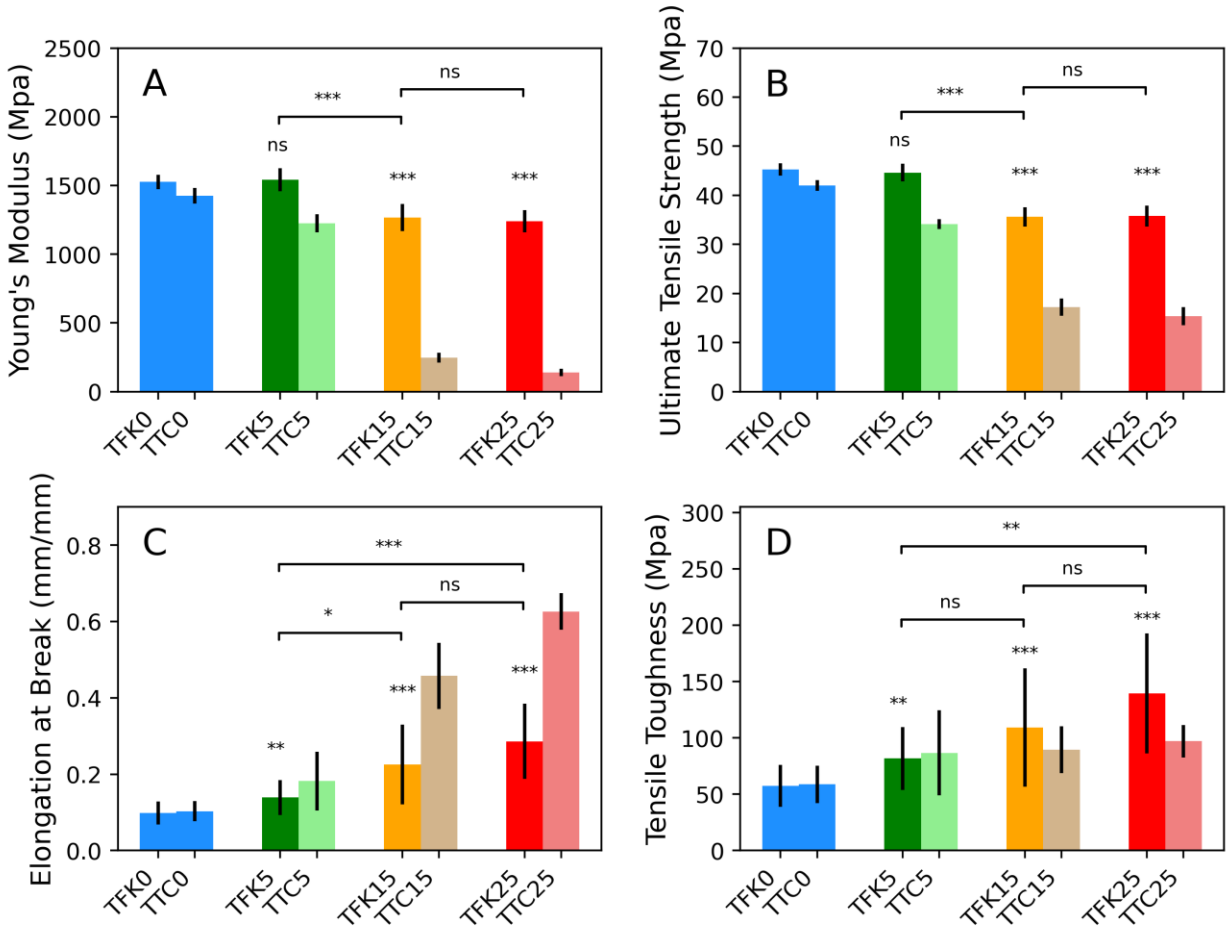

Figure 2-4 Tensile properties of TFK and TTC resins. A) Young's modulus; B) Ultimate tensile strength; C) Elongation at break; D) Tensile toughness. Error bar show standard deviation. Statistics performed using independent two-sample t-test with n = 25, comparing each TFK sample to **TFK0**, and in pairs among all TFK samples. ns: $p > 0.05$; *: $0.05 > p > 0.01$; **: $0.01 > p > 0.001$; ***: $p < 0.001$

Table 2-2 Tensile properties of TFK and TTC resins.

Resin	Young's Modulus (Mpa)	Ultimate Tensile Strength (Mpa)	Elongation at Break (%)	Toughness (Mpa)
TFK0	1525±53	45.3±1.3	9.8±3.0	57.3±18.6
TFK5	1541±85	44.6±1.8	13.9±4.6	81.7±27.9
TFk15	1267±99	35.6±2.0	22.6±10.4	109.1±52.5
TFK25	1239±81	35.8±2.1	28.6±9.9	139.6±53.3
TTC0	1425±57	42.0±1.1	10.3±2.6	58.7±16.6
TTC5	1224±67	34.1±1.0	18.1±7.7	86.7±37.7
TTC15	247±36	17.2±1.8	45.8±8.6	89.6±20.8
TTC25	139±27	15.4±1.9	62.6±4.8	97.0±14.5

Samples made from the base **TFK0** resin yields at ~5% elongation and fails soon after, consistent with hard glassy polymers. They have an average elongation at break of only 10% and a toughness of 52 MPa. Replacing 5% of crosslinkers for TFKs (**TFK5**) improved elongation at break and toughness by 50%. **TFK15** and **TFK25**, showed more improvements in toughness and elongation at break. Specifically, **TFK25** samples have an average toughness of 139MPa and elongation at break of 29%, representing an improvement of more than 100% in both properties.

Compared to the TFK resins, TTC resins (**Figure 2-3** B) show similar or less improvement in toughness, while being able to reach much longer elongation before failing. While **TTC5** samples still display a yield point, stress-strain curves of **TTC15** and **TTC25** samples do not and bear more resemblance to that of a rubbery elastomer. **TTC15** and **TTC25** samples reach an average elongation at break of 46% and 62% respectively, more than twice that of corresponding TFK

resins. The gain in elongation is offset by diminished modulus to result in similar performance in toughness.

There is a general tradeoff between strength and elongation. TFK resins trade very favorably in this regard by gaining up to 100% toughness while maintaining more than 80% of their strength compared to the base resin. TFK allows high loading of CTAs into a resin, while minimizing the negative effects of adding CTAs outright, such as dilution and increased amount of dangling chains. We think this strategy is not limited to trithiocarbonates but a wide variety of CTAs, reversible and irreversible alike.

2.2.4 3D printing of TFK resins

We demonstrated 3D printing with **TFK0** and **TFK5** resins on an Elegoo Mars Pro MSLA printer (**Figure 2-5** A). The resins are capable of printing with accurate dimensions, although some artifacts exist resulting from light diffusion due to the lack of a light blocker in the formulation.[8] Samples printed with **TFK0** and **TFK5** showed similar trends in mechanical properties compared to cast samples (**Figure 2-5** B and C).

To further explore the potential of TFKs as a general approach for toughening photopolymer resins, we doped 5% (w/w) of TFK into a commercial resin (Elegoo Standard white). We were able to print intricate models with the doped resin, which shows a distinctive yellow color. Compared to the unmodified resin, the doped resin requires longer irradiation time to cure (**Table 2-4**), but is capable of reproducing complex and detailed models, such as a submarine, shown in **Figure 2-5** D. Dogbones were printed with unmodified and doped resins and their mechanical properties compared, as shown in Figure. Resins doped with TFK showed significantly improved toughness (**Figure 2-5** E and F).

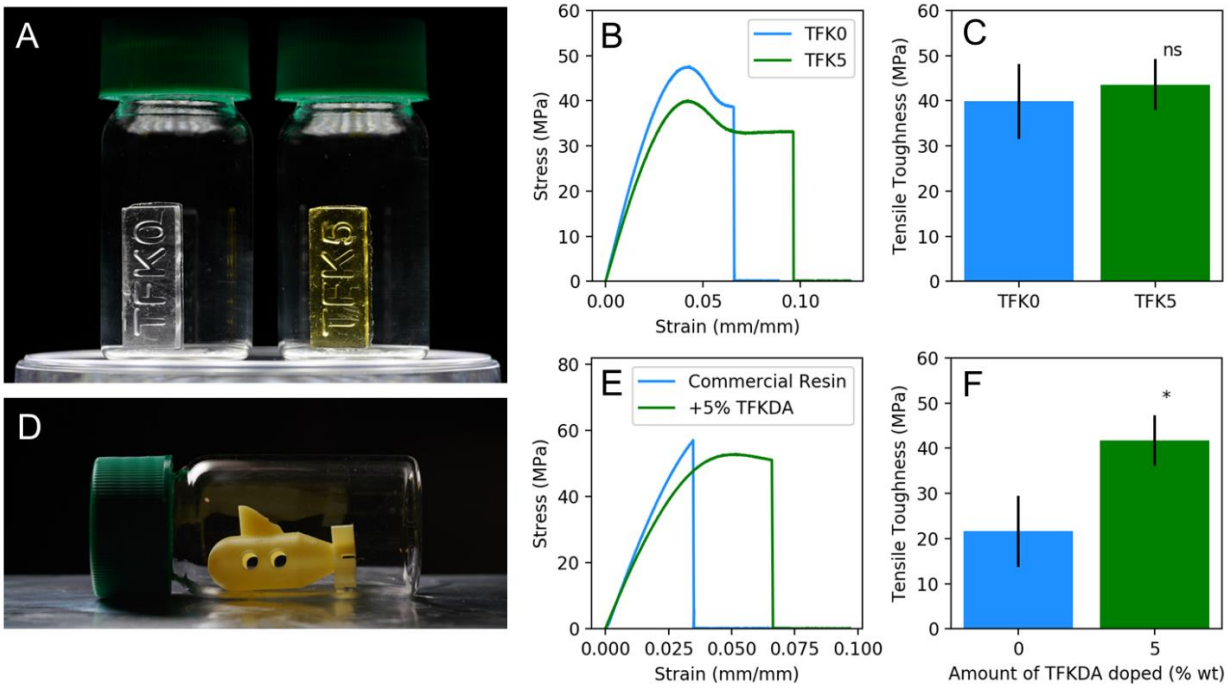

Figure 2-5 3D printing with TFK resins and doping commercial resin with **TFKDA**. A) Models printed with **TFK0** and **TFK5** resins, 20 mL vial for scale. B) Stress-strain curves of dogbone samples printed with **TFK0** and **TFK5**. C) Tensile toughness of 3D printed **TFK0** and **TFK5** samples. D) A model submarine printed with a commercial 3D printing photopolymer resin (Elegoo Standard White) doped with 5% wt of **TFKDA**. 20 mL vial for scale. E) Stress-strain curves of dogbone samples printed with commercial and doped resins. F) Tensile toughness of commercial and doped resins. Error bar show standard deviation. Statistics performed using independent two-sample t-test with n = 25, comparing each TFK sample to **TFK0**, and in pairs among all TFK samples. ns: $p > 0.05$; *: $0.05 > p > 0.01$.

2.2.5 Qualitative study of the effect of TFKs on network architecture with kinetic Monte Carlo simulation

To gain a more fundamental understanding of the effects TFKs have on these networks, we developed a simple software platform to simulate the formation of a network through crosslinking. The crosslinking process of a photopolymer can be considered a copolymerization between monomers and crosslinkers. Ting Xu and co-workers[40] reported a kinetic Monte Carlo simulation program that addresses the composition of copolymers produced by controlled radical polymerization (CRP). In the reported program, polymer chains are represented by empty lists, and chain propagation is modelled by appending different kinds of monomers into the chains according to their reactivity ratios. We adapted this method so that information pertaining to network architecture can be preserved and extracted after the simulation. Crosslinkers are represented by assigning some of the monomers in pairs. With the identity of one of the monomers in the pair, the identity and state of the other monomer can be looked up. As CTAs can rearrange the network, they need to be modelled as well. A chain transfer event can be seen as a CTA deactivating a chain and activating another one, thus a CTA can be represented simply as an inactive list. If chain transfer is determined to occur between an active chain and a CTA, the chain is deactivated and no longer participates in propagation, while the inactive chain on the CTA is activated. The probability of the occurrence of chain transfer on an active chain is determined by the concentration of CTAs and monomers, and the chain transfer constant of the CTA.

Compared to most CTAs, a TTC is special that it has two inactive chains. This can be represented by two lists associated with the TTC. Chain transfer can occur with either one of the chains being activated as the result. By the same concept of associating objects that are covalently attached to each other, more complex objects like TFKs can also be constructed. A TFK object contains a TTC with its two chains. Each chain is associated with a monomer representing the reactive side chain of the TFK. The TTC and the monomers all retain their aforementioned functions; the added associations between the objects denote their covalent bonding to one another. These associations preserve the information pertaining to the connectivity between molecules, which allows the entire network to be constructed after the simulation, as opposed to only the compositions of the vinyl chains.

As different species contribute different chain lengths to the network, the geometry of each species needs to be defined before the network could be reconstructed. (**Table 2-3**) The length of the monomer is set as 2, corresponding to the number of C-C bonds contributed to the network by an acrylate monomer. Similarly, length of a crosslinker is set as 16, and the length of a TTC is 2. A TFK contains a TTC object and two side chains; the length of side chains on a TFK is 7. Note that the total length of a TFK is equal to that of a crosslinker. These lengths can also be considered as molecular weights.

A series of simulations were set up to qualitatively assess the how TFKs affect the architecture of the network. The composition of the model systems are is listed in **Table 2-3**. We started from a composition of 5000 monomers, 5000 crosslinkers, 62 initiators and no TFKs. The molar ratio among all species found in this system matches that found in the **TFK0** resin. In subsequent model systems, 5%, 10%, and 25% of the crosslinkers are replaced with TFKs, maintaining the total number of difunctional species. Each model system matches a TFK resin formulation. As comparison, TTC systems are similarly set up with TTCs that lack the reactive side chains. As TTCs are not difunctional species, the number of crosslinkers is kept constant to maintain the total number of difunctional species. Each TTC system matches a TTC resin formulation. Simulations are repeated 10 times and the results are averaged. We also scaled the systems by a factor of 10 and obtained indistinguishable results, validating the statistical significance of the systems.

Molecular weight between crosslinks in a network is a parameter that is closely related to mechanical properties. To find all the elastic segments in the network, all crosslinkers are queried and those with both functionalities reacted are considered elastic crosslinkers. Points where an elastic crosslinker joins a vinyl chain is considered a crosslinking point. To obtain the molecular weight (or chain length) between crosslinks, all chain segments between crosslinking points are tallied and a length histogram of these chain segments is calculated and shown in **Figure 2-6**A. The length distribution of elastic segments is bimodal, with short segments along the vinyl chains and long segments contributed by crosslinkers. The addition of TFKs slightly changes this distribution, with less chains on the longer and shorter end of the spectrum and an emerging distribution of medium length chains corresponding to the length of the TFK's side chains.

Analogous to the way that number and weight average molecular weights are calculated from a distribution, the number and length average chain length can be calculated as the simple average and the ratio of the second to the first moment of the length distribution[41], respectively. (**Figure 2-6**B) As crosslinkers are replaced with TFKs, the number average length of elastic chain segments slightly increases while the length average decreases, resulting in lower dispersity.

Table 2-3 Compositions of models systems used in simulation. Each model system matches the composition of a TFK or TTC resin of the same name, found in **Table 2-1**. *a* TFKs consist of a TTC with length 2 and two side chains with length 7.

Species	**Monomer**	**Crosslinker**	**TTC**	**TFK**	**Initiator**
Length	2	16	2	7+2+7 = 16[a]	0
System	**Monomer**	**Crosslinker**	**Initiator**	**TFK**	**TTC**
TFK0	5000	5000	62	0	0
TFK5	5000	4750	62	250	0
TFK15	5000	4250	62	750	0
TFK25	5000	3750	62	1250	0
TTC0	5000	5000	62	0	0
TTC5	5000	5000	62	0	250
TTC15	5000	5000	62	0	750
TTC25	5000	5000	62	0	1250

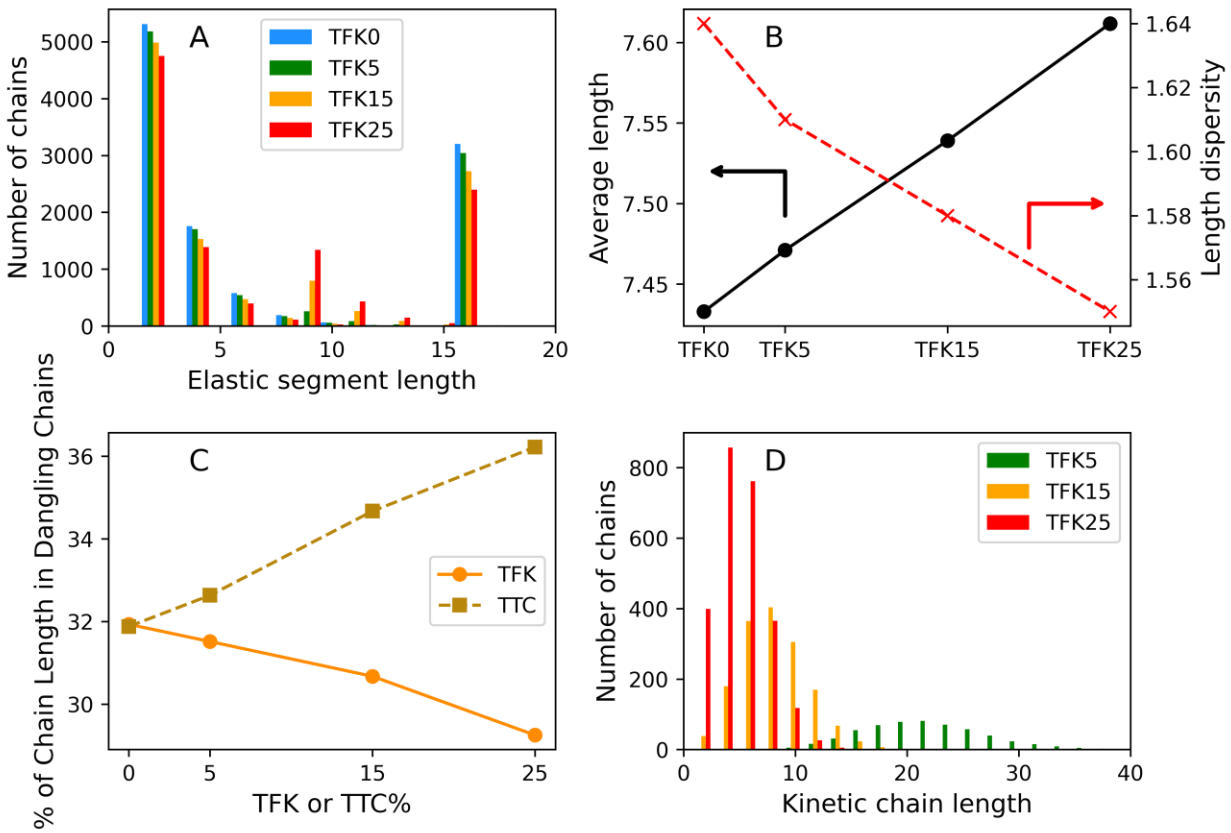

Figure 2-6 Network properties from simulation. A) Histogram of the length distribution of elastic segments in networks containing TFK. B) Average length and length dispersity of elastic segments in networks containing TFK. Length dispersity is defined as the quotient between the ratio of the second to the first moment of the length distribution and the average length, similar to the way dispersity is defined for molecular weight. C) Percentage of chain length trapped in dangling chains (and not contributing to elasticity) for networks containing TFK or TTC. Lower percentage mean less dangling chain ends. D) Histogram depicting the distribution of kinetic chain lengths in networks containing TFK.

As normal CTAs introduce more chains into the system, we wondered if they would also introduce a large number of dangling chain ends, which negatively impact the mechanical properties. The total length of dangling chain ends is obtained by subtracting the length of all segments that are crosslinked on both ends from the total length of all species. Less length in dangling chains suggests that more chain segments are contributing to elasticity. As crosslinkers are replaced with TFKs, we observed less chain length in dangling chains. (**Figure 2-6**C) In comparison, TTC resins show increased amount of chain lengths in dangling chains. TTC, like TFK, creates more vinyl chains through chain transfer and thus creates more chain ends. However, in a TFK resin the end of most of the chains are the reactive side chain of the TFK. This lessens the chance of the chain end becoming a dangling chain end as the TFK side chain can react and form a crosslink. In a TTC resin, the same number of chains are created, but as the end group of a TTC is unreactive, the large number of chain ends are more likely to become dangling.

We also investigated the kinetic chain lengths of the vinyl chains formed during the polymerization process. (**Figure 2-6**D) **TFK5**, **TFK15** and **TFK25** resins displayed progressively shorter kinetic chain lengths, with number average kinetic chain lengths decreasing from 19.5 for **TFK5** to 6.6 for **TFK15** and on to 4.1 for **TFK25**. The kinetic chain length for **TFK0** could not be accurately determined from this simulation, as the assumption of fast initiation and slow termination does not hold for an uncontrolled FRP system as **TFK0**. However, previous literature[42,43] has provided experimental insight on similar systems which suggest the kinetic chain length for **TFK0** is at least an order of magnitude higher. These results suggest that, while **TFK0** resin (and to a certain degree, **TFK5** resin) can be envisioned as long polyacrylate chains being crosslinked by crosslinkers, in **TFK15** and **TFK25** resins the polyacrylate chains are so short (with an average DP of 3 for **TFK15** and 2 for **TFK25**) that they bear more resemblance to a network formed by condensation polymerization. In a typical photopolymer resin with a high loading of crosslinkers compared to monomers, stress concentrate on the vinyl chains due to the large number of crosslinkers attached to them, but they cannot provide much elasticity due to the close proximity of crosslinkers along the chain. The addition of TFKs disperses these vinyl chains into smaller fragments and allows them to move away from each other under stress, allowing stress to be distributed more evenly, which explains the improved toughness of the TFK resins.

2.2.6 Accelerated degradation of TFK resins

A major challenge faced by acrylic-based photopolymer resins is that, as they are thermosets, it is difficult to process or otherwise degrade them at the end of their life cycles. While in theory the ester bonds in acrylic resins are labile to solvolysis by a variety of nucleophilic solvents, the typical high crosslinking density and low swellability of the resins disfavor solvent ingress. This limits the concentration of solvent molecules inside the resin, thus disfavoring cleavage. In addition, as the vinyl chains themselves are not susceptible to solvolysis, after cleavage they become high molecular weight polyacrylate fragments which are slow to diffuse into solution, further hindering the degradation process. We wondered if the shorter kinetic chains in TFK resins would facilitate faster degradation, as they result in smaller fragments post-cleavage and may clear faster. Moreover, the presence of TTC groups adds additional cleavable points that could facilitate further network swelling.

5mm x 3mm x 2mm pellets of **TFK0** and **TFK25** were cast and cured under previously described conditions. The samples were subsequently immersed in a range of solvent mixtures as presented in **Table 2-5** and heated to 60°C. Gratifyingly, **TFK25** pellets could be completely dissolved to soluble products by a 1:1 mixture of a nucleophilic amine (such as piperidine and *n*-butylamine) and a nucleophilic solvent (such as methanol) over 2-3 days, while **TFK0** pellets remained intact. **TFK25** samples remain intact in 100% methanol under the same conditions. **TFK25** samples immersed in 1:1 mixtures of n-butylamine and non-nucleophilic solvents (such as DMF and chloroform) turn colorless and swell, but do not dissolve.

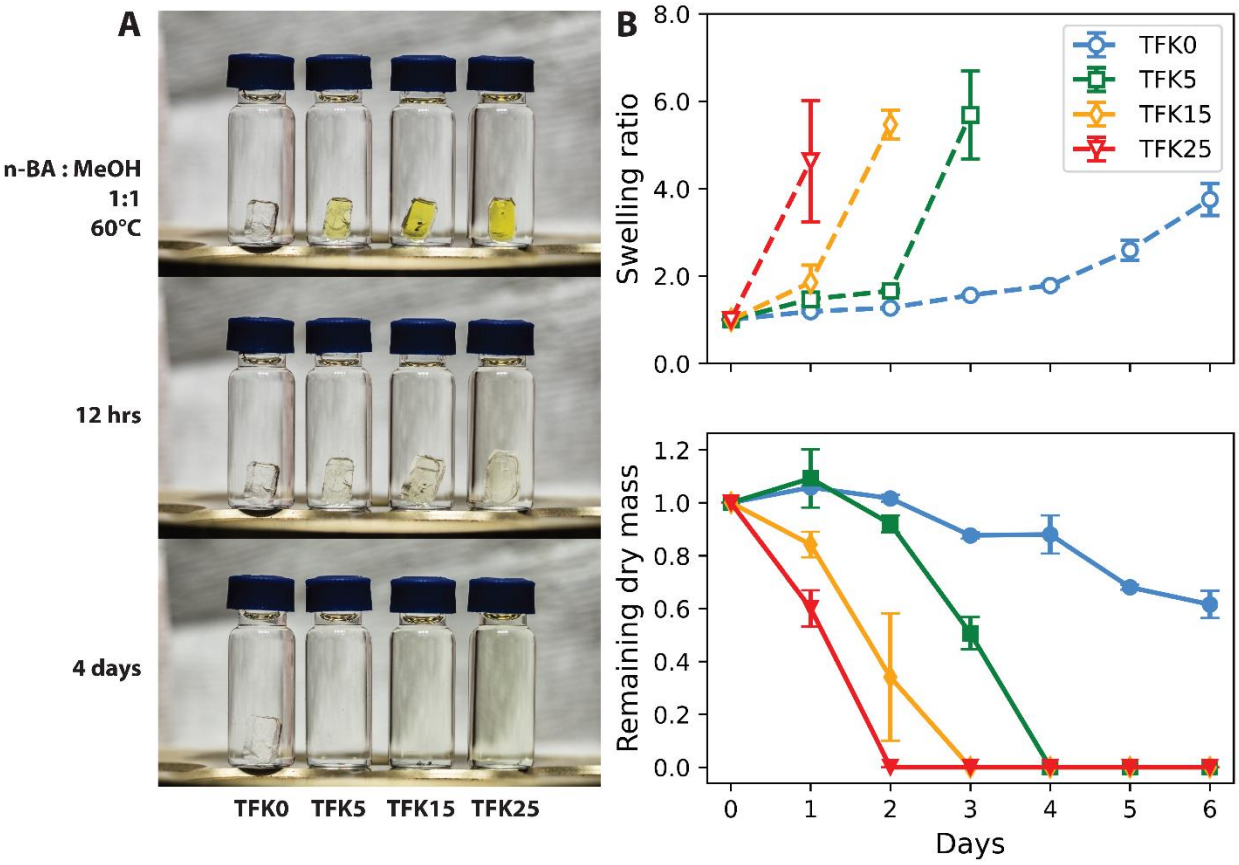

Figure 2-7 Accelerated degradation of TFK resins in the presence of an amine. A) Resin pellets cured with TFK resins are immersed in a 1:1 mixture of *n*-butylamine and heated to 60°C and observed the course of 4 days. B) Weight loss and swelling ratio of TFK resins during degradation.

Further degradation studies were carried out with pellets of **TFK0**, **TFK5**, **TFK15** and **TFK25** resins. The pellets were initially weighed dry and then submerged in a 1:1 mixture of *n*-butylamine and methanol and heated to 60°C. One group of samples was taken out after each day, removed from the solvent, rinsed 3 times with acetone, and weighed to obtain the wet mass. The samples were then dried under vacuum until no change in weight was observed, at which point the dry mass

was recorded. Swelling ratio is defined as the ratio between the wet and dry masses. Cleavage of the trithiocarbonate occurs relatively fast (over 12 hours of immersion) as evidenced by the disappearance of the yellow color, and the resin pellet is swollen into a gel. Resins with higher TFK concentration swell faster. Degradation takes place over the next few days until the gel collapses and eventually disappears. **TFK0** displays some swelling and weight loss but remains mostly intact over the time period of observation.

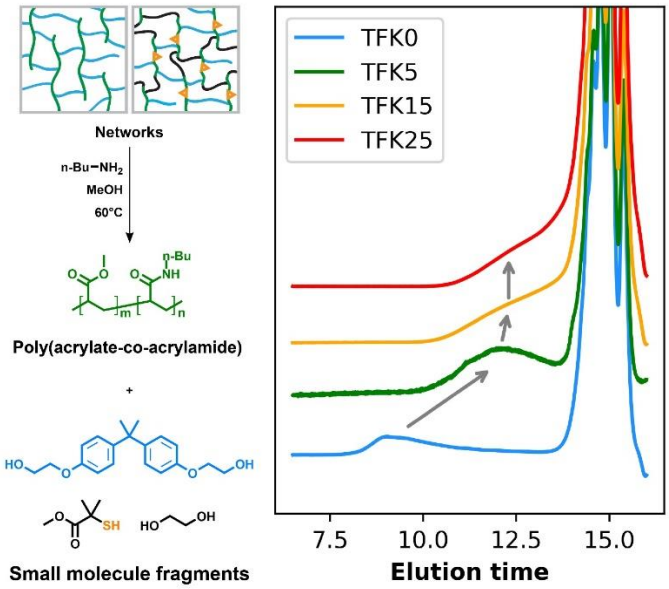

Figure 2-8 GPC traces of degradation residues. Scheme on the left depict proposed structures of polymeric and small molecule degradation products. Figure on the right is the GPC trace of the soluble products formed by the degradation of TFK resins. Gray arrow shows the shift of the polymeric peak corresponding to the decreasing kinetic chain length.

As TTCs are labile to cleavage by aminolysis, and the acrylic crosslinkers are labile to cleavage by alcoholysis, we hypothesized that, after complete cleavage of the resin, the only polymeric residues that remain would be the vinyl chains formed during photopolymerization. Subjecting the soluble residues of the degradation studies to GPC analysis (**Figure 2-8**), **TFK0** did not completely

degrade so the supernatant was used), we were able to observe a polymeric peak in all groups, assumed to be the undegradable acrylates. Consistent with our simulation studies, the molecular weight of this polymer peak decreases with increasing TFK incorporation, suggesting shorter kinetic chains. In **TFK0**, its molecular weight was ~30kDa, consistent with previous studies in similar systems. In **TFK5** the molecular weight was ~3kDa, on the same order of magnitude as suggested by our simulation. To our knowledge, this is the first report of a direct observation of the modulation of kinetic chain length by CTAs in a photopolymer network.

While the shorter kinetic chains in TFK resins are likely to have played a role in their faster degradation, the observation that both an amine and an alcohol need to be present for the accelerated degradation to occur, and the fast cleavage of TTCs throughout the resins suggest that the aminolysis of TTC plays an important role in accelerating degradation. While the low concentration of solvent molecules within the network is not sufficient for the solvolysis of acrylates to take place at any significant rate, the irreversible nature of TTC aminolysis means that they can be cleaved much faster. The cleavage of TTC lowers the crosslinking density of the network and allows it to swell, increasing the concentration of solvent molecules accessible to the ester bonds, facilitating their cleavage. This further swells the resin and the degradation proceeds at an accelerated rate until the entire resin is consumed. While TFK accelerates degradation by facilitating solvent ingress in the presence of an amine, the specificity of this reaction means that resistance to solvents under normal conditions is not compromised, as evidenced by the fact that accelerated degradation is not observed in pure solvents.

2.3 Conclusion

In conclusion, a crosslinker bearing a CTA or "transferinker" (TFK) has been synthesized and its effect in photopolymer resins was investigated through simulation and experiment. Simulation suggests that TFKs have a positive effect on the mechanical properties of the resin by decreasing the amount of dangling chains and preventing the formation of long vinyl chains. This agrees with experiments which show that the introduction of TFKs can increase the toughness of the cured resin by a significant margin at the cost of very little loss in modulus and ultimate tensile strength. Such improvement in mechanical properties cannot be replicated by adding the same amount of

unfunctionalized CTAs. In fact, the addition of unfunctionalized CTAs drastically reduce the modulus of the material, possibly as a result of increased amount of dangling chain ends and the dilution effect of the CTAs themselves. We also demonstrated that TFKs can be used as a drop-in additive to modify the property of off-the-shelf acrylic formulations. In general, building CTAs into crosslinkers could be a translatable strategy towards the introduction of CTAs into photopolymer resins while avoiding significant detriment to mechanical properties. In addition, the introduction of TTC-based TFKs also has the effect of accelerating the degradation of the cured resin under specific conditions, by means of an altered network architecture that leaves lower molecular weight fragments and the fast degradation of TTC. We believe this strategy is not limited to TTC; the incorporation of fast-cleaving moieties could a represent a general approach for accelerating degradation in densely crosslinked polymer network systems in which degradation is limited by solvent diffusion.

2.4 Experimental Section

2.4.1 General

Unless otherwise specified, all reagents are purchased from Sigma-Aldrich and used as received. 2-Hydroxyethyl acrylate is purchased from TCI and used as received. ^{1}H NMR spectra were recorded on Bruker Avance DRX 400 MHz NMR spectrometers at 22 °C. Signals are reported in δ units, parts per million (ppm), and were measured relative to residual solvent peak ($CDCl_3$: 7.26 ppm). Deuterated chloroform was purchased from Cambridge Isotope Laboratories. S,S"-bis(α, α "-dimethyl- α"-acetic acid)-trithiocarbonate (BDMAT) was synthesized following a previously described procedure.[44]

2.4.2 Synthesis of Di(2-(acryloyloxy) ethyl) 2,2'-(thiocarbonylbis(sulfanediyl))bis(2-methylpropanoate) (TFKDA)

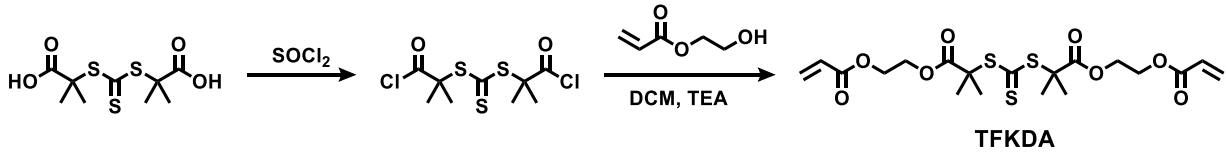

Figure 2-9 Synthesis of model transferinker **TFKDA**

A 250 mL round bottom flask equipped with a reflux condenser and magnetic stirring is charged with 10 g S,S"-bis (α,α"-dimethyl-a"-acetic acid)-trithiocarbonate (BDMAT, 35.4 mmol, 1 eq) and 50 mL $SOCl_2$ and heated to 60°C for 3 hrs. Excess $SOCl_2$ is removed via rotary evaporation (excess 1M NaOH solution is placed in the traps to neutralize the $SOCl_2$ and HCl) to give the acyl chloride as an dark orange solid which is used without further purification. 10.3 g 2-Hydroxyethyl Acrylate (88.5 mmol, 2.5 eq) and 58.5 g Triethylamine (531 mmol, 15 eq) are dissolved in 50 mL DCM in a 500 mL round bottom flask equipped with magnetic stirring and cooled to 0°C with an ice bath. The acyl chloride is dissolved in 50 mL DCM and added in dropwise at 0°C and the reaction is stirred overnight at room temperature. The solvent is removed via rotary evaporation and the residue is dissolved in ethyl acetate, washed 3x with water and extracted with ethyl acetate, dried over anhydrous Na_2SO_4 and purified by column chromatography to give **TFKDA** as an orange oil

(4.7 g, 28%). ^{1}H NMR (400 MHz, Chloroform-d) δ 6.42 (dd, J = 17.3, 1.4 Hz, 2H), 6.12 (dd, J = 17.3, 10.4 Hz, 2H), 5.85 (dd, J = 10.5, 1.4 Hz, 2H), 4.42 – 4.26 (m, 8H), 1.65 (s, 12H).

2.4.3 Synthesis of Di(2-(methoxy) ethyl) 2,2'-(thiocarbonylbis(sulfanediyl)) bis(2-methylpropanoate) (TTCDG)

TTCDG

Figure 2-10 Synthesis of model RAFT agent **TTCDG**

A three-necked round bottomed flask equipped with a stirring bar and a nitrogen inlet is charged with 5 g BDMAT (17.5 mmol, 1 eq) and 16.2 g triphenylphosphine (61.2 mmol, 3.5 eq) and subsequently purged with nitrogen for 30 minutes. 7 g 2-Hydroxyethyl acrylate (62 mmol, 3.5 eq) and anhydrous tetrahydrofuran (100mL) were added to the mixture. The flask is cooled to 0°C with an ice bath. A 40% solution of diethyl azodicarboxylate (28 mL, 62 mmol, 3.5 eq) in toluene was added dropwise. The solution was stirred at room temperature overnight (16 h) and subsequently at 40 °C for 3 hours. It was then diluted with DCM and washed twice with saturated aqueous NaHCO3 solution, extracted with DCM and dried over anhydrous Na_2SO_4 and purified by column chromatography to give **TTCDG** as an orange oil (3.6g, 50%). ^{1}H NMR (400 MHz, Chloroform-d) δ 4.40 – 4.00 (m, 4H), 3.60 – 3.55 (m, 4H), 3.36 (s, 6H), 1.67 (s, 12H).

2.4.4 FTIR study of conversion

FTIR is performed on a Bruker ALPHA II FTIR Spectrometer. A 1mm thick shim plate with a 5mm diameter hole in the middle is placed over the ATR crystal. The hole is filled with resin to ensure thickness of the resin puck. The FTIR spectrometer is programmed to perform an acquisition every 60s. A 30W 405nm LED array is placed 130mm above the setup and turned on after the first two acquisitions are completed. The relative amount of acrylates in the resin is obtained by comparing the intensity of the vinyl C=C peak at 1635cm^{-1} to the aromatic C=C peak

at 1610cm^{-1}. Assuming conversion to be 0 before irradiation, and the aromatic C=C peak does not change in intensity, conversion at a subsequent time point can be calculated:[45]

$$\alpha(t) = 1 - \frac{\left[\frac{I_{1635}}{I_{1610}}\right]_t}{\left[\frac{I_{1635}}{I_{1610}}\right]_0}$$

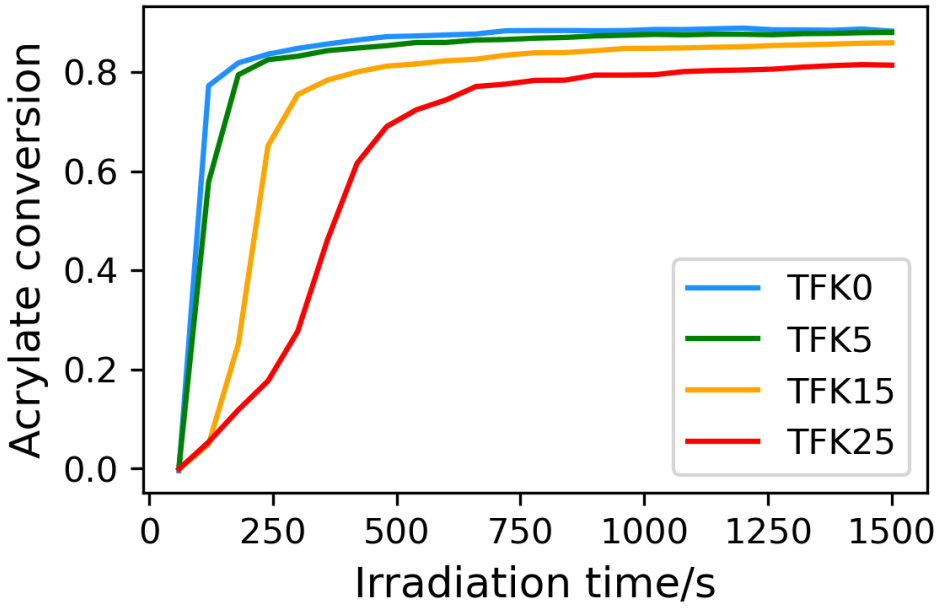

Figure 2-11 Acrylate conversion with irradiation time for TFK resins at 405nm and 1.95mW/cm^2.

The resins are molded into dogbones in a machined PTFE mold. Dimension of the dogbones are shown in **Figure 2-12**. Curing is accomplished by placing the mold under the center of a 30W 405nm LED array. Distance between the top of the mold and the LED array is 130mm. Light intensity of the setup is measured to be 1.95mW/cm^2. The samples are cured for 2h under the LED

lamp, before undergoing post cure in a Formlabs Form Cure enclosure with 405nm irradiation at 60°C for 10 hours.

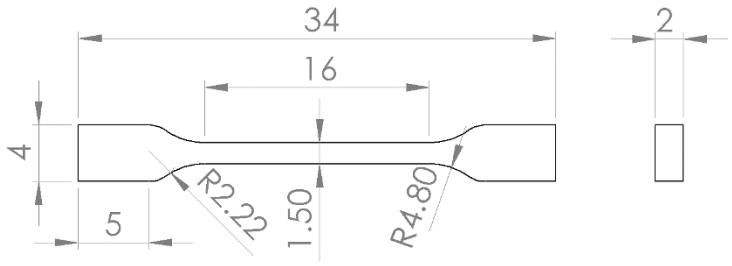

Figure 2-12 Dimension of dogbones used for mechanical testing. Units are in mm.

2.4.5 Mechanical testing

Mechnical testing is performed on an Instron 8848 MicroTester. Dogbone samples were tested to failure at room temperature at a rate of 1mm/min to obtain a stress-strain curve. 25 Samples are prepared and tested for each formulation. Modulus is measured by the slope of the stress-strain curve in the initial linear range. Toughness is measured by integrating stress against strain up to the point of failure. Elongation at break is defined as the strain at point of failure. Maximum tensile strength is defined as the value of stress at yield point.

2.4.6 Dynamic mechanical analysis (DMA)

Dynamic mechanical analysis was carried out in triplicate on a TA Instruments DMA Q800 in tensile mode. A TA Instruments Liquid Nitrogen Purge Cooler (NPC) was used for samples which required low temperature measurements.

DMA samples are 1mm*2.5mm*18mm bars cast in a PTFE mold. Irradiation and post-curing conditions are the same as in dogbones.

Temperature sweeps were conducted from a total range of 0 °C to 220 °C at a heating rate of 3 °C/min (note: sample runs with higher crosslink density were initiated at temperatures up to 50 °C, and sample runs of lower crosslink density were terminated as low as 180 °C). A preload force of 0.01 N and 125.0% force tracking was applied during the measurements. Strain was applied at a frequency of 1 Hz. Unless otherwise indicated, glass transition temperatures were estimated from the average global maxima in tan (δ) peaks across triplicate runs. Molecular weight between crosslinks are calculated with the following formula:

$$M_c = \frac{E_{rubbery}}{3RT}$$

Where $E_{rubbery}$ is taken as the storage modulus at 110°C, well above the glass transition temperature.

The addition of TFK resins does not introduce a significant change in T_g of the network (**Figure 2-13**A), although at higher incorporations TFK still shows some plasticization effect, likely due to the fact that, despite similar in molecular weight, **TFKDA** is more flexible and less bulky as BPAEDA it replaces. This is also reflected in the network homogeneity in **Figure 2-13**B. TFK inherently improves the network homogeneity, however at higher incorporations the dichotomy between the BPAEDA and **TFKDA** chains start to offset the improvement in homogeneity.

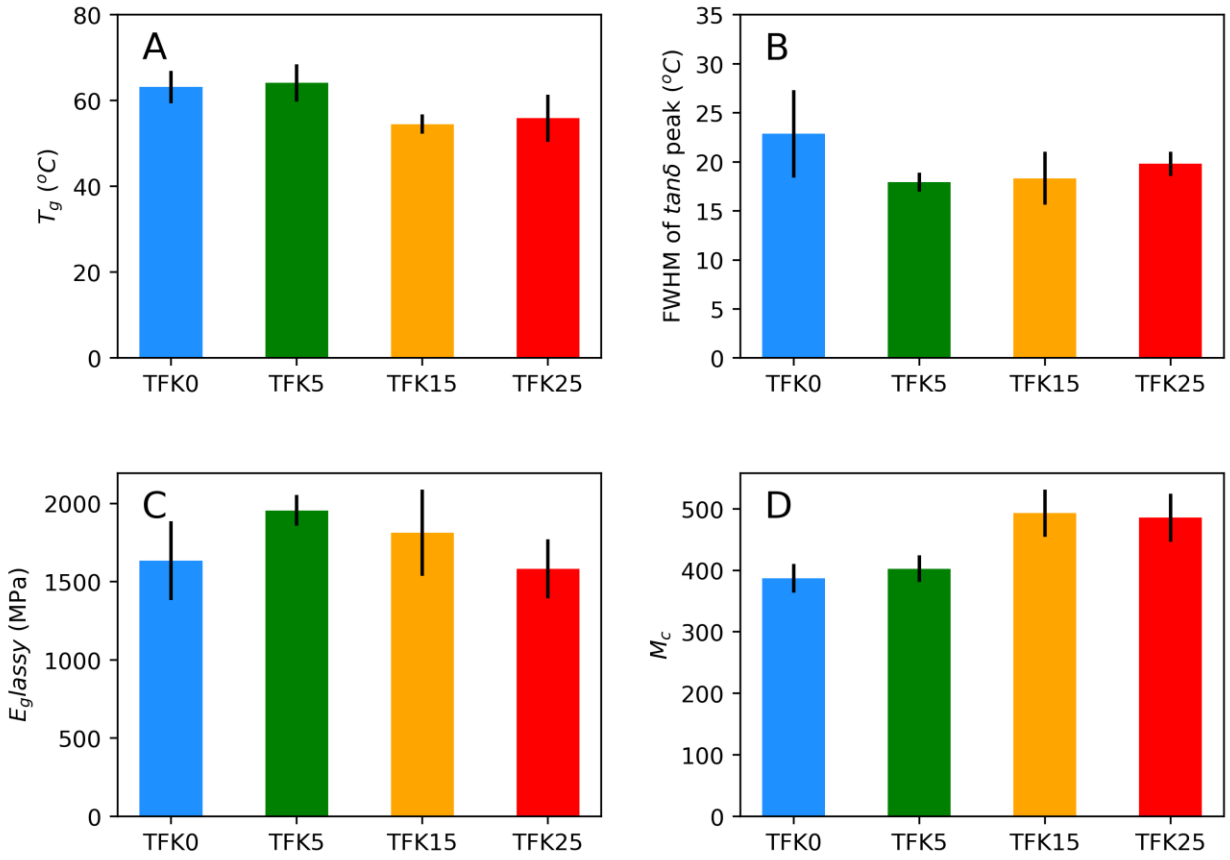

Figure 2-13 Thermomechanical data of TFK resins obtained from DMA. A) Glass transition temperature. B) FWHM of the tanδ peak, reflecting homogeneity of the network. C) Glassy modulus. Storage modulus at 20°C was used. D) Molecular weight between crosslinks.

2.4.7 3D printing

Models for 3D printing are designed in Solidworks 2017, exported as .stl files and sliced with Chitubox 1.6.5 software. 3D printing is performed on an Elegoo Mars Pro 3D printer. Post cured using a Formlabs Form Cure enclosure. Images are recorded using a Sony A7R II camera with a Tokina AT-X 90mm f2.5 Macro lens.

Printing parameters for resins are as shown in **Table 2-4**:

Table 2-4 Printing parameters for different resins. *a*. The first few layers are generally irradiated for longer time to ensure adhesion to the build plate. *b.* Per manufacturer recommendations.

Resin	Cure time for first 5 layers (s)[a]	Cure time for subsequent layers (s)	Layer height (mm)	Post cure
TFK0	100	40	0.05	60°C 10h at 405nm
TFK5	120	40	0.05	60°C 10h at 405nm
Elegoo Standard White (ESW)	60	8	0.05	40°C 1min at 405nm[b]
ESW with 5% TFKDA	60	18	0.05	40°C 1min at 405nm

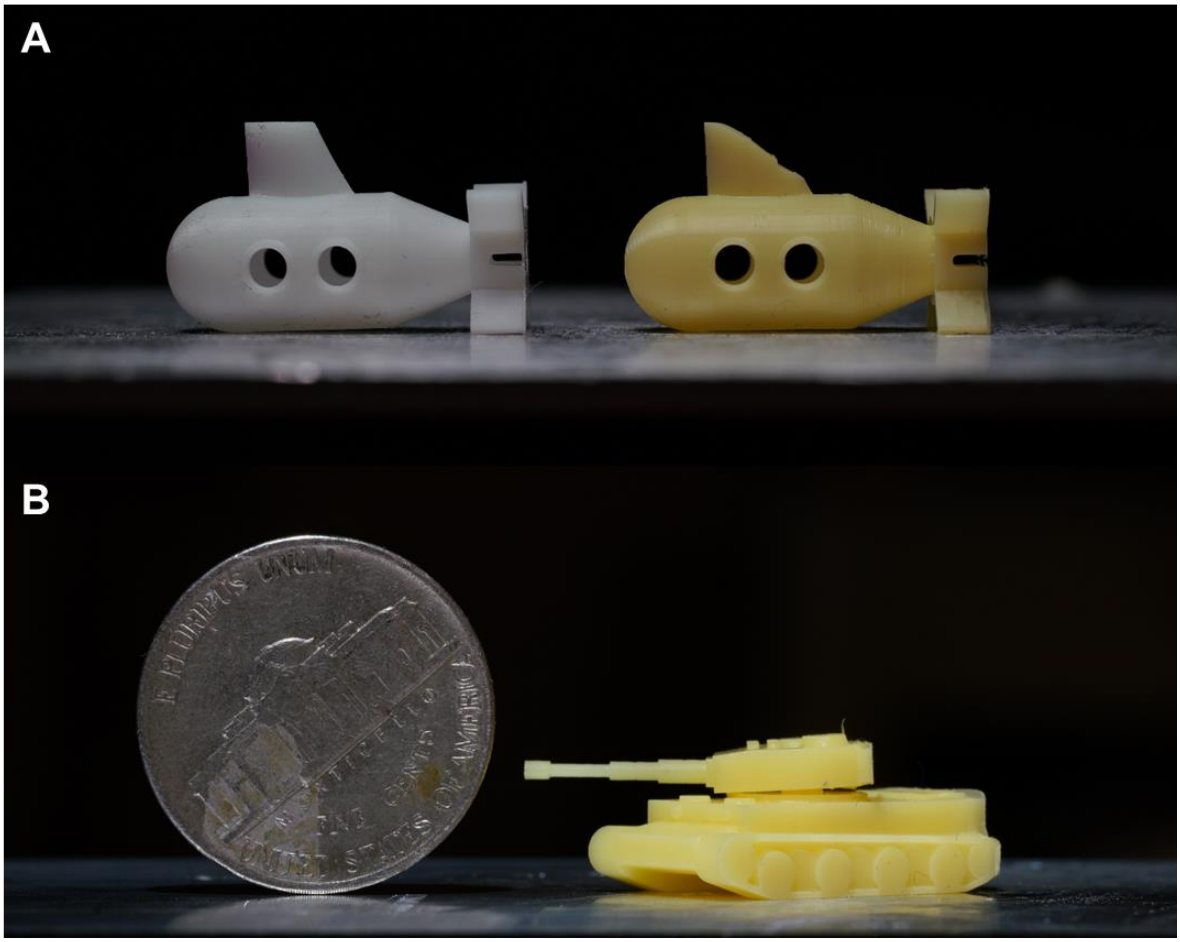

Figure 2-14 Models printed using commercial resin doped with **TFKDA**. A) Submarine model printed with unmodified Elegoo Standard White Resin (left) and resin doped with 5% wt **TFKDA** (right). The doped resin shows a distinctive yellow color. Compared to the unmodified resin, the doped resin is capable of reproducing similar resolution, but requires longer irradiation times and has a steeper overhang threshold (see sail part of submarine). B) A snap-fit toy printed with doped resin. A nickel coin (Diameter 17.91mm) shown for scale. The model is available at https://www.thingiverse.com/thing:90265

2.4.8 Numerical Simulation

The simulation code is written in Python and hosted at:

https://github.com/johnsongroupmit/Network_simulation.

It takes the following parameters, which are listed in the *current_parameters* dictionary:

repeats: The program repeats simulation for a set number of times and average the results.

conversion: The simulation terminates when the desired monomer conversion is reached.

Repeat_unit_length, *crosslinker_length*, *TTC_length*, *TFK_TTC_length*, *TFK_arm_length*: gemoetry of different kinds of species.

monomer_number: Total number of polymerizable functional groups. This includes functional groups contained in crosslinkers. For example, in a system of 2000 monofunctional monomers and 4000 difunctional crosslinkers, the monomer_number will be 10000.

crosslinker_number: Number of difunctional crosslinkers.

TTC_number: Number of trithiocarbonate objects without reactive end groups.

TFK_number: Number of transferinker objects with reactive end groups.

initiator_number: number of initiators

k_transfer_to_ttc and *k_transfer_to_TFK*: Chain transfer constant of the AFCT agent. For tritiocarbonates in acrylic systems, the number is set as 220. In practice, setting these at any value higher than 20 yields very similar results. The larger the values are, the slower the simulation is.

r1 and *r2*: Reactivity ratios as defined in the Mayo-Lewis reaction. They are not used for the scope of this paper and set as 1 at all times. All monomers are initiated with attribute *kind* = 1, meaning they are M1 in the Mayo-Lewis equation. If one wishes to change a certain kind of molecule M2, do so at the end of the definition of *initiation()* function. An example is given in the code comments.

As an output, the program prints the number and weight average molecular weight between crosslinks, the total number of elastic segments, and the total molecular weight contributing to elasticity. It also plots a histogram of elastic segment lengths and exports the data to an Excel file.

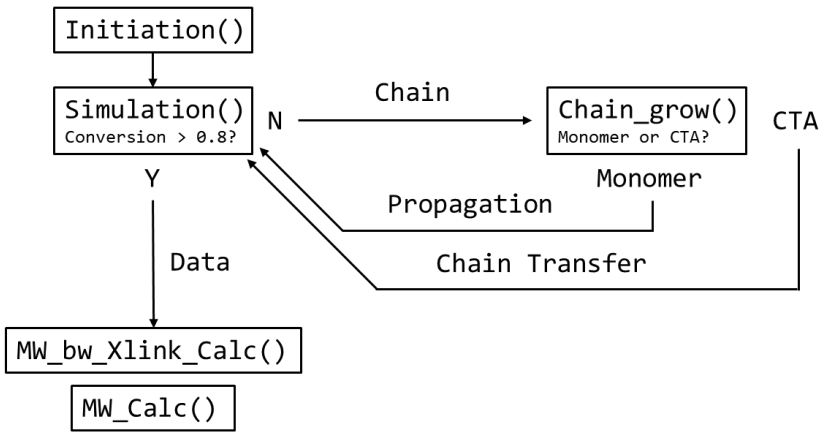

Figure 2-15 Flowchart depicting the relationship between important functions in the simulation program

2.4.8.1 Algorithm overview

Figure 2-15 shows an overview of the algorithm. The process shown is repeated for a set number of times and the results are aggregated to minimize statistical fluctuation.

Initiation(): This function runs at the start of each simulation. It generates monomer, crosslinker, TTC, and TFK objects. Next it allocates monomers to crosslinkers and TFKs by updating the "*parent*" attribute of a monomer and the "*monomer1*" or "*monomer2*" attribute of the parent object. Chains are created next. One active chain is created for each initiator, with the initiator as the "*head*" attribute of the chain. Two inactive chains are created for each TFK or TTC and associations are made accordingly by updating the corresponding attributes in both objects.

Simulation(): The *simulation()* function manages the propagation process until a set conversion is reached. It creates a combined list of monomers, TTCs and TFKs called "*molecule_list*" which represent all the species an active chain end can possibly react with. It picks an active chain at random and passes it on to the *chain_grow()* function. It will continue picking active chains until conversion reaches the set value at which point it exits and passes all the data to the *Mw_btw_Xlink_Calc()* and *MW_calculator()* function.

Chain_grow(): The *chain_grow()* funtion determines the fate of a chain in a reaction step. first it loops through all the members of the *molecule_list* and creates a probability map of the chain end reacting with each member of the *molecule_list*, depending on the identity of the member and of the chain end. Typically, a monomer would be assigned 1 and a TFK or TTC would be assigned their chain transfer constant. Then it performs a weighted random pick from the *molecule_list* based on the probability map. If a monomer is picked, it would be appended to the chain, marked as reacted, and dropped from the *molecule_list*. If a TFK is picked, the current chain is deactivated and appended to the TFK, and a random chain on the TFK is activated. TTCs are treated in the same way.

The process of generating a weight map for each cycle of the chain growth is computationally time consuming, but it allows new species with different reactivities to be easily modelled in the future. A *chain_grow_alt()* is provided which runs faster but is limited to a monomer-TFK system.

Mw_btw_Xlink_Calc(): This function calculates the molecular weight between crosslinks. First, it identifies crosslinking points. If both ends of a crosslinker are reacted, they are both crosslinking points. For chains that are originally part of a TFK, which means they have a monomer in the beginning, the monomer is a crosslinking point if it is reacted. Then, it loops through all the chains and adds the length all the monomers and TFK side chains between two adjacent crosslinking points on a chain to obtain the lengths of elastic segments along the vinyl backbones (which are what the chain objects represent). Unreacted or partially reacted crosslinkers are not counted, nor are monomers at the end of a chain that is not attached to anything. Finally, the lengths of crosslinkers, TTCs and TFKs are considered to give the final distribution of elastic segments. The number average and weight average length of these segments can also be calculated.

MW_calculator(): This function calculates the length of each chain to give the distribution of kinetic chain lengths.

2.4.9 Degradation studies

6mm*4mm*2mm pellets of resin are cured as previously described and placed in 2 mL autosampler vials. The vials are filled with a 1:1 mixture of *n*-butylamine and Methanol and placed on a hotplate heated to 60°C. The degradation process is optically monitored using an Olympus E-M1 camera with a Canon FD 50mm f3.5 SSC Macro lens.

For gravimetric studies, resin pellets are cured as previously described and weighed. Degradation samples are prepared in triplicates for each time point. At each time point, solvent is removed by decantation (or filtering if the sample is broken into small pieces) and the insoluble content is weighed to obtain the wet mass. The insoluble content is then placed under vacuum at 40°C and weighed daily until no further change in mass is observed. The final mass of the dried sample is

the dry mass. Weight loss is obtained by comparing the remaining dry mass with the original mass of the sample. Swelling ratio is defined as the ratio between the wet mass and dry mass.

For gel permeation chromatography (GPC) measurements, the degradation residue is filtered to remove any insoluble content. Solvent is removed *in vacuo* and the remaining residue is dissolved in $CHCl_3$ and filtered through a 0.2μm syringe filter to prepare a GPC sample.

Table 2-5 Screening of degradation conditions. Sample pellets are immersed in solvent mixtures, heated to 60°C and observed over the course of 7 days. Abbreviations used: MeOH (methanol); *n*-BuA (*n*-butylamine); EtOH (ethanol); DMF (N, N'-dimethylformamide); MeCN (acetonitrile); $CHCl_3$ (chloroform); TEA (triethylamine). *a.* Unless otherwise specified, solvent mixtures are 1:1. *b.* 100% *n*-Butylamine. *c.* "Degraded" means no insoluble mass is observable.

Solvent Mixture[a]	**Resin Formulation**	
	TFK0	**TFK25**
MeOH / n-BuA	Unchanged	Degraded in 4 days[c]
MeOH / Piperidine	Unchanged	Degraded in 4 days[c]
EtOH/ n-BuA	Unchanged	Degraded in 4 days[c]
n-BuA[b]	Unchanged	Degraded in 6 days[c]
MeOH	Unchanged	Unchanged
DMF / n-BuA	Unchanged	Colorless, broken
MeCN / n-BuA	Unchanged	Colorless
$CHCl_3$ / n-BuA	Unchanged	Colorless, broken
TEA / n-BuA	Unchanged	Colorless

2.4.10 Gel Permeation Chromatography (GPC)

GPC measurements were performed on a Tosoh Ecosec HLC-8320 GPC system with three TSKgel Super HZ columns (SuperHZ 4000, SuperHZ 3000, SuperHZ 2500) in tandem at 40°C and a flow rate of 0.6mL/min with Chloroform with 0.75% Ethanol as the mobile phase. Molecular weight determination is performed by calibrating the elution curve in dRI against a calibration curve obtained with Agilent EasiCal PS-2 standards.

2.4.11 Degradation studies of 3D printed samples

Rectangular blocks with printed letters are printed with **TFK0** and **TFK5** resins and submerged in a 1:1 mixture of *n*-butylamine and Methanol and heated to 60°C. Images are recorded using a Sony A7R II camera with a Tokina AT-X 90mm f2.5 Macro lens.

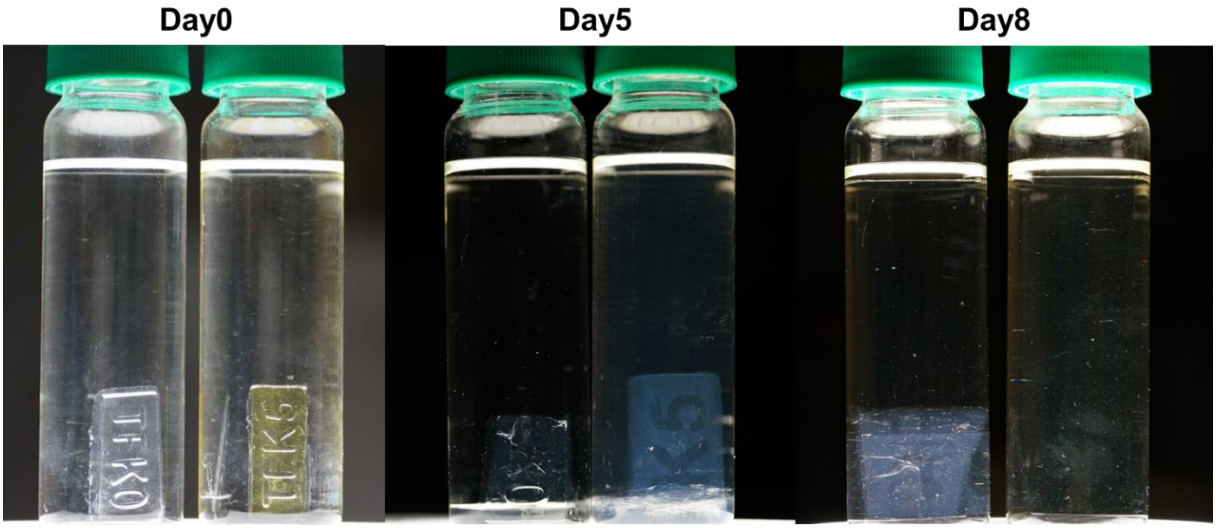

Figure 2-16 Degradation of samples printed with **TFK0** and **TFK5** resins. The **TFK5** sample swells and degrades faster than the **TFK0** sample. The **TFK0** sample fractured on day 2 due to uneven swelling, typical of large 3D printed objects. On day 4 **TFK5** sample is completely degraded, while **TFK0** sample largely remains intact.

2.5 Supplements

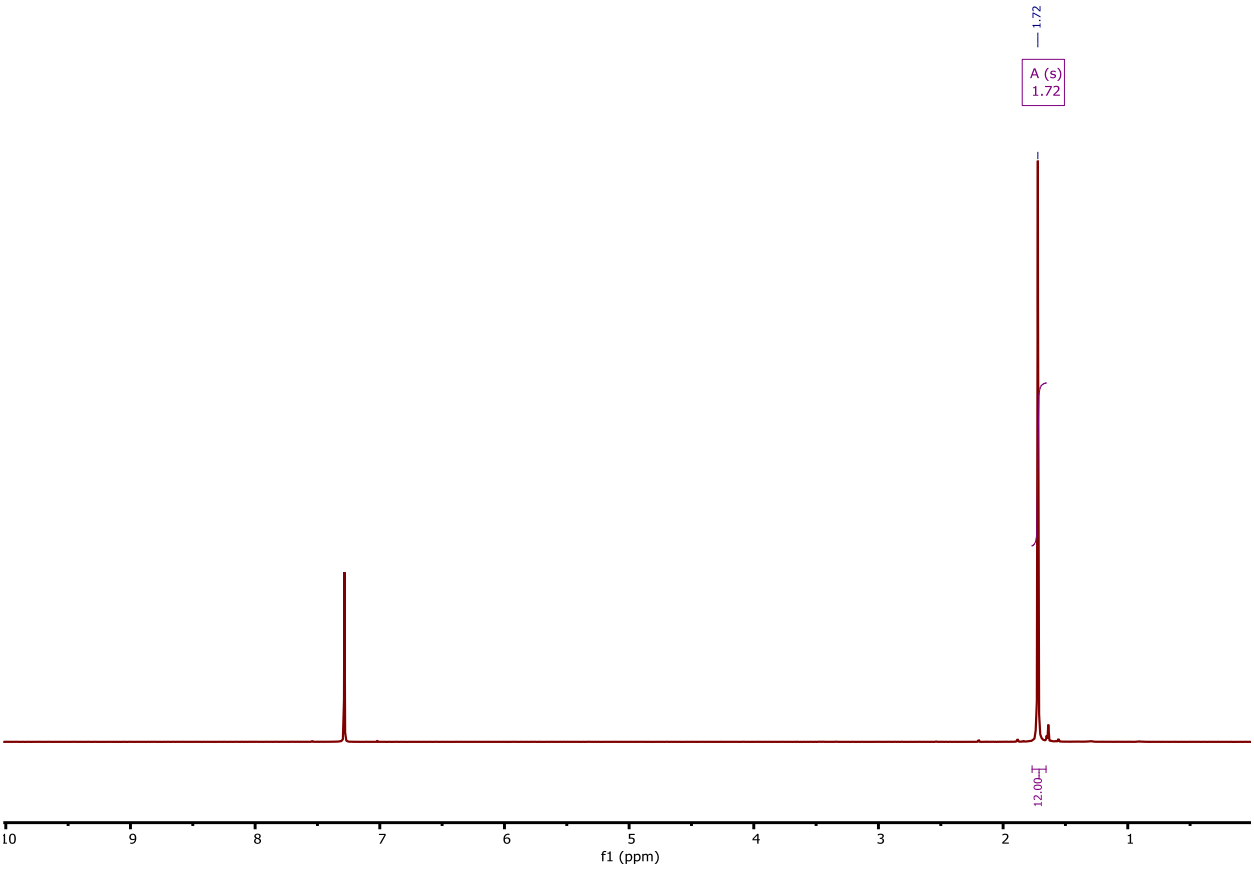

Figure 2-17 ^{1}H-NMR of BDMAT in $CDCl_3$

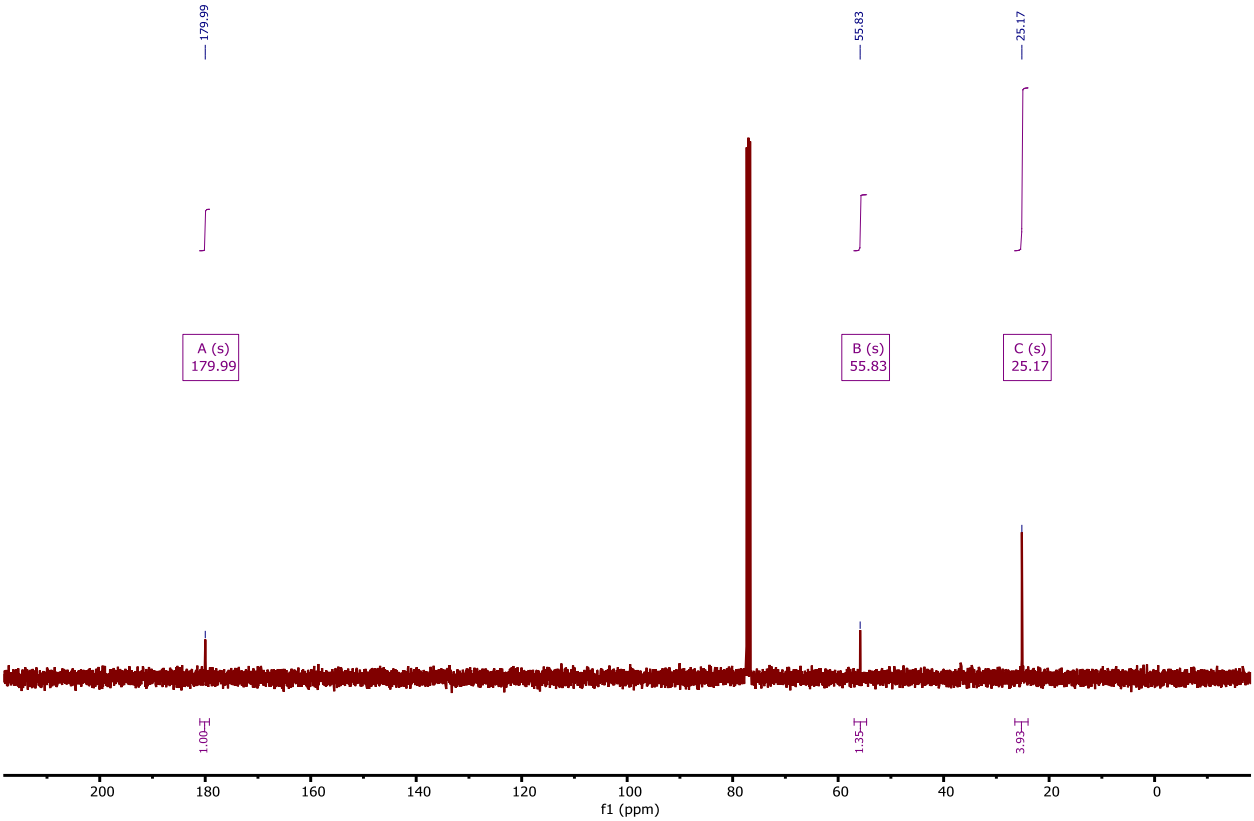

Figure 2-18 ^{13}C-NMR of BDMAT in $CDCl_3$

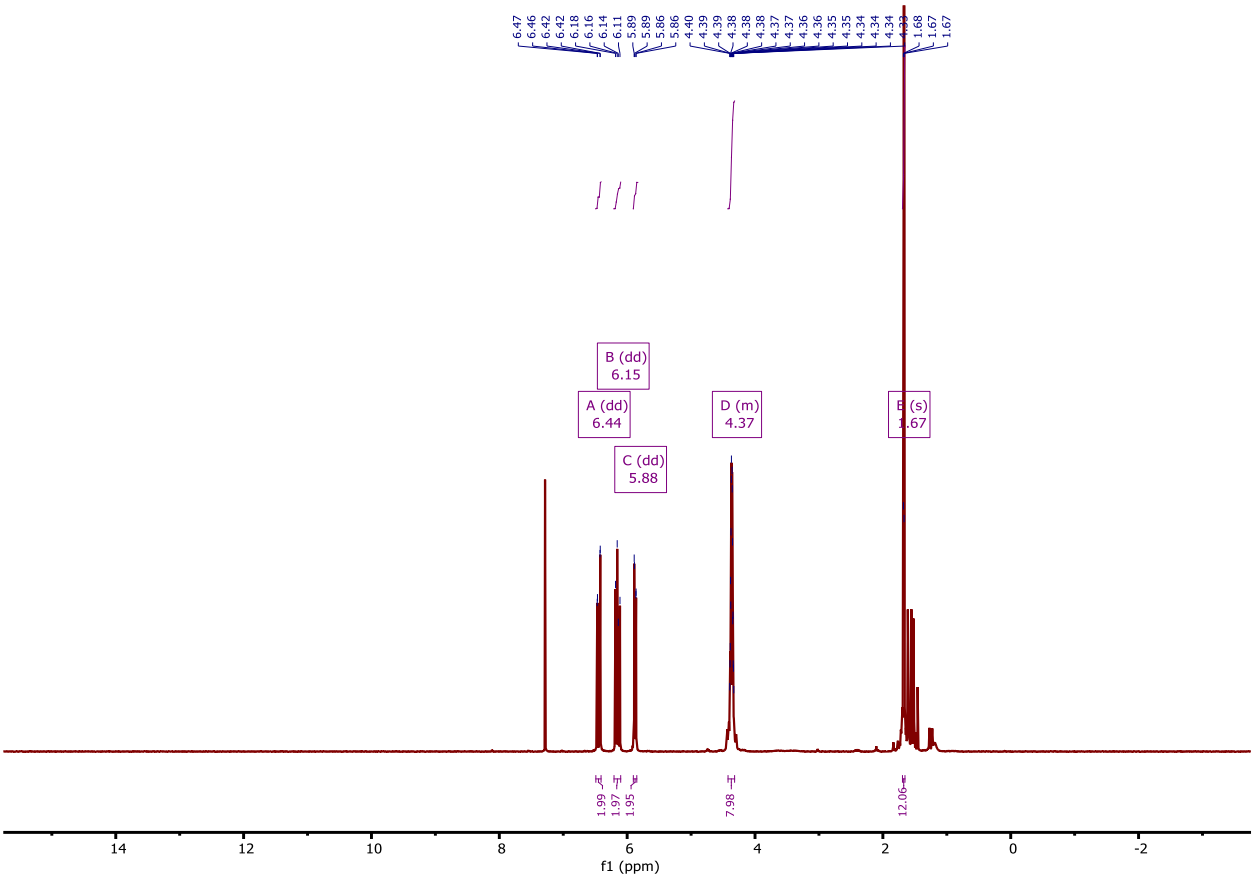

Figure 2-19 ^{1}H-NMR of **TFKDA** in $CDCl_3$

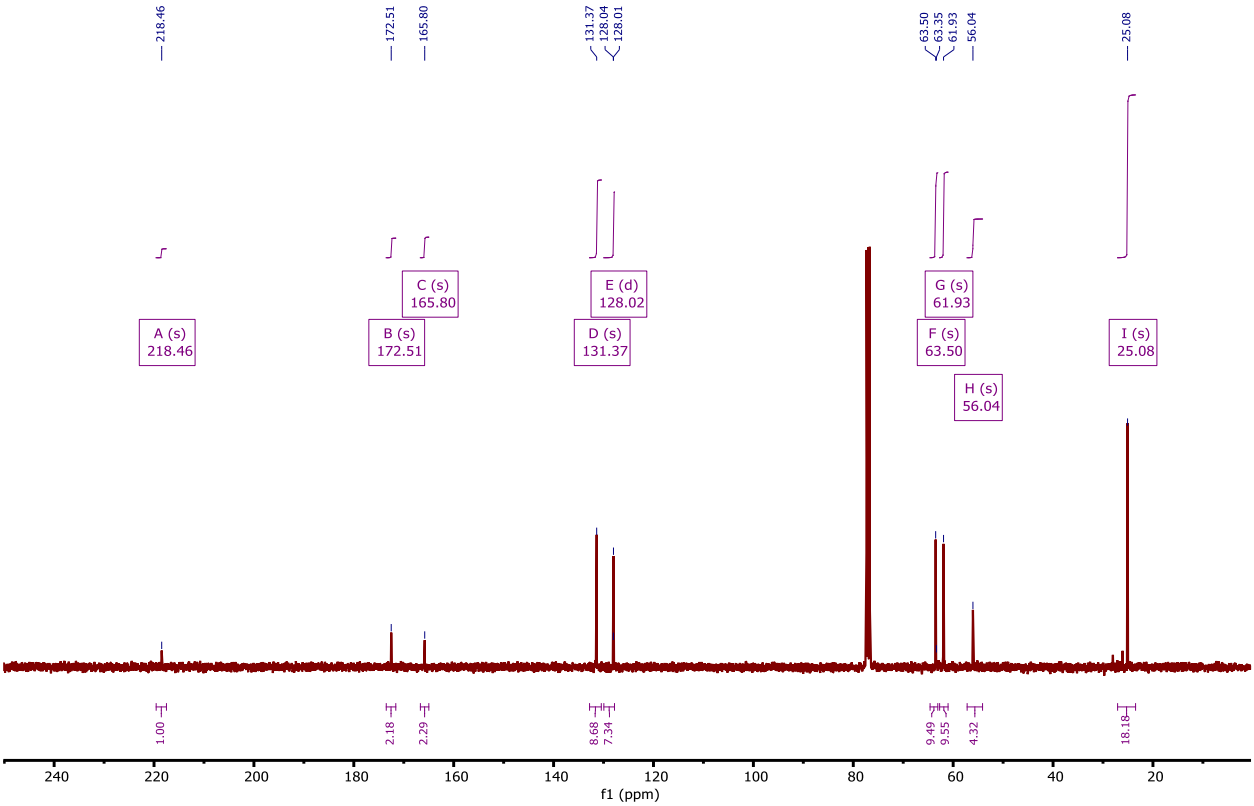

Figure 2-20 ^{13}C-NMR of **TFKDA** in $CDCl_3$

^{1}H NMR (400 MHz, Chloroform-*d*) δ 4.37 – 4.20 (m, 2H), 3.69 – 3.57 (m, 2H), 3.39 (s, 3H), 1.70 (s, 6H).

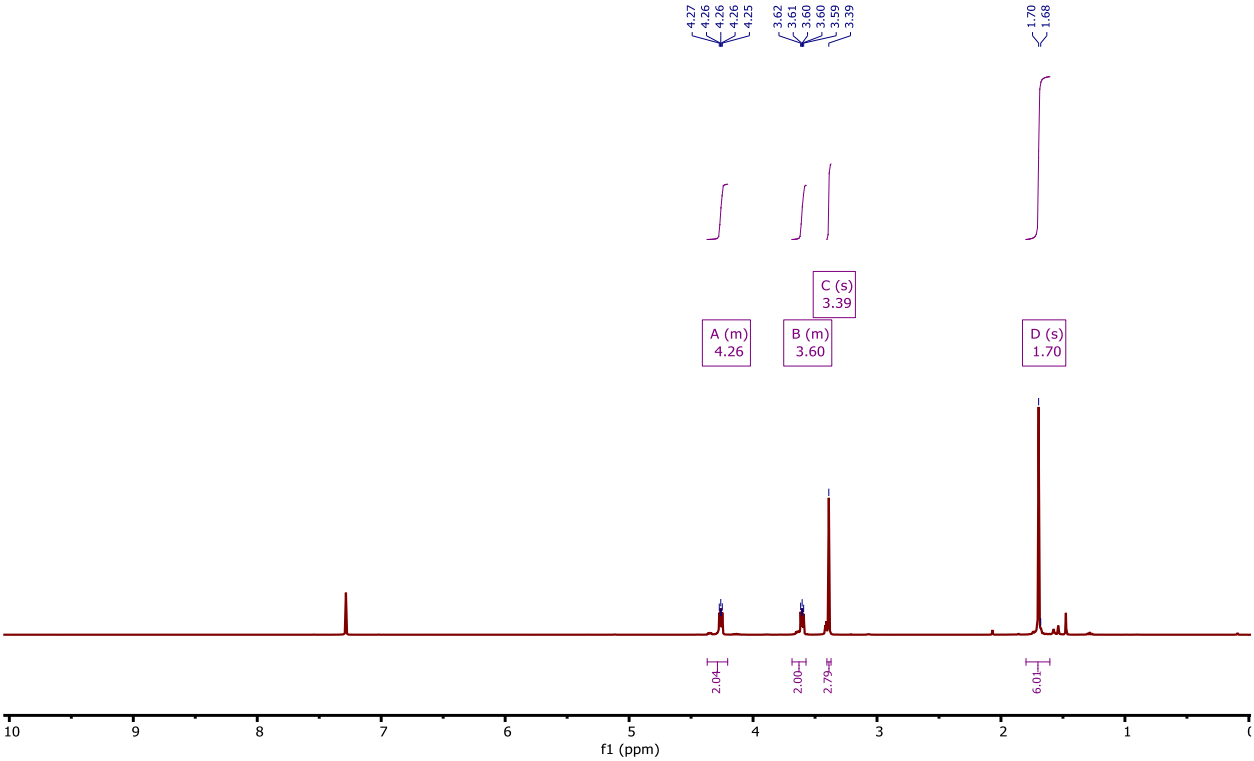

Figure 2-21 ^{1}H-NMR of **TTCDG** in $CDCl_3$

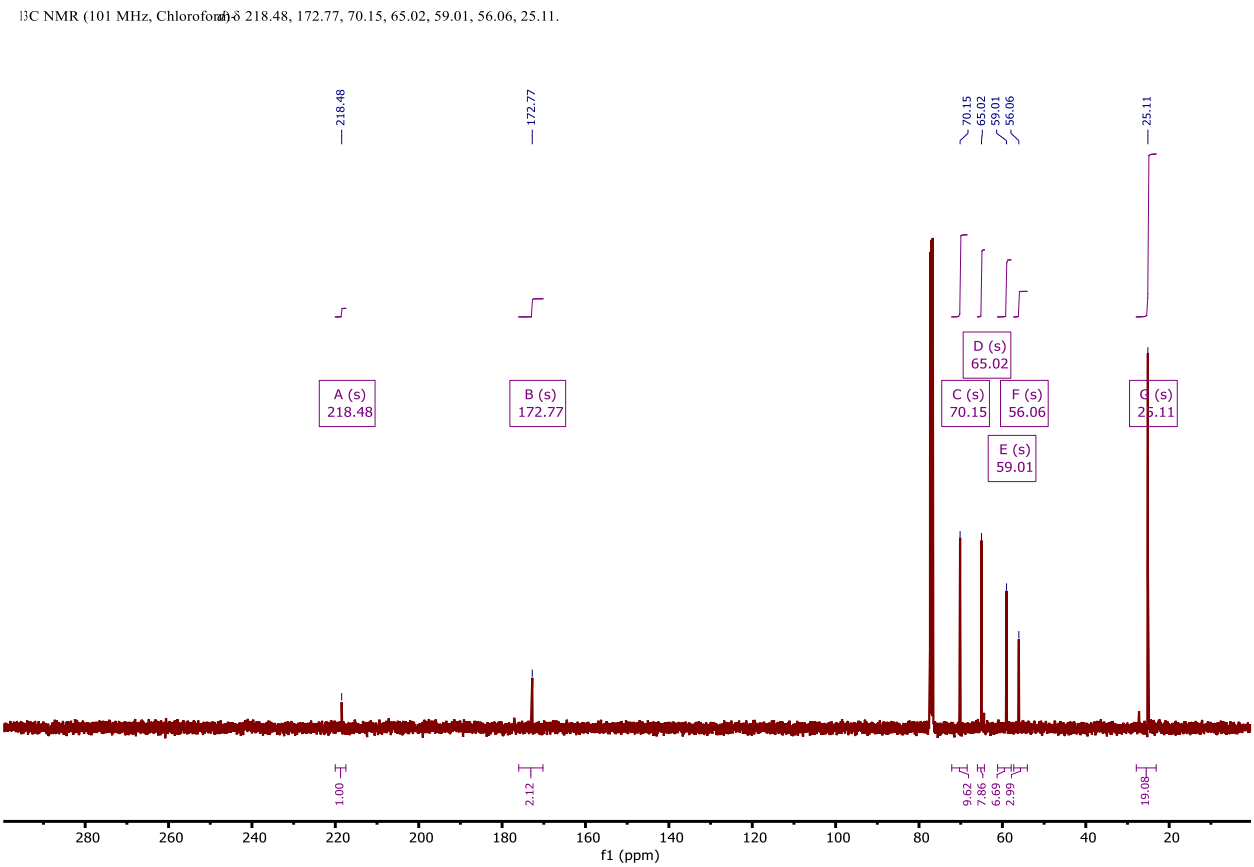

Figure 2-22 ^{13}C-NMR of **TTCDG** in $CDCl_3$

Reference

(1) Bongiovanni, R.; Montefusco, F.; Priola, A.; Macchioni, N.; Lazzeri, S.; Sozzi, L.; Ameduri, B. High Performance UV-Cured Coatings for Wood Protection. *Prog. Org. Coatings* **2002**, *45* (4), 359–363. https://doi.org/10.1016/S0300-9440(02)00119-4.

(2) Farhat, S.; Gilliam, M.; Rabago-Smith, M.; Baran, C.; Walter, N.; Zand, A. Polymer Coatings for Biomedical Applications Using Atmospheric Pressure Plasma. *Surf. Coatings Technol.* **2014**, *241*, 123–129. https://doi.org/10.1016/j.surfcoat.2013.10.077.

(3) Karasu, F.; Croutxé-Barghorn, C.; Allonas, X.; Van Der Ven, L. G. J. Free Radical Photopolymerization Initiated by UV and LED: Towards UV Stabilized, Tack Free Coatings. *J. Polym. Sci. Part A Polym. Chem.* **2014**, *52* (24), 3597–3607. https://doi.org/10.1002/POLA.27427.

(4) Kim, H. K.; Kim, J. G.; Cho, J. D.; Hong, J. W. Optimization and Characterization of UV-Curable Adhesives for Optical Communications by Response Surface Methodology. *Polym. Test.* **2003**, *22* (8), 899–906. https://doi.org/10.1016/S0142-9418(03)00038-2.

(5) Murata, N.; Nakamura, kouzaburo. UV-Curable Adhesives For Optical Communications. *http://dx.doi.org/10.1080/00218469108041012* **2006**, *35* (4), 251–267. https://doi.org/10.1080/00218469108041012.

(6) Malik, J.; Clarson, S. J. A Thermally Reworkable UV Curable Acrylic Adhesive Prototype. *Int. J. Adhes. Adhes.* **2002**, *22* (4), 283–289. https://doi.org/10.1016/S0143-7496(02)00005-2.

(7) Klee, J. E.; Maier, M.; Fik, C. P. Applied Photochemistry in Dental Materials: From Beginnings to State of the Art. In *Dyes and Chromophores in Polymer Science*; John Wiley & Sons, Inc.: Hoboken, NJ, USA, 2015; pp 123–138. https://doi.org/10.1002/9781119006671.ch4.

(8) Dolinski, N. D.; Page, Z. A.; Benjamin Callaway, E.; Eisenreich, F.; Garcia, R. V; Chavez, R.; Bothman, D. P.; Hecht, S.; Zok, F. W.; Hawker, C. J.; Dolinski, N. D.; Callaway, E. B.; Zok, F. W.; Hawker, C. J.; Page, Z. A.; Eisenreich, F.; Garcia, R. V; Chavez, R.; Hecht, S.; Bothman, D. P. Solution Mask Liquid Lithography (SMaLL) for One-Step, Multimaterial 3D Printing. *Adv. Mater.* **2018**, *30* (31), 1800364. https://doi.org/10.1002/ADMA.201800364.

(9) Tumbleston, J. R.; Shirvanyants, D.; Ermoshkin, N.; Janusziewicz, R.; Johnson, A. R.; Kelly, D.; Chen, K.; Pinschmidt, R.; Rolland, J. P.; Ermoshkin, A.; Samulski, E. T.; DeSimone, J. M. Continuous Liquid Interface Production of 3D Objects. *Science* **2015**, *347* (6228), 1349–1352. https://doi.org/10.1126/science.aaa2397.

(10) Zhang, Z.; Corrigan, N.; Bagheri, A.; Jin, J.; Boyer, C. A Versatile 3D and 4D Printing System through Photocontrolled RAFT Polymerization. **2019**, No. 50.

(11) Jung, K.; Corrigan, N.; Ciftci, M.; Xu, J.; Seo, S. E.; Hawker, C. J.; Boyer, C. Designing with Light: Advanced 2D, 3D, and 4D Materials. *Adv. Mater.* **2020**, *32* (18). https://doi.org/10.1002/ADMA.201903850.

(12) Schwartz, J. J.; Boydston, A. J. Multimaterial Actinic Spatial Control 3D and 4D Printing. **2019**, *10* (1). https://doi.org/10.1038/s41467-019-08639-7.

(13) Liska, R.; Schuster, M.; Inführ, R.; Turecek, C.; Fritscher, C.; Seidl, B.; Schmidt, V.; Kuna, L.; Haase, A.; Varga, F.; Lichtenegger, H.; Stampfl, J. Photopolymers for Rapid Prototyping. *J. Coatings Technol. Res.* **2007**, *4* (4), 505–510. https://doi.org/10.1007/S11998-007-9059-3.

(14) Kelly, B. E.; Bhattacharya, I.; Heidari, H.; Shusteff, M.; Spadaccini, C. M.; Taylor, H. K. Volumetric Additive Manufacturing via Tomographic Reconstruction. *Science* **2019**, *363* (6431), 1075–1079.

(15) Munprom, R.; Limtasiri, S. Optimization of Stereolithographic 3D Printing Parameters Using Taguchi Method for Improvement in Mechanical Properties. *Mater. Today Proc.* **2019**, *17*, 1768–1773. https://doi.org/10.1016/j.matpr.2019.06.209.

(16) Yin, H.; Ding, Y.; Zhai, Y.; Tan, W.; Yin, X. Orthogonal Programming of Heterogeneous Micro-Mechano-Environments and Geometries in Three-Dimensional Bio-Stereolithography. *Nat. Commun. 2018 91* **2018**, *9* (1), 1–7. https://doi.org/10.1038/s41467-018-06685-1.

(17) Quan, H.; Zhang, T.; Xu, H.; Luo, S.; Nie, J.; Zhu, X. Photo-Curing 3D Printing Technique and Its Challenges. *Bioact. Mater.* **2020**, *5* (1), 110–115. https://doi.org/10.1016/J.BIOACTMAT.2019.12.003.

(18) Ligon-Auer, S. C.; Schwentenwein, M.; Gorsche, C.; Stampfl, J.; Liska, R. Toughening of Photo-Curable Polymer Networks: A Review. *Polym. Chem.* **2015**, *7* (2), 257–286. https://doi.org/10.1039/C5PY01631B.

(19) Zhang, Z.; Corrigan, N.; Boyer, C. Effect of Thiocarbonylthio Compounds on Visible-Light-Mediated 3D Printing. *Macromolecules* **2021**, *54* (3), 1170–1182. https://doi.org/10.1021/acs.macromol.0c02691.

(20) Lovestead, T. M.; O'Brien, A. K.; Bowman, C. N. Models of Multivinyl Free Radical Photopolymerization Kinetics. *J. Photochem. Photobiol. A Chem.* **2003**, *159* (2), 135–143. https://doi.org/10.1016/S1010-6030(03)00178-3.

(21) Elliott, J. E.; Bowman, C. N. Monomer Functionality and Polymer Network Formation. *Macromolecules* **2001**, *34* (13), 4642–4649. https://doi.org/10.1021/ma010153m.

(22) Gu, Y.; Zhao, J.; Johnson, J. A. Polymer Networks: From Plastics and Gels to Porous Frameworks. *Angew. Chemie Int. Ed.* **2020**, *59* (13), 5022–5049. https://doi.org/10.1002/anie.201902900.

(23) Yu, Q.; Zhu, Y.; Ding, Y.; Zhu, S. Reaction Behavior and Network Development in RAFT Radical Polymerization of Dimethacrylates. *Macromol. Chem. Phys.* **2008**, *209* (5), 551–556. https://doi.org/10.1002/MACP.200700464.

(24) Bobrin, V. A.; Lee, K.; Zhang, J.; Corrigan, N.; Boyer, C.; Bobrin, V. A.; Lee, K.; Corrigan, N.; Boyer, C.; Zhang, J. Nanostructure Control in 3D Printed Materials. *Adv. Mater.* **2021**, 2107643. https://doi.org/10.1002/ADMA.202107643.

(25) Gorsche, C.; Seidler, K.; Knaack, P.; Dorfinger, P.; Koch, T.; Stampfl, J.; Moszner, N.; Liska, R. Rapid Formation of Regulated Methacrylate Networks Yielding Tough Materials for Lithography-Based 3D Printing. *Polym. Chem.* **2016**, *7* (11), 2009–2014. https://doi.org/10.1039/C5PY02009C.

(26) Gorsche, C.; Koch, T.; Moszner, N.; Liska, R. Exploring the Benefits of β-Allyl Sulfones for More Homogeneous Dimethacrylate Photopolymer Networks. *Polym. Chem.* **2015**, *6* (11), 2038–2047. https://doi.org/10.1039/C4PY01582G.

(27) Peer, G.; Eibel, A.; Gorsche, C.; Catel, Y.; Gescheidt, G.; Moszner, N.; Liska, R. Ester-Activated Vinyl Ethers as Chain Transfer Agents in Radical Photopolymerization of Methacrylates. *Macromolecules* **2019**, *52* (7), 2691–2700. https://doi.org/10.1021/acs.macromol.9b00085.

(28) Moad, G.; Chiefari, J.; Chong, Y.; Krstina, J.; Mayadunne, R. T.; Postma, A.; Rizzardo, E.; Thang, S. H. Living Free Radical Polymerization with Reversible Addition-Fragmentation Chain Transfer (the Life of RAFT). *Polym. Int.* **2000**, *49* (9), 993–1001. https://doi.org/10.1002/1097-0126.

(29) Moad, G. Trithiocarbonates in RAFT Polymerization . *RAFT Polym.* **2021**, 359–492. https://doi.org/10.1002/9783527821358.CH9.

(30) Moad, G.; Rizzardo, E.; Thang, S. H. Radical Addition–Fragmentation Chemistry in Polymer Synthesis. *Polymer* **2008**, *49* (5), 1079–1131. https://doi.org/10.1016/J.POLYMER.2007.11.020.

(31) Brown, T. E.; Carberry, B. J.; Worrell, B. T.; Dudaryeva, O. Y.; McBride, M. K.; Bowman, C. N.; Anseth, K. S. Photopolymerized Dynamic Hydrogels with Tunable Viscoelastic Properties through Thioester Exchange. *Biomaterials* **2018**, *178*, 496–503. https://doi.org/10.1016/j.biomaterials.2018.03.060.

(32) Fenoli, C. R.; Wydra, J. W.; Bowman, C. N. Controllable Reversible Addition–Fragmentation Termination Monomers for Advances in Photochemically Controlled Covalent Adaptable Networks. *Macromolecules* **2014**, *47* (3), 907–915. https://doi.org/10.1021/MA402548E.

(33) Kloxin, C. J.; Bowman, C. N. Covalent Adaptable Networks: Smart, Reconfigurable and Responsive Network Systems. *Chem. Soc. Rev.* **2013**, *42* (17), 7161–7173. https://doi.org/10.1039/C3CS60046G.

(34) Zhang, Z.; Corrigan, N.; Boyer, C. A Photoinduced Dual-Wavelength Approach for 3D Printing and Self-Healing of Thermosetting Materials. *Angew. Chemie Int. Ed.* **2021**. https://doi.org/10.1002/ANIE.202114111.

(35) Lee, K.; Corrigan, N.; Boyer, C. Rapid High-Resolution 3D Printing and Surface Functionalization via Type I Photoinitiated RAFT Polymerization. *Angew. Chemie Int. Ed.* **2021**, *60* (16), 8839–8850. https://doi.org/10.1002/ANIE.202016523.

(36) Bagheri, A.; Engel, K. E.; Bainbridge, C. W. A.; Xu, J.; Boyer, C.; Jin, J. 3D Printing of Polymeric Materials Based on Photo-RAFT Polymerization. *Polym. Chem.* **2020**, *11* (3), 641–647.

(37) Fenoli, C. R.; Bowman, C. N. Synthesis of Novel Trithiocarbonate and Allyl Sulfide Containing Monomers. *Polym. Chem.* **2013**, *5* (1), 62–68. https://doi.org/10.1039/C3PY00709J.

(38) Park, H. Y.; Kloxin, C. J.; Scott, T. F.; Bowman, C. N. Covalent Adaptable Networks as Dental Restorative Resins: Stress Relaxation by Addition–Fragmentation Chain Transfer in Allyl Sulfide-Containing Resins. *Dent. Mater.* **2010**, *26* (10), 1010–1016. https://doi.org/10.1016/j.dental.2010.06.007.

(39) Anastasio, R.; Cardinaels, R.; Peters, G. W. M.; van Breemen, L. C. A. Structure–Mechanical Property Relationships in Acrylate Networks. *J. Appl. Polym. Sci.* **2020**, *137* (13), 48498. https://doi.org/10.1002/APP.48498.

(40) Smith, A. A. A.; Hall, A.; Wu, V.; Xu, T. Practical Prediction of Heteropolymer Composition and Drift. *ACS Macro Lett.* **2019**, *8* (1), 36–40. https://doi.org/10.1021/acsmacrolett.8b00813.

(41) Rudin, A.; Choi, P. The Elements of Polymer Science and Engineering. *Elem. Polym. Sci. Eng.* **2013**. https://doi.org/10.1016/C2009-1-64286-6.

(42) Burdick, J. A.; Lovestead, T. M.; Anseth, K. S. Kinetic Chain Lengths in Highly Cross-Linked Networks Formed by the Photoinitiated Polymerization of Divinyl Monomers: A Gel Permeation Chromatography Investigation. *Biomacromolecules* **2002**, *4* (1), 149–156. https://doi.org/10.1021/BM025677O.

(43) Anseth, K. S.; Wang, C. M.; Bowman, C. N. Reaction Behaviour and Kinetic Constants for Photopolymerizations of Multi(Meth)Acrylate Monomers. *Polymer* **1994**, *35* (15), 3243–3250. https://doi.org/10.1016/0032-3861(94)90129-5.

(44) Lai, J. T.; Filla, D.; Shea, R. Functional Polymers from Novel Carboxyl-Terminated Trithiocarbonates as Highly Efficient RAFT Agents. *Macromolecules* **2002**, *35* (18), 6754–6756. https://doi.org/10.1021/MA020362M.

(45) Herrera-Gonzaíez, A. M.; Caldera-Villalobos, M.; Pe, A. A.; Cuevas-Sua, C. E.; Abraham Gonzaíez-Lo, J. Analysis of Double Bond Conversion of Photopolymerizable Monomers by FTIR-ATR Spectroscopy. **2019**. https://doi.org/10.1021/acs.jchemed.8b00659.

Chapter 3 *In-situ* Generation of Trithiocarbonate RAFT Agents with a Spirocyclic Precursor

3.1 Introduction

2,2'-(Carbonothioyldisulfanediyl) bis (2-methylpropanoic acid) (**BDMAT**) is a common precursor to synthesizing a variety of functionalized trithiocarbonate RAFT (TTC) agents. Its carboxyl groups provide reaction handles for attaching a variety of desired end groups via coupling reactions that produce an ester or amide linkage. However, all reported modification of **BDMAT** to date is achieved by transforming the diacid into an acyl chloride[1] or via the Mitsunobu reaction[2]. Treating **BDMAT** with coupling agents such as EDC results in the complete conversion of **BDMAT** into a side product that does not react further with alcohols. The isolation of this compound was first reported by Lewis and co-workers.[3]. A cyclic anhydride structure was proposed, as shown in **Figure 3-1**. While the proposed structure agrees with the molecular weight obtained through mass spectrometry, the highly symmetric structure is not consistent with the reported ^{1}H-NMR spectrum, which displays four discrete peaks, indicating that the four methyl groups in the molecule are in distinct chemical environments.

3.2 Results and discussion

BDMAT was subjected to a variety of conditions and coupling reagents *(vide infra)*, all of which resulted in the same side product **Sp**, as observed by TLC and LC-MS. The product can be readily purified with flash column chromatography and is a white solid. The ^{1}H-NMR spectrum and MS is identical to the side product reported by Lewis and co-workers.

All of the attempted coupling reagents transforms the carbonyl group on **BDMAT** into an activated ester. Attack on the activated ester by the other carbonyl results in the proposed cyclic anhydride structure. We proposed a different mechanism in which the sulfur atom on the TTC group acts as the nucleophile as shown in **Figure 3-1**, resulting in a proposed spirocyclic structure.

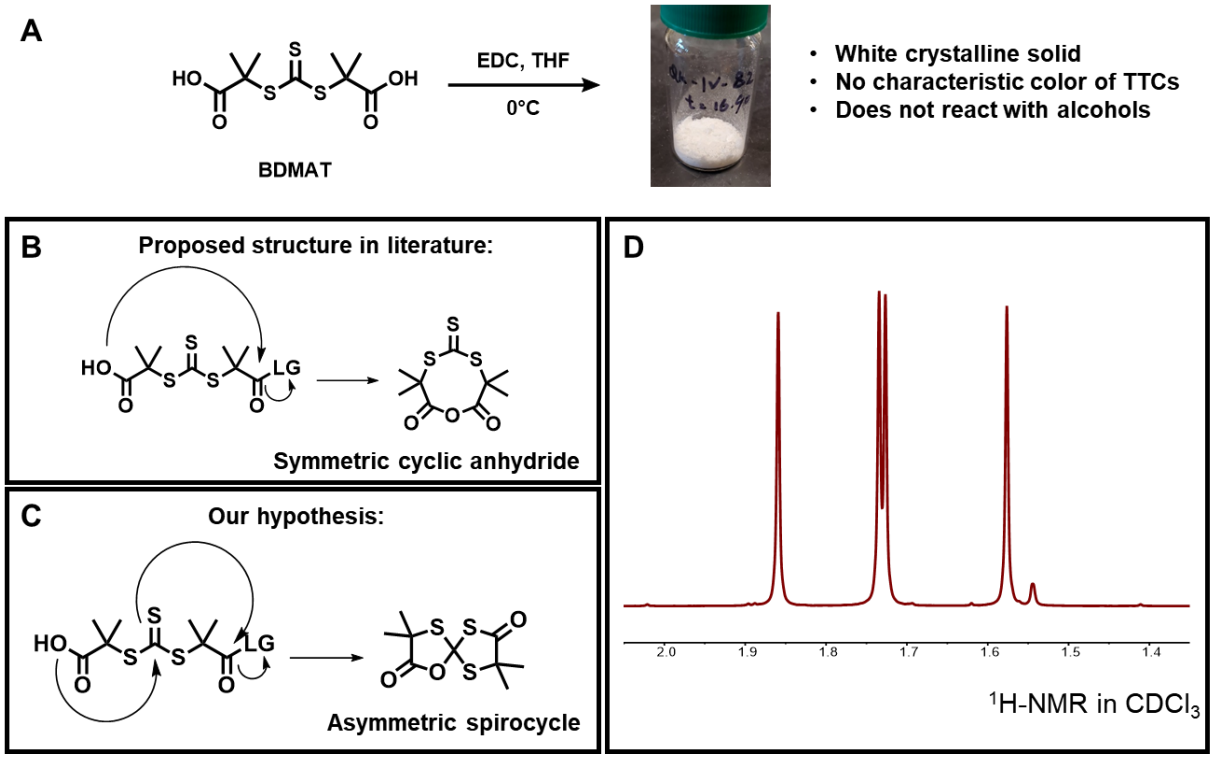

Figure 3-1 A) Reaction conditions that yields **Sp**. B) Proposed structure for **Sp** in literature[3] and proposed reaction mechanism for its formation. C) Proposed structure and mechanism in this work. D) ^{1}H-NMR spectrum of **Sp** in $CDCl_3$

We obtained a single crystal of the compound and resolved its structure with X-Ray crystallography (**Figure 3-2**). The crystallographic structure agrees with the proposed spirocyclic structure. The simulated powder X-Ray diffraction (PXRD) spectrum of the compound based on the single crystal X-Ray diffraction data matched well with PXRD data obtained experimentally. This is further corroborated by the IR spectrum of the spirocyclic structure predicted from DFT calculations, which matches very well with the FTIR spectrum of the compound obtained experimentally (**Figure 3-11**). The simulated IR spectrum of the cyclic anhydride structure does not match the experimental spectrum (**Figure 3-12**).

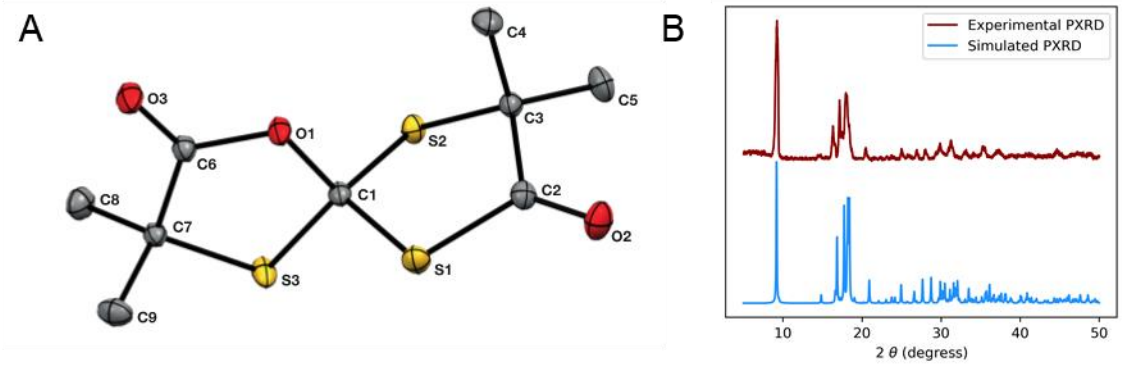

Figure 3-2 A) ORTEP representation of **Sp**. Ellipsoids are plotted at the 50% probability level. Hydrogen atoms removed for clarity. B) Simulated and experimental powder diffraction pattern of **Sp**.

The spirocyclic structure contains a reactive thioester group and is strained so we hypothesized that it can be ring opened with a suitable nucleophile to regenerate a TTC. We attempted to treat it with a variety of alcohols and amines. Generation of TTCs can be detected by monitoring the characteristic n-π* transition of TTCs at around 464nm. **Sp** reacts readily in the presence of a primary amine. Secondary amines react very slowly. Alcohols did not react at all under conditions tested.

An issue with primary amines is that once they generate the TTC, they will proceed to also attack the central carbon atom of the newly formed TTC, resulting in aminolysis of the TTC. A dithiocarbamate is formed first, which can be subsequently attacked by another equivalent of amine for form a thiourea. ^{1}H-NMR experiments(**Figure 3-13**) suggest the generation and the degradation of the TTC occur simultaneously. In addition, as the TTC generated has a carboxyl end group, some amines can be expected to be consumed by acid-base reactions as well. To find optimal conditions for generating TTCs, we treated **Sp** with different equivalents of dodecylamine and monitored the reaction with UV-Vis over the course of 3 days. Dodecylamine is chosen for its low volatility. The reaction between dodecylamine and **Sp** occurs almost instantaneously. However, if an excess of dodecylamine is used, the concentration of TTC will decrease over time, indicating degradation. By measuring the absorption by known concentrations of **BDMAT**, a

structurally similar TTC compound, a calibration curve can be established to estimate the concentration of trithiocarbonate generated.

Next we sought to determine if the generated trithiocarbonate can be used to regulate RAFT reactions.[4–7] In a system with methyl acrylate(MA) as the monomer and azobisisobutyronitrile (AIBN) as the initiator, adding **Sp** and dodecylamine in place of a RAFT agent leads to lower molecular weight and low dispersity compared to uncontrolled free radical polymerization. In fact, molecular weight and dispersity control is similar to those obtained using a coventional trithiocarbonate RAFT agent under the same conditions. No control is observed in the absence of either **Sp** or the amine, as both the molecular weight and dispersity are nearly identical with uncontrolled polymerization. The degradation of TTC also generates dithiocarbamates and thioureas. Thioureas are not known to be capable of mediating RAFT activities. Although dithiocarbamates are known RAFT agents, those without stabilizing groups on the nitrogen atom (such as N,N-dialkyldithiocarbamates) have been shown to have very low transfer constants for acrylate monomers.[8] The monoalkyl ditiocarbamate generated here with a primary amine is even less stabilized and can therefore be expected to have even less RAFT activity. As such, the only possible species that is capable of controlling polymerization is the TTCs that are generated.

Although low dispersities can be achieved at lower molecular weights, attempts to synthesize higher molecular weight polymers lea to a rapid increase in dispersity. While this is an inherent drawback for many RAFT systems, we hypothesize that at elevated temperatures, the amines may be continuing to degrade trithiocarbonates, leading to irregular chain lengths. The presence of thiols may also negatively influence dispersity. However, these drawbacks can be overcome in future work by further optimization of the conditions, such as controlling the equivalents of amine added, or neutralizing the excess amines after the ring opening process, or using a photoinitiator to run the reaction at ambient temperature.

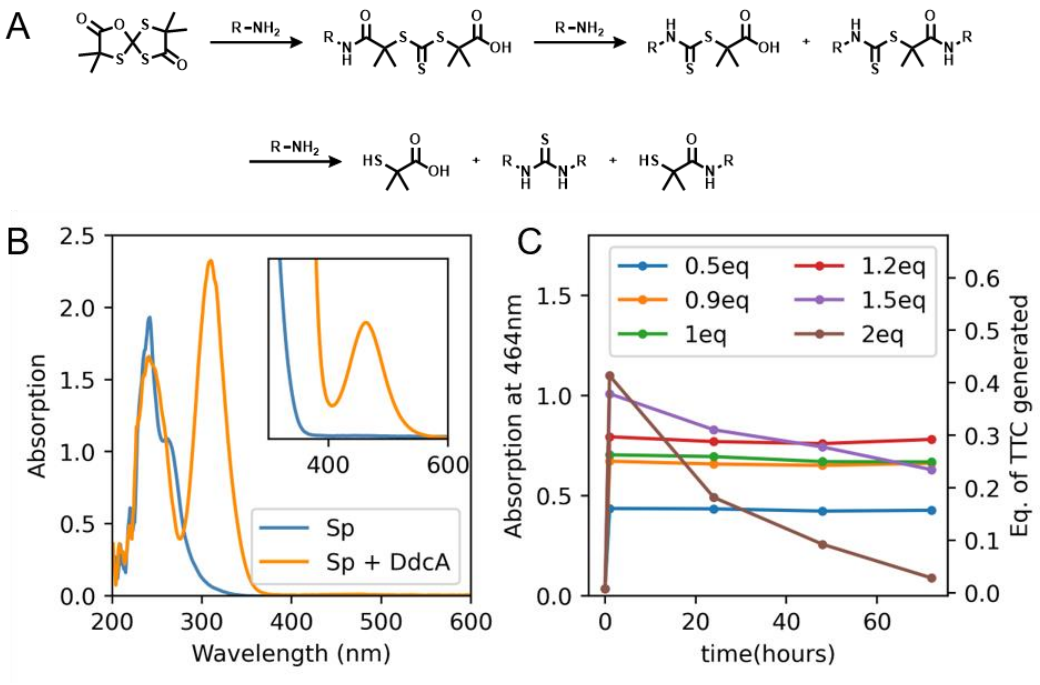

Figure 3-3 A) Proposed reaction pathway for the ring opening and aminolysis of **Sp**. B) UV-Vis spectrum of **Sp** and reacting **Sp** and 1eq of dodecylamine. C) The generation and degradation of trithiocarbonates by reacting **Sp** with dodecylamine, as followed by UV-Vis absorption at 464nm.

Aside from low dispersities, other advantage of controlled radical polymerization are its ability to keep chain ends alive for reinitiation, and its control over chain end functionalities.[9] These properties enable the synthesis of block copolymers and telechelic polymers. In the case of RAFT using TTCs, the R group that flanks the TTC determines the chain end functionality of the resulting polymer. However, if a series of polymers with diverse chain end modifications is desired, one either needs to conduct divergent post-polymerization modification, which can be inefficient, or a different kind of TTC needs to be synthesized for every modification, which can be tedious.

Table 3-1 Reaction conditions to demonstrate control over free radical polymerization by ring opening **Sp** with dodecylamine (**DdcA**), and the number average molecular weight and dispersity of the resulting polymers. *a.* 2-(Dodecylthiocarbonothioylthio)-2-methylpropionic acid (**DMAT**) used as positive control. Its equivalent was calculated from concentration of trithiocarbonate generated in **Sp**-**DdcA** systems, determined via colorimetry.

AIBN	Sp	DdcA	MA	Mn	*Đ*
0.06	1	1.2	30	2679	1.14
0.06	0	1	30	6997	1.65
0.06	1	0	30	6672	1.65
0.06	0	0	30	6762	1.57
0.06	**DMAT** 0.3 eq [a]		30	4132	1.14

As **Sp** readily generates a TTC in-situ with the amine attached to one of its R groups, TTCs with different end groups can be generated simply by varying the amine used. As the TTC end groups determine the end functionality of the polymers synthesized, we wondered if **Sp** could be used as a precursor to quickly generate polymers with desired end functionalities. To demonstrate this, we used 4-Fluorobenzylamine(**4-FBA**) to ring open **Sp**, and to control the polymerization of 2-methoxyethyl acrylate (**2-MEA**) with AIBN as the initiator. 4-fluorobenzylamine was chosen as its presence on polymer chain ends can be detected with ^{19}F NMR. Due to its weaker nucleophilicity compared to dodecylamine (**DdcA**), **4-FBA** takes longer to fully react with **Sp**, thus the reaction is allowed to sit at room temperature for 30min before being heated. After polymerization and precipitation in ether, **4-FBA** can indeed be detected in the purified polymer, indicating successful chain end functionalization. When treated with additional monomers and initiators, the polymers are able to reinitiate and undergo chain extension to achieve higher molecular weight, and **4-FBA** can still be detected in the purified chain extended polymer.

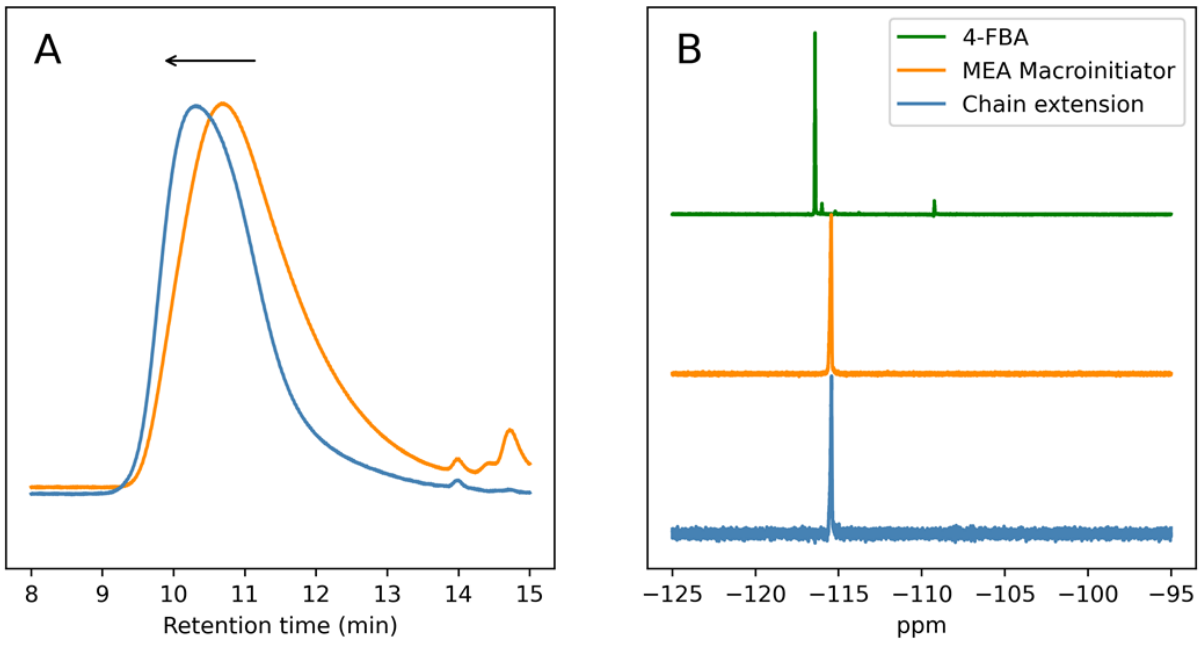

Figure 3-4 (A) GPC trace of poly-MEA macroinitiators prepared by reacting **4-FBA** with Sp, before and after chain extension. (B) ^{19}F-NMR of **4-FBA** and poly-MEA macroinitiators before and after chain extension.

3.3 Conclusion

In conclusion, we have isolated and identified a new spirocyclic compound that is generated upon treating **BDMAT** with certain coupling reagents. Its structure was elucidated with X-Ray crystallography. It can be ring opened *in-situ* with nucleophilic amines to give a trithiocarbonate that is capable of mediating RAFT polymerization. This strategy opens up the possibility of adding logical control to polymerization processes through the presence of amines. In addition, a diverse library of TTCs can be readily generated by using different kinds of amines, which leads to facile divergent synthesis of polymers with diversified end group functionalities. The new compound is easy to prepare in large scales and stable under ambient conditions, lending itself to be a potentially useful reagent in polymer synthesis.

3.4 Experimental Section

3.4.1 General

Unless otherwise specified, all reagents are purchased from Sigma-Aldrich and used as received. Azobisisobutyronitrile was recrystallized from methanol before use. Methyl acrylate(MA) and 2-Methoxyethyl acrylate (**2-MEA**) were run through a plug of neutral alumina to remove inhibitors prior to use. ^{1}H NMR and ^{13}C NMR spectra were recorded on Bruker Avance DRX 400 MHz NMR spectrometers at 22 °C. Signals are reported in δ units, parts per million (ppm), and were measured relative to residual solvent peak ($CDCl_3$: 7.26 ppm). Deuterated chloroform was purchased from Cambridge Isotope Laboratories. UV-Vis measurements were taken on an Implen NP80 NanoPhotometer using Firefly Scientific screw cap cuvettes with 10mm light path. Gel Permeation Chromatography (GPC) measurements were performed on a Tosoh Ecosec HLC-8320 GPC system with three TSKgel Super HZ columns (SuperHZ 4000, SuperHZ 3000, SuperHZ 2500) in tandem at 40°C and a flow rate of 0.6mL/min with Chloroform with 0.75% Ethanol as the mobile phase. Molecular weight determination is performed by calibrating the elution curve in dRI against a calibration curve obtained with Agilent EasiCal PS-2 standards.

3.4.2 Synthesis of S,S''-bis(α,α''-dimethyl-α''-acetic acid)-trithiocarbonate (BDMAT)

S,S''-bis(α,α''-dimethyl-α''-acetic acid)-trithiocarbonate (**BDMAT**) was synthesized following a previously described procedure.

3.4.3 Attempted coupling reactions with BDMAT

250 mg **BDMAT** (0.89 mmol, 1 eq), 255 mg 4-Penten-1-ol (3.54 mmol, 4 eq) and 57 mg DIPEA (0.44 mmol, 0.5 eq) are dissolved in 5mL anhydrous THF and cooled to 0°C. 510 mg N-Ethyl-N′-(3-dimethylaminopropyl) carbodiimide hydrochloride (EDC-HCl, 2.66 mmol, 3 eq) is dissolved in 5mL anhydrous THF and added dropwise to the reaction. Immediately upon addition of EDC-HCl the reaction mixture turned from yellow to colorless. The only isolable product is **Sp**.

The reaction is repeated in dichloromethane (DCM), acetonitrile, acetone and dimethylformamide (DMF) with identical result. Using 4-dimethylaminopyridine (DMAP), triethylamine (TEA) or not using a base at all does not change the outcome. Running the reaction at room temperature or not adding an alcohol also yield the same product. Using N,N′-Dicyclohexylcarbodiimide (DCC) or HBTU also yields the same product.

Interestingly, upon treating **BDMAT** with oxalyl chloride and catalytic amounts of DMF at 0°C the reaction mixture also turned colorless, indication the formation of **Sp**, but upon warming up to room temperature the reaction mixture turned orange the desired ester product can be recovered, suggesting that **Sp** is a kinetically favored product and is susceptible to ring opening by Cl^- to regenerated the acyl chloride.

3.4.4 Synthesis of Sp

1 g **BDMAT** (3.55 mmol, 1 eq) is dissolved in 40 mL anhydrous THF and cooled to 0°C. 1.02 g N-Ethyl-N′-(3-dimethylaminopropyl) carbodiimide hydrochloride (EDC-HCl, 5.31 mmol, 1.5 eq) is added to the reaction. Immediately upon addition of EDC-HCl the reaction mixture turned from yellow to colorless. The reaction is warmed to room temperature and allowed to stir overnight. The reaction is then concentrated with rotary evaporation and redissolved in 200mL DCM, washed three times with water and once with brine, before being dried over anhydrous Na_2SO_4. **Sp** is purified with flash column chromatography in 1:19 EtOAc-Hexane as a white crystalline solid with 75% yield. ^{1}H NMR (400 MHz, Chloroform-d) δ 1.88 (s, 1H), 1.76 (d, J = 3.1 Hz, 2H), 1.60 (s, 1H). ^{13}C NMR (101 MHz, Chloroform-d) δ 67.19, 53.78, 30.28, 28.56, 27.82, 23.50.

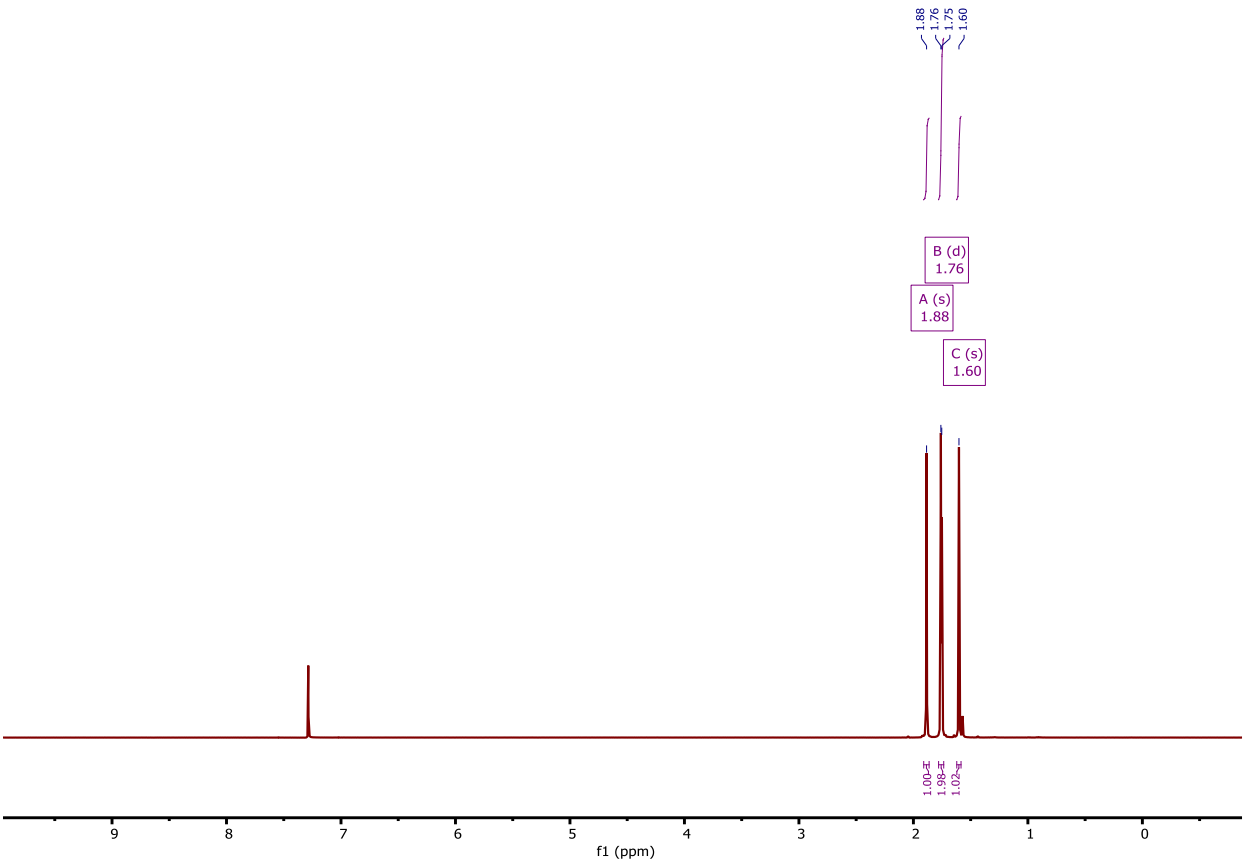

Figure 3-5 ^{1}H NMR (400 MHz, $CDCl_3$) of **Sp**

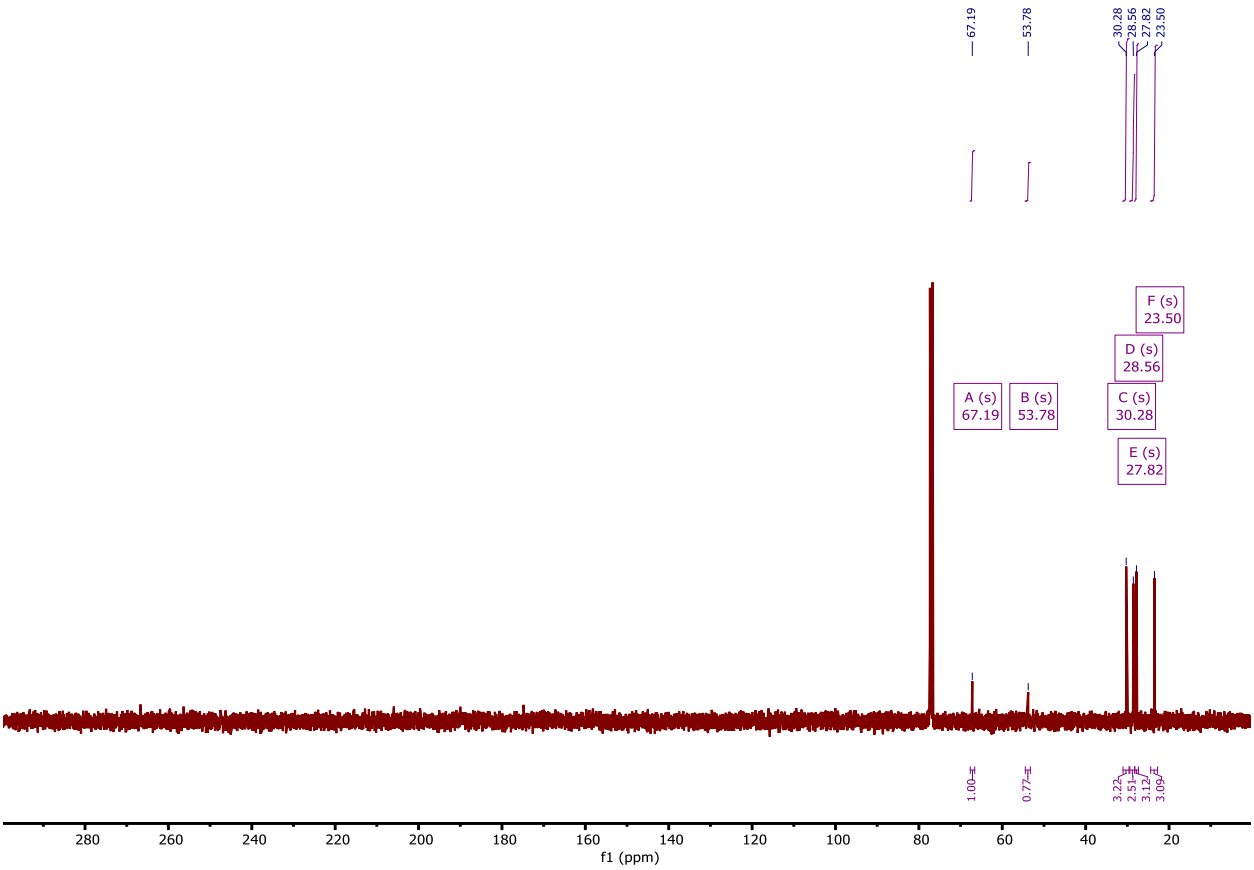

Figure 3-6 ^{13}C NMR (101 MHz, $CDCl_3$) of **Sp** in $CDCl_3$

3.4.5 2D NMR of Sp

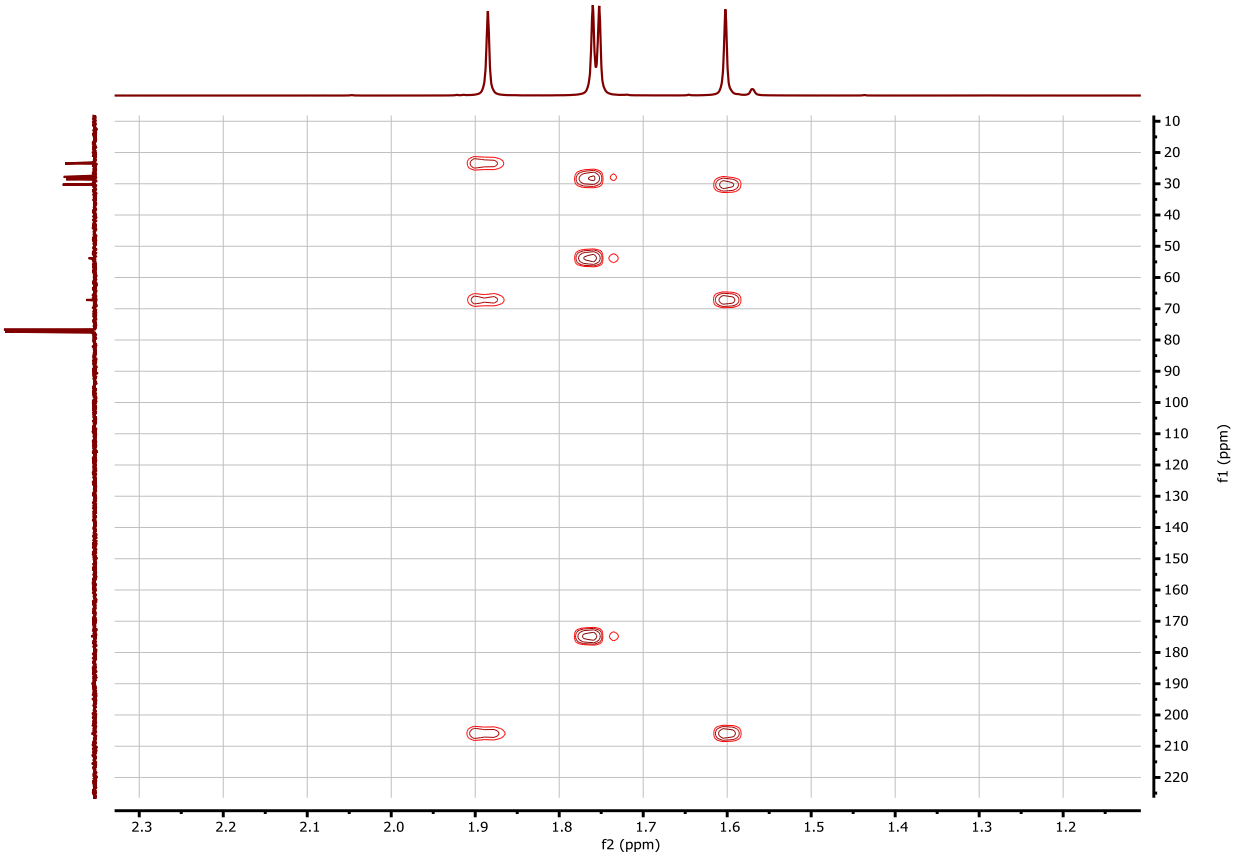

Figure 3-7 ^{1}H-^{13}C HMBC NMR spectrum of **Sp**

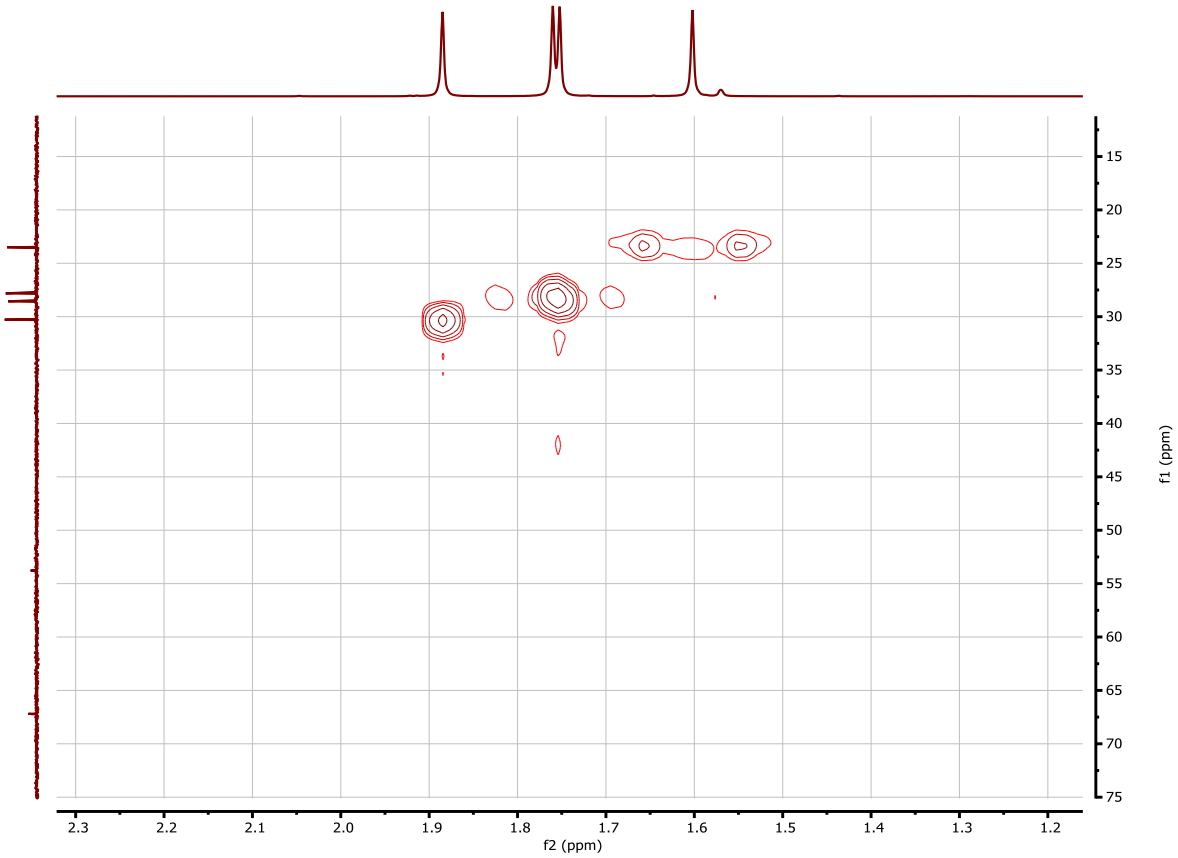

Figure 3-8 ^{1}H-^{13}C HSQC NMR spectrum of **Sp**

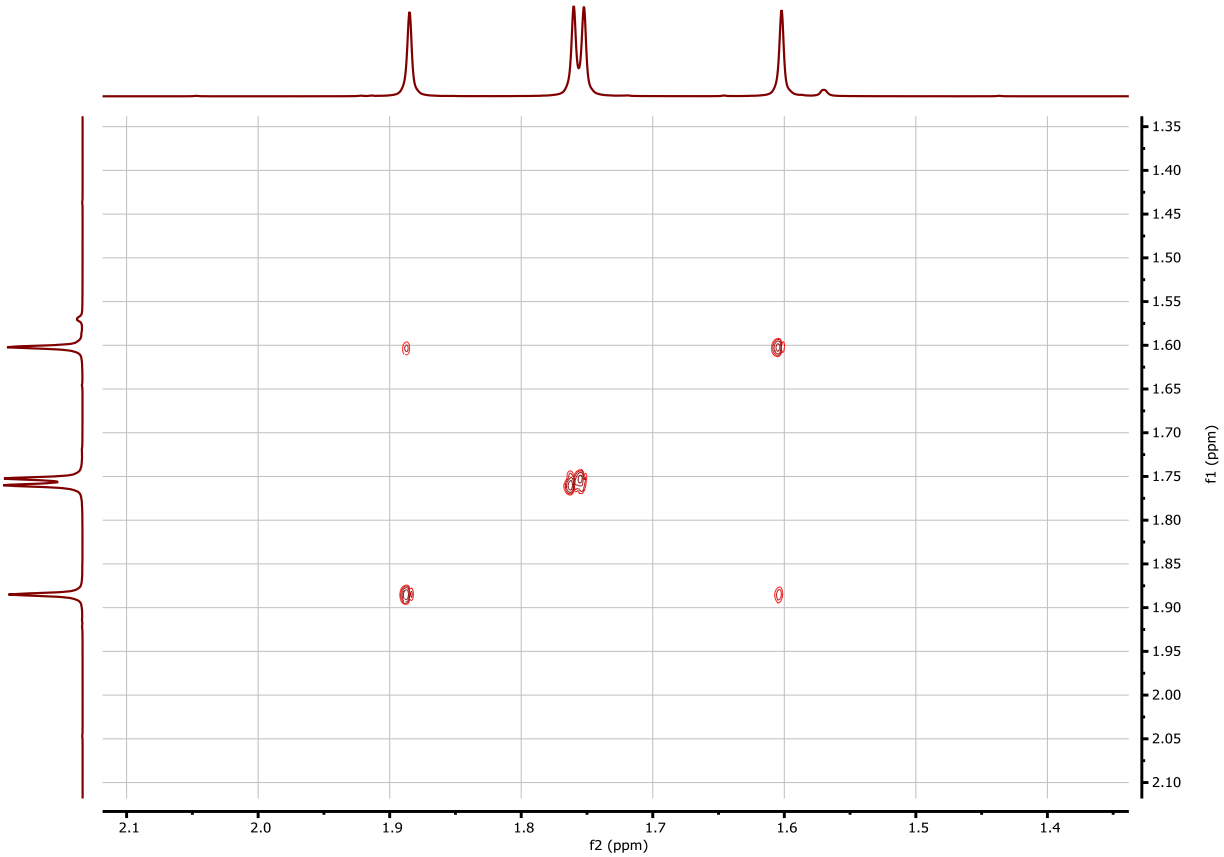

Figure 3-9 ^{1}H-^{1}H COSY NMR Spectrum of **Sp**

3.4.6 Fourier Transform Infrared Spectroscopy(FTIR)

FTIR is performed on a Bruker ALPHA II FTIR spectrometer equipped with a Platinum ATR module.

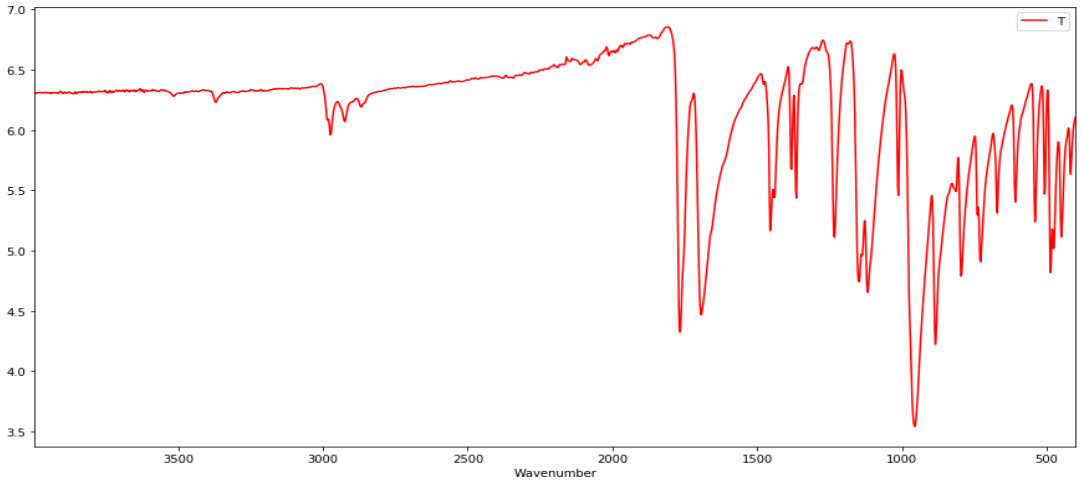

Figure 3-10 FTIR spectrum of **Sp** powder

3.4.7 DFT Calculations

DFT calculations were performed using Spartan 14. A conformer search is first performed with PM6. Geometry optimizations and frequency calculations were both performed with DFT to B3LYP/6-31G(d) level. The spirocyclic structure is predicted to have only one conformer, the predicted IR and ^{1}H-NMR spectra of which matched very well with those obtained experimentally. Conformation search of the cyclic anhydride structure yielded 4 conformers. All of them were predicted to have one peak in ^{1}H-NMR, and their predicted IR spectrum did not match that of the experimental.

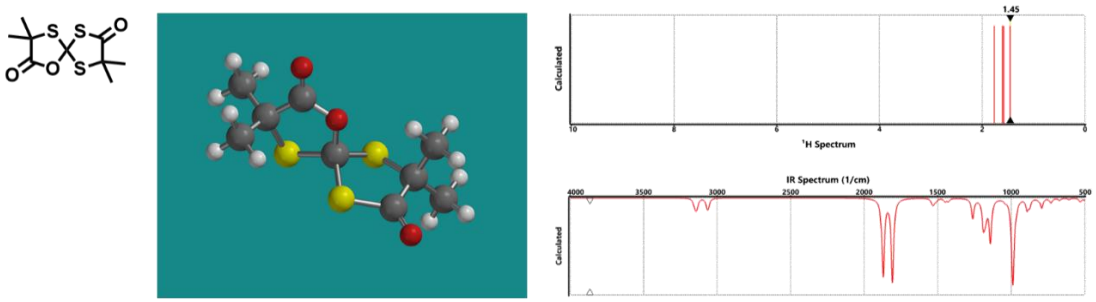

Figure 3-11 Energy minimized geometry and predicted ^{1}H-NMR and FTIR spectra of the proposed spirocyclic structure

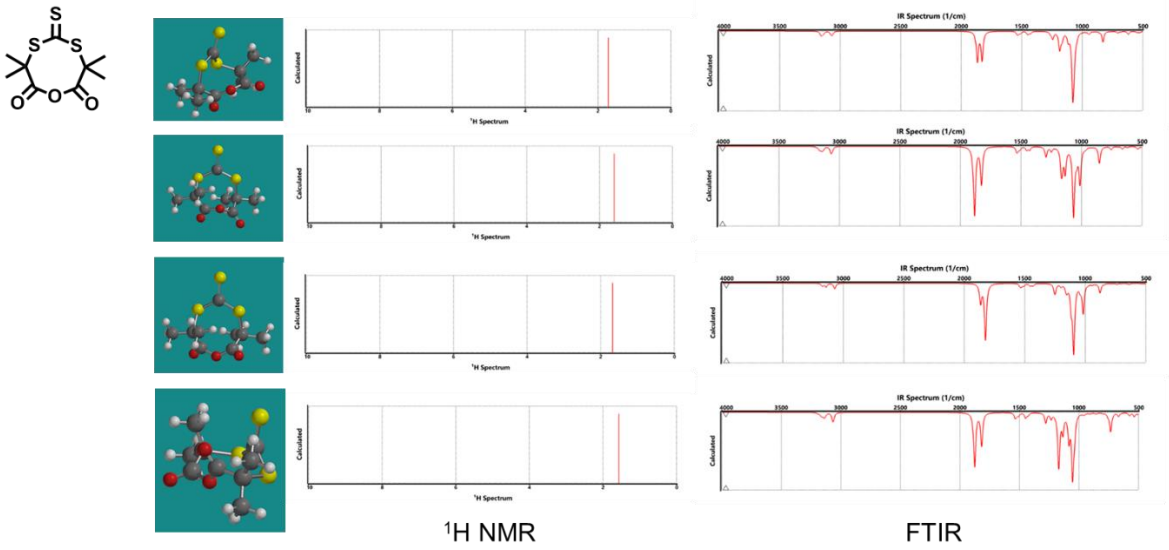

Figure 3-12 Energy minimized geometry and predicted ^{1}H-NMR and FTIR spectra of the proposed cyclic anhydride structure

3.4.8 ^{1}H-NMR Study of ring opening products

25 mg **Sp** (0.088 mmol) and 9.5 mg (0.088 mmol) benzylamine were each dissolved in 0.3mL $CDCl_3$ and mixed in an NMR tube. A ^{1}H-NMR spectrum is taken immediately upon mixing and then after 5h. ^{1}H-NMR shows complete consumption of benzylamine. Two new species were observed and their proposed structures are shown in **Figure 3-10**.

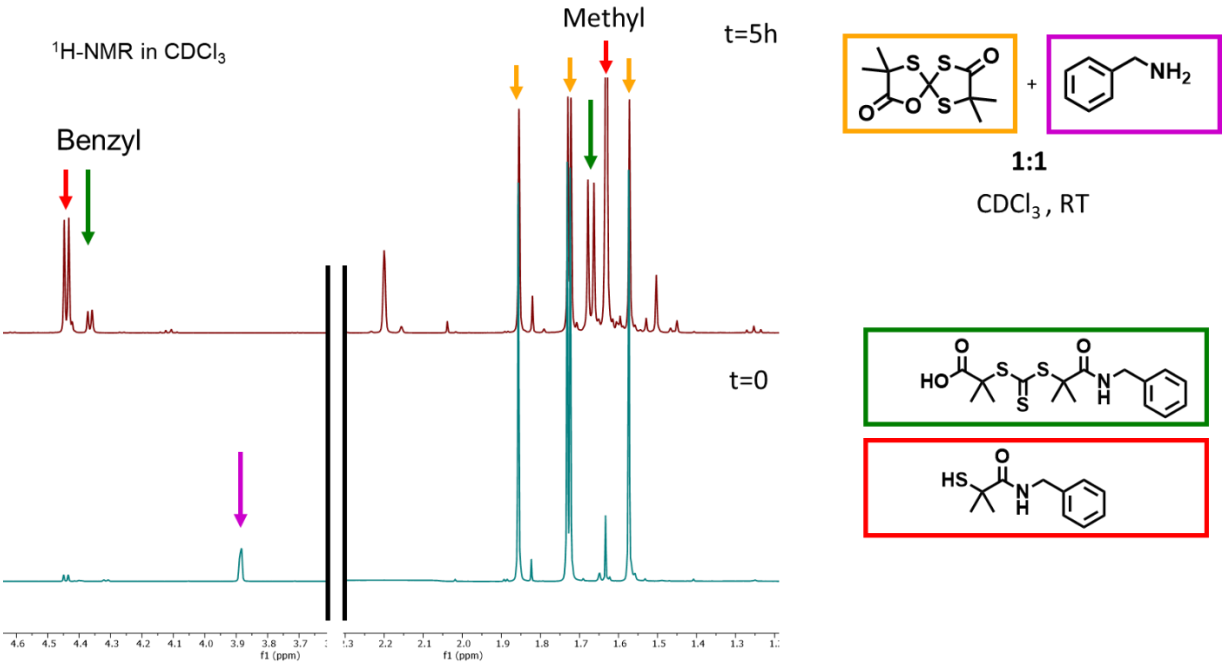

Figure 3-13 ^{1}H-NMR monitoring of the reaction between **Sp** and benzylamine. Orange arrows indicate unreacted **Sp**. Green arrows indicate newly formed ring opening product. Red arrows indicate newly formed degradation product.

3.4.9 Kinetic UV-Vis study of ring opening reaction of Sp by Dodecylamine

51.6 mg (0.2 mmol, 1 eq) **Sp** and 44 µL (0. 2 mmol, 1 eq) dodecylamine are separately dissolved in 1.5 mL THF and mixed in a UV cuvette. Absorption at 464nm is monitored to quantify the generation of TTCs.

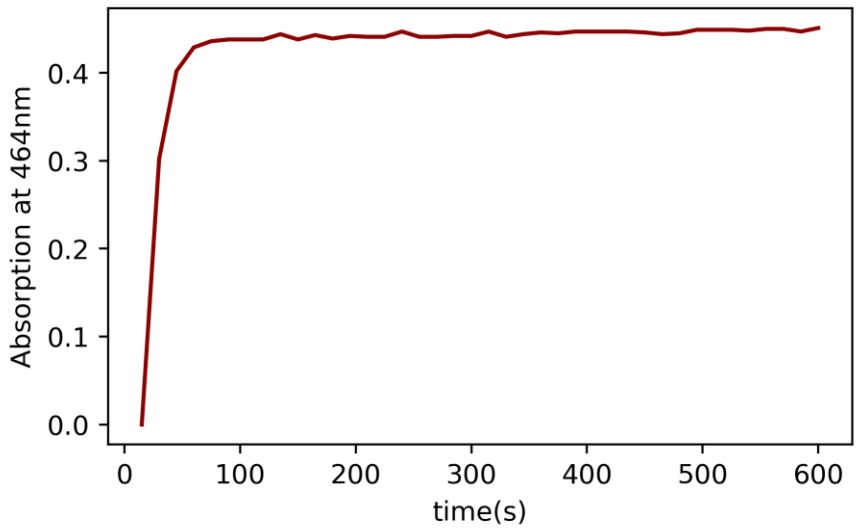

Figure 3-14 Kinetics of TTC generation by reacting **Sp** with **DdcA**, as monitored by UV-Vis absorption at 464nm.

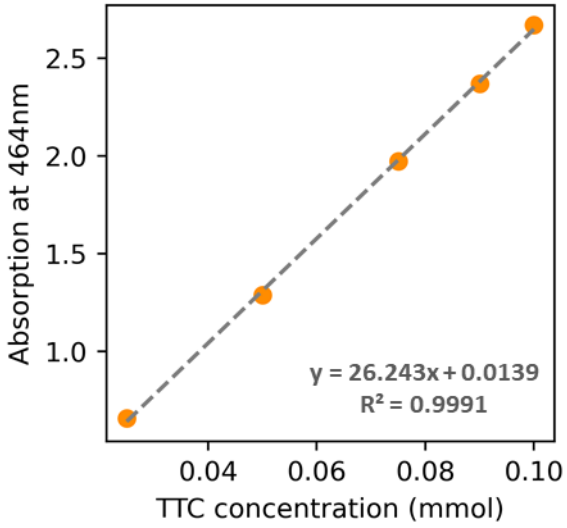

Figure 3-15 Calibration curve of UV absorption against concentration of **BDMAT**

3.4.10 General procedure for RAFT reactions of MA

A 4mL vial is equipped with a magnetic stirbar and charged with 1 mg AIBN (0.006 mmol, 0.06 eq) and 26.4 mg **Sp** (0.1 mmol, 1 eq). 1.5 mL THF was added to dissolve the solids. 271µL (3 mmol, 30 eq) MA was then added. 22.2 mL (0.12 mmol, 1.2 eq) Dodecylamine was added last.

The mixture was freeze-pump-thawed for three cycles, let stand for 5min at room temperature for the amine to fully react with **Sp** at which point the mixture turns from colorless to yellow. The mixture was then heated at 70°C for 2h after which crude samples were taken and analyzed with GPC.

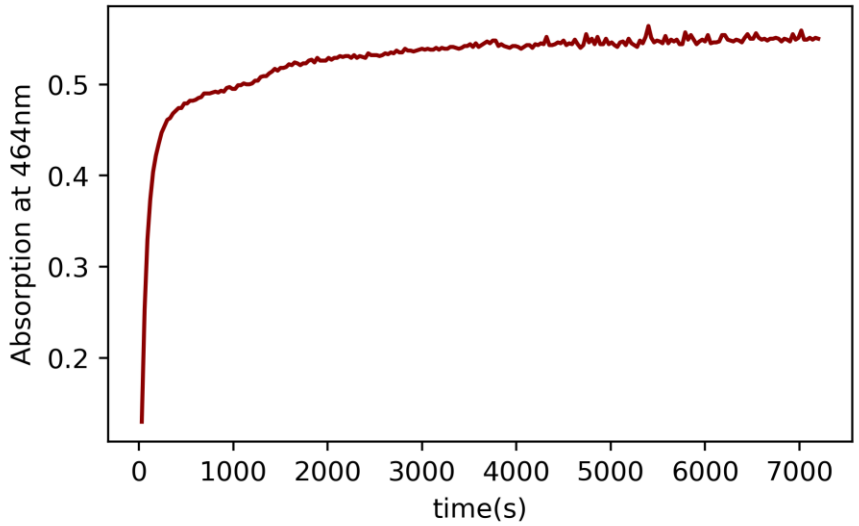

Figure 3-16 Kinetics of trithiocarbonate generation by reacting **Sp** with **4-FBA**, as monitored by UV-Vis absorption at 464nm.

3.4.11 Synthesis of MEA macroinitiator

A 40mL vial is equipped with a magnetic stirbar and charged with 4.92 mg AIBN (0.03 mmol, 0.06 eq) and 132mg **Sp** (0.5 mmol, 1 eq). 7.5mL THF was added to dissolve the solids. 3.2mL (25 mmol, 50 eq) MEA was then added. 75mg (0.12 mmol, 1.2 eq) Dodecylamine was added last. The mixture was freeze-pump-thawed for three cycles, let stand for 30min at room temperature for **4-FBA** to fully react with **Sp** at which point the mixture turns from colorless to yellow. The mixture was then heated at 70°C for 2h after which the reaction mixture is precipitated in 500mL cold diethyl ether three times. MEA macroinitiator was yielded as a slightly yellow oil. The macroinitiaor was analyzed by GPC to have an M_n of 6kDa and dispersity of 1.50.

3.4.12 Chain extension of MEA

A 40mL vial is equipped with a magnetic stirbar and charged with 260 mg MEA macroinitiator (0.4 mmol, 1eq), 282 mg MEA (2.2 mmol, 55 eq) and 0.7 mg AIBN (0.00 4 mmol, 0.1 eq) and dissolved in 7.5mL THF. The mixture was freeze-pump-thawed for three cycles and then heated at 70°C for 2h after which the reaction mixture is precipitated in 100mL cold diethyl ether three times. Chain extended MEA was yielded as a slightly yellow oil, with M_n of 10kDa and dispersity of 1.27.

References

(1) Chen, M.; Gu, Y.; Singh, A.; Zhong, M.; Jordan, A. M.; Biswas, S.; Korley, L. T. J.; Balazs, A. C.; Johnson, J. A. Living Additive Manufacturing: Transformation of Parent Gels into Diversely Functionalized Daughter Gels Made Possible by Visible Light Photoredox Catalysis. *ACS Cent. Sci.* **2017**, *3* (2), 124–134. https://doi.org/10.1021/acscentsci.6b00335.

(2) Amamoto, Y.; Kamada, J.; Otsuka, H.; Takahara, A.; Matyjaszewski, K.; Amamoto, Y.; Kamada, J.; Matyjaszewski, K.; Otsuka, H.; Takahara, A. Repeatable Photoinduced Self-Healing of Covalently Cross-Linked Polymers through Reshuffling of Trithiocarbonate Units. *Angew. Chemie Int. Ed.* **2011**, *50* (7), 1660–1663. https://doi.org/10.1002/ANIE.201003888.

(3) Lewis, R. W.; Malic, N.; Saito, K.; Cameron, N. R.; Evans, R. A.; Lewis, R. W.; Cameron, R.; Malic, N.; Evans, R. A.; Saito, K.; Cameron, N. R. Linear Coordination Polymer Synthesis from Bis-Catechol Functionalized RAFT Polymers. *Macromol. Rapid Commun.* **2020**, *41* (18), 2000366. https://doi.org/10.1002/MARC.202000366.

(4) Mayadunne, R. T. A.; Rizzardo, E.; Chiefari, J.; Chong, Y. K.; Moad, G.; Thang, S. H. Living Radical Polymerization with Reversible Addition-Fragmentation Chain Transfer (RAFT Polymerization) Using Dithiocarbamates as Chain Transfer Agents. https://doi.org/10.1021/ma9906837.

(5) Keddie, D. J.; Moad, G.; Rizzardo, E.; Thang, S. H. RAFT Agent Design and Synthesis. *Macromolecules*. American Chemical Society July 10, 2012, pp 5321–5342. https://doi.org/10.1021/ma300410v.

(6) Moad, G.; Rizzardo, E.; Thang, S. H. Radical Addition–Fragmentation Chemistry and RAFT Polymerization. *Ref. Modul. Mater. Sci. Mater. Eng.* **2016**. https://doi.org/10.1016/B978-0-12-803581-8.01349-7.

(7) Moad, G. RAFT Polymerization. In *RAFT Polymerization*; Wiley, 2021. https://doi.org/10.1002/9783527821358.

(8) Moad, G. A Critical Survey of Dithiocarbamate Reversible Addition-Fragmentation Chain Transfer (RAFT) Agents in Radical Polymerization. *J. Polym. Sci. Part A Polym. Chem.* **2019**, *57* (3), 216–227. https://doi.org/10.1002/POLA.29199.

(9) Lamb, J. R.; Qin, K. P.; Johnson, J. A. Visible-Light-Mediated, Additive-Free, and Open-to-Air Controlled Radical Polymerization of Acrylates and Acrylamides. *Polym. Chem.* **2019**, *10* (13). https://doi.org/10.1039/c9py00022d.

Chapter 4 Design, Synthesis, and 3D Printing of a Photoswitching Polymer Metal-Organic Cage Gel

4.1 Introduction

Materials chemists have relied on the incorporation of dynamic bonds that can be controlled through a specific external stimulus (e.g., light, force, heat, electricity) to give rise to a host of novel "stimuli-responsive" materials with properties that could be altered to achieve a desired function.[1–16] These dynamic bonds, however, are often binarily actuated by this stimulus, resulting in two-state materials that return to the initial state upon the removal of the stimulus. Recently, a new concept has emerged for polymer network design wherein supramolecular interactions are leveraged to produce materials that reversibly switch topological structure in response to a given set of stimuli and that are subsequently stable in each state upon removal of the stimulus.[17,18] For example, by using photo-switchable dithienylethene-based polymer ligands to link Pd-based metal-organic cages (MOCs), a "polyMOC" material capable of alternating between Pd_3L_6 and $Pd_{24}L_{48}$ topological states with different static and dynamic mechanical properties was reported.[18]

Herein, we introduce polyMOC gels derived from Cu(II) and polymer strands with m-benzenedicarboxylate (*m*-BDC = L) termini (e.g., 4 **PL**, **Figure 4-1**A). A combination of small/wide-angle X-ray scattering (SAXS/WAXS), UV-vis absorption, rheology, and simulation experiments supported a polyMOC network structure composed of high branch functionality MOC junctions interconnected by flexible polymer strands. In particular, the high branch functionality of these polyMOCs leads to mechanically robust materials with MOC junctions that can be modularly functionalized without impacting the mechanical properties of the material. Leveraging this unique aspect of the polyMOC topology,[19] we demonstrate the installation of coumarin-based *m*-BDC ligands (**CL**) that, in the presence of a photosensitizer and a hydrogen atom donor, facilitate controlled reduction of the Cu centers within the MOC junctions of the material, thereby enabling photoswitching between three distinct redox states (Cu(II), Cu(I), and Cu(0)) that each display dramatically different mechanical, optical, catalytic, and electronic properties (**Figure 4-1**B). We utilize this material to introduce a fundamentally new way to form interpenetrating networks, in this case a "metal-organic cage interpenetrating networks" (MINs), by leveraging the Cu(I) polyMOC functional state to catalyze the formation of a covalent network and subsequent switching back to the Cu(II) state to reform a polyMOC. The resulting MIN has >100-fold increased toughness compared to the polyMOC and the covalent network alone. Moreover,

because this process is photoinduced, we can leverage the mechanical robustness and dynamics of the polyMOC to 3D pattern and print MINs of arbitrary shape, addressing a major challenge in the field of 3D printing of gels.

4.2 Results and Discussions

4.2.1 Synthesis and properties of Cu-based polyMOCs (*s*-Gel)

When **PL** was combined with *m*-BDC in a 1:3 ratio with respect to *m*-BDC groups (each **PL** contributes 4 *m*-BDC groups) and mixed with a dimethylformamide (DMF) solution of Cu(II) acetate (Note: 5.3wt. % polymer was used for these studies; polymer concentrations as low as 2 wt. %, however, still formed robust gels) (**Figure 4-2**A). Gelation occurred immediately; annealing for 4 h at 60 °C provided a translucent blue gel (*s*-Gel) with a maximum absorption (λ_{max}) at 724 nm (**Figure 4-2**B), which is diagnostic of the paddlewheel complexes in the desired *m*-BDC-based $Cu_{24}L_{24}$ MOCs.[20] The small- and wide-angle X-ray scattering (SAXS/WAXS) curve (**Figure 4-2**C) for *s*-Gel displayed two peaks: one in the high *q* region (0.47 $Å^{-1}$) that corresponds to the form factor of a ~2.7 nm spherical particle, which agrees well with the size of the cuboctahedral $Cu_{24}L_{24}$ MOC,[21] and a broad peak at low *q* (~0.07 $Å^{-1}$) that provides the average distance between the MOC junctions (~9 nm). These two peaks, which are unique to the spherical shape of the MOC and the predictable inter-MOC distance within the network, respectively, are strong indicators of the presence of nanoscale MOCs within the material. In oscillatory rheology frequency sweep studies, *s*-Gel behaved as an elastic solid ($G' > G''$) at all measured frequencies (0.1 to 100 rad/s) with $G' = 6.6$ kPa @ 10 rad/s (**Figure 4-2**D). This modulus value is consistent with the presence of high branch functionality junctions as expected for the proposed polyMOC structure. $Cu_{24}L_{24}$ MOCs are known to undergo rapid ligand exchange in solution,[20,22] which in the case of *s*-Gel could provide a mechanism for stress relaxation. Indeed, *s*-Gel relaxes stress (**Figure 4-2**E) with a characteristic relaxation time (τ) of 132 ± 5 s at room temperature, which is ~100-fold less than previously reported polyMOCs with cuboctahedral $Pd_{12}L_{24}$ MOC junctions at 55 °C.[19]

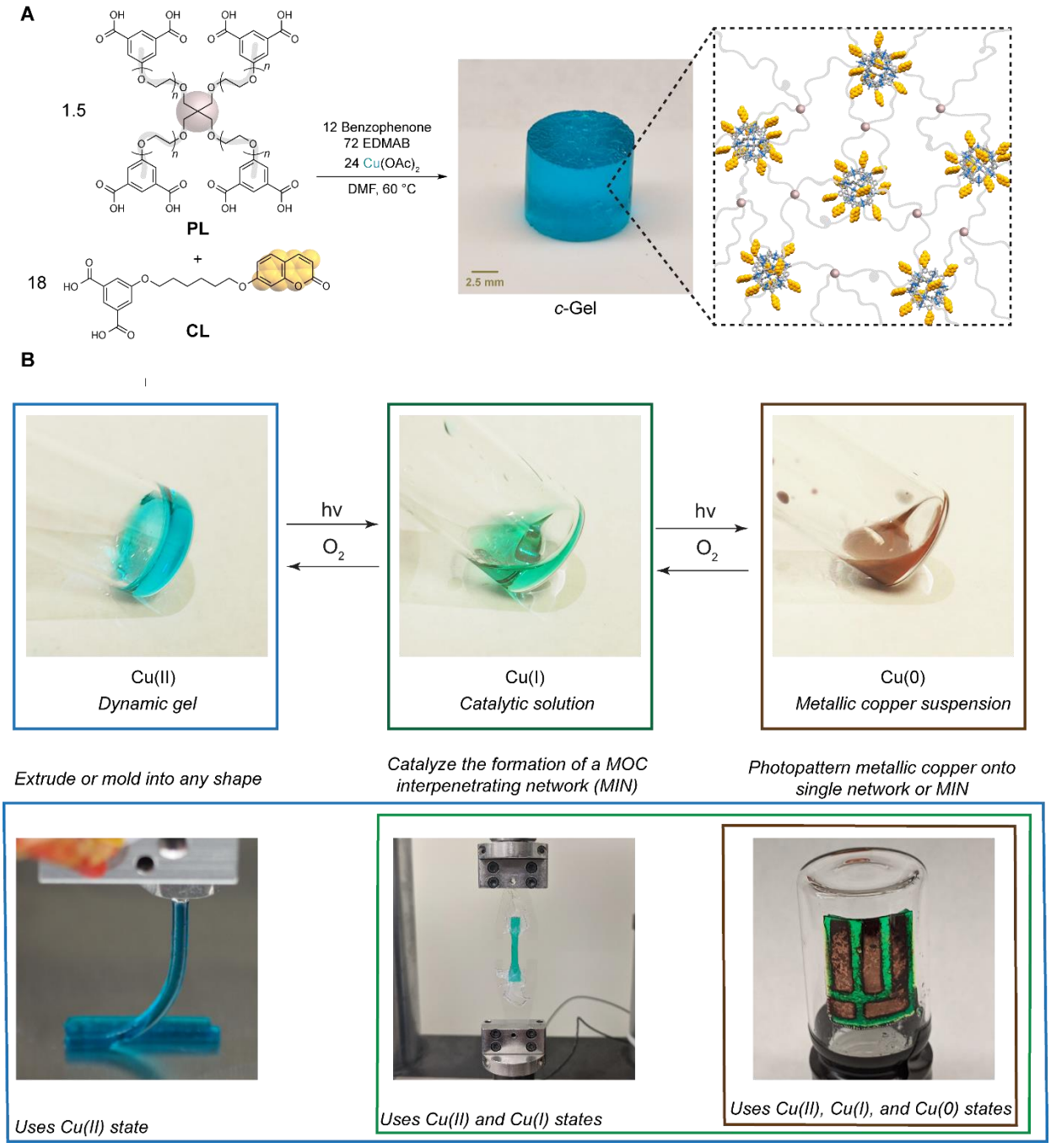

Figure 4-1 Design of Cu24L24-based polyMOCs featuring coumarin-functionalized junctions. A) Readily accessible m-BDC-functionalized PEG star polymer **PL** and coumarin-functionalized *m*-BDC (**CL**) are combined with $Cu(OAc)_2$. Annealing provides coumarin-functionalized polyMOC *c*-Gel, which is comprised of $Cu_{24}L_{24}$ junctions densely functionalized with coumarins and polymer

strands from **CL** and **PL**, respectively. The Cu(II) state of this material provides its deep 21 blue color. B) Combining this material with suitable reagents and exposing it to light or oxygen enables its reversible interconversion between primarily Cu(II), Cu(I), and Cu(0) functional states. The properties of each state can be used alone or the different states can be leveraged against one another for more advanced functions.

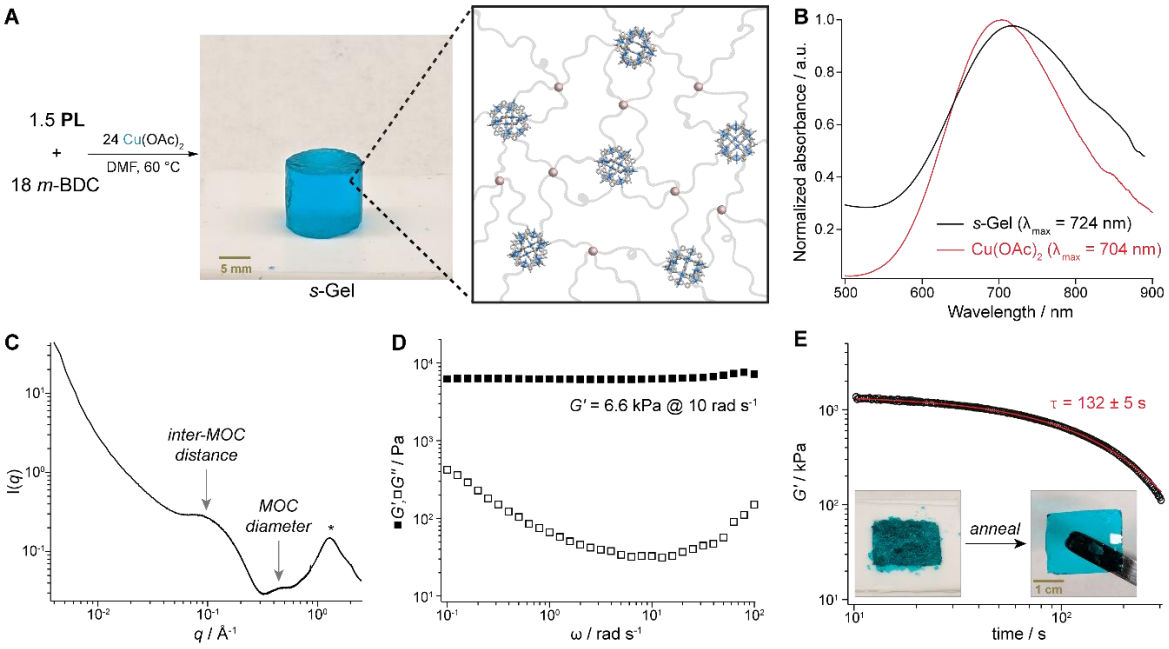

Figure 4-2 Synthesis and characterization of star polymer-based $Cu_{24}L_{24}$ polyMOC s-Gel. *a*, Synthesis and schematic representation of s-Gel. DMF = N,N-dimethylformamide. *b*, UV-vis spectrum of s-Gel network (black line) showing the red-shifting of λ_{max} to 724 nm compared to copper acetate (red line). This red shift is indicative of the formation of Cu-*m*-BDC paddlewheel complexes. *c*, SAXS/WAXS curve depicting the spacing between $Cu_{24}L_{24}$ MOCs within s-Gel as well as the form factor of the individual MOCs. *d*, Frequency sweep rheology curve for *s*-Gel (5.3 wt. %) swollen to equilibrium in DMF. e, Stress relaxation curve for *s*-Gel. The red line corresponds to fitting of the data using the Kohlrausch stretched exponential model, which provide the characteristic relaxation time t. Inset: Image

of *s*-Gel mashed into several pieces (left). Placing the mashed sample in a mold and applying pressure leads to complete healing (right).

4.2.2 Reversible photoswitching of coumarin functionalized $Cu_{24}L_{24}$ polyMOCs (*c*-Gel)

The photo-induced reduction of Cu(II) complexes in the presence of benzophenone and hydrogen donors is well-known.[23–26] Recently, Park and coworkers[27] applied this strategy to the photoreduction of Cu_{24}*m*-BDC_{24} MOCs bearing exohedral coumarin ligands, the latter of which were required for accessing the Cu(I) state in a controlled manner (as opposed to rapid reduction to Cu(0)). A distinguishing feature of polyMOCs is their ability to be modularly functionalized by the addition of small molecule ligands[19] into the network junctions without affecting their mechanical properties, which is not possible in traditional supramolecular networks based on point metal-ligand complexes as junctions.

Here, we leverage this capability for the installation of coumarin-based *m*-BDC into the junctions of *s*-Gel (providing "*c*-Gel"), enabling controlled photoreduction of the network junctions from Cu(II) to Cu(I). It was hypothesized that such a photoreduction would disrupt the paddlewheel complexes within these $Cu_{24}L_{24}$ MOCs and induce a corresponding change in the network topology. Moreover, selective access to a catalytically active species (here, Cu(I)) could enable the chemical remodeling of the material in a way that creates new multi-material properties, for example through the polymerization of polymeric azides and alkynes.

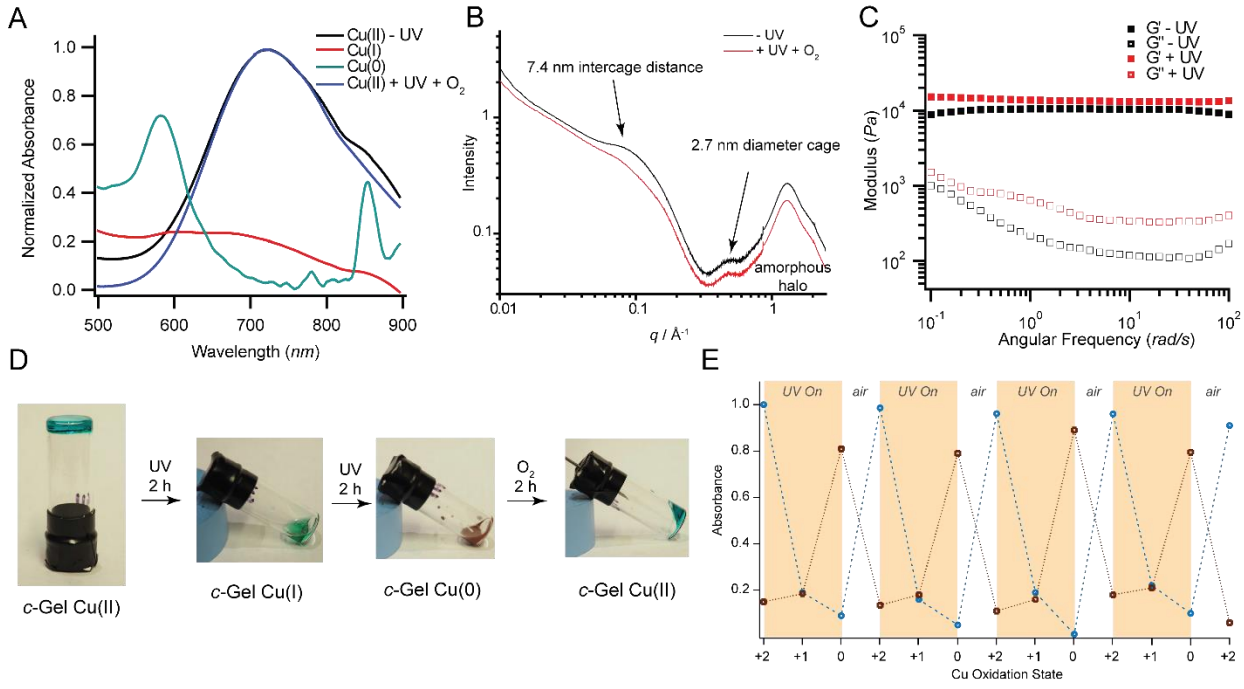

Figure 4-3 Multi-state switching of c-Gel in the presence of benzophenone and EDMAB. A) UV-vis spectra of the material (6.6 wt. %) before UV exposure (black line), in the Cu (I) state (red line), in the Cu (0) state (gray line), and after oxidation via exposure to air (blue line). B) SAXS/WAXS curves for c-Gel before (black) and after UV exposure and re-oxidation (red). The structure of the Cu(II) c-Gel is restored upon re-oxidation. C) Frequency sweep rheology curves for c-Gel before (black) and after UV exposure and re-oxidation (red). The slight increases in the storage and loss moduli are attributed to a small amount of solvent evaporation during the course of the 25 switching and re-oxidation processes. D) Images of c-Gel as it proceeds through a full switching cycle. After 2 h of UV exposure the gel converts into a green fluid, which further converts into a brown opaque liquid after 2 additional hours of UV exposure. 16 h after exposure to air the blue Cu(II) c-Gel is re-formed. E) Switching of c-Gel through 4 complete cycles (12 total state conversions) as monitored by UV-vis spectroscopy. The blue circles represent absorbance at 724nm corresponding to the Cu (II) state, while the brown squares represent absorbance at 580nm corresponding to the Cu(0) state. Dashed lines are drawn between points to aid the viewer; they are not mathematical fits or actual

data. Note: oxidation labels indicate the primary functional oxidation state of the material; they are not intended to imply that 100% of the Cu centers have a given oxidation state.

To prepare coumarin functionalized $Cu_{24}L_{24}$ polyMOCs (*c*-Gel), **PL** was combined with **CL** in a 1:3 ratio with respect to *m*-BDC groups and Cu(II) acetate (6.6 wt. % polymer) (**Figure 4-1**). Park and coworkers[27] reported on the use of a mixture of benzophenone, N,N-dimethylformamide, and methanol or THF to achieve controlled photoreduction of discrete coumarin-based MOCs in solution. Searching for conditions to achieve a similar photoreduction in the context of materials, where solvent evaporation and long-term storage stability are concerns, we screened several alternatives and identified ethyl-4-(dimethylamino)benzoate (EDMAB) as a suitable H-donor to achieve, in combination with benzophenone, controlled photoreduction of our polyMOCs. Thus, EDMAB (3 equiv relative to Cu) and benzophenone (0.5 equiv relative to Cu) were added and the mixture was annealed for 4 h at 60 °C. The resulting material, *c*-Gel, displayed the characteristic λ_{max} = 724 nm of Cu(II) paddlewheel complexes (**Figure 4-3**A) while the SAXS/WAXS (**Figure 4-3**B) and frequency sweep rheology (**Figure 4-3**C) results were similar to those of *s*-Gel, suggesting that, as expected for the unique high branch functionality polyMOC topology, coumarin incorporation and the presence of EDMAB and benzophenone have little effect on the structure and topology of the polyMOC network. Strikingly, when *c*-Gel was exposed to 368 nm light (FL8BLB-368 8W bulb) under N_2 atmosphere, it converted over the course of 2 h into a transparent green liquid (**Figure 4-3**D). This solid-to-liquid phase transition along with disappearance of the 724 nm absorbance peak (red line, **Figure 4-3**A) are consistent with photoinduced reduction of the Cu(II) polyMOC to a primarily 7 Cu(I) state. The material was stable in this state indefinitely under N_2 atmosphere, while exposure to 368 nm light for an additional 2 h produced an opaque brown liquid (**Figure 4-3**A) with λ_{max} = 580 nm (grey line, **Figure 4-3**A), which is consistent with the formation of Cu(0)[28]. Once again, the material was indefinitely stable in this state under N_2 atmosphere. Exposing either the primarily Cu(I) or Cu(0) solutions to ambient air, however, led to their slow conversion back to Cu(II) *c*-Gel with λ_{max} = 724 nm (blue line, **Figure 4-3**A; **Figure 4-3**D), an identical SAXS/WAXS profile (red line, **Figure 4-3**B), and a similar G′ value compared to *c*-Gel (red line, **Figure 4-3**C) (10.3 kPa vs 13.1 kPa @

10 rad/s before and after photoreduction/re-oxidation, respectively; the increase in G′ is attributed to solvent evaporation during the re-oxidation process). This switching between the primarily Cu(II), Cu(I), Cu(0) and back to Cu(II) states was repeated for 4 cycles without the addition of any new reagents, which corresponds to 12 separate state transformations for a single sample (**Figure 4-3**D). We note that the photoreduction required a longer irradiation time with subsequent cycles (~4 h for the fourth cycle compared to ~2 h for the first cycle) likely due to the consumption of EDMAB during each photoreduction step; more EDMAB can be added to the material to enable further switching if desired).

4.2.3 Cu(I)-catalyzed formation of covalent secondary network in *c*-Gel

Inspired by Park and coworkers,[27] who used photoreduction of discrete $Cu_{24}L_{24}$ MOCs in solution to induce a Cu(I)-catalyzed azide-alkyne cycloaddition (CuAAC) between small molecule reactants, we anticipated that reduction of *c*-Gel could be used to create new material functionality. Specifically, we envisioned that the Cu(I) functional state of *c*-Gel could serve as a catalyst for the formation of a covalent polymer network via copper-catalyzed azide-alkyne cycloaddition (CuAAC) of suitable polymeric azides and alkynes. Then, re-oxidation to the Cu(II) state would provide a Metal-organic cage interpenetrating network (MIN) that is composed of both the $Cu_{24}L_{24}$ polyMOC and a secondary covalent network. Related interpenetrating networks featuring energy dissipating supramolecular networks and ductile covalent networks have received extensive attention due to their similarity to biological tissues and their outstanding toughness;[29–31] the use of a primary supramolecular network, however, to catalyze the formation of a reinforcing secondary covalent network represents, to our knowledge, a fundamentally new way to generate such materials.

α, ω-azide-terminated PEG (Mn = 2.0 kDa) (**A2**) and tetrakis(prop-2- ynyloxymethyl)methane (**B4**) were included (2:1 ratio of **A2**:**B4**, 13 wt. % of **A2**) during the formation of *c*-Gel as precursors to covalent **A2** + **B4** covalent networks (**Figure 4-4**A). The mixture was annealed into a sheet, which was cut into uniform strips and placed in nitrogen-purged vials (**Figure 4-4**B, i). The strips were then irradiated with 368 nm light for 4 h to achieve switching throughout the sample (**Figure 4-4**B, ii). In contrast to *c*-Gel alone, which converts into a fluid upon switching (**Figure 4-3**D), the

material prepared in the presence of **A2** and **B4** retained its structure hinting at the creation of a new covalent network. UV-vis analysis after irradiation showed complete disappearance of the characteristic 724nm absorbance associated with the Cu(II) paddlewheel complex; re-oxidation by air provided the desired MIN (*min*-Gel, **Figure 4-4**B, iii) with the original blue color and λ_{max} = 724 nm. Notably, the SAXS/WAXS scattering profile (**Figure 4-6**) for *min*-Gel was identical before and after irradiation, indicating that formation of an interpenetrating covalent network does not significantly alter the structure of the polyMOC network (**Figure 4-4**A). Thus, though a new covalent network is formed irreversibly in this process, the polyMOC network is able to reversibly switch between states (e.g., from Cu(I) back to Cu(II)) within the MIN, making it available to catalyze subsequent reactions if desired.

We reasoned that by leveraging the light-induced state-switching properties of *c*-Gel it should be possible to spatiotemporally control MIN fabrication. To demonstrate this concept, a fish-shaped slab (**Figure 4-4**E, i) of *c*-Gel containing **A2** and **B4** was covered by a fish skeleton-shaped photomask (**Figure 4-4**e, ii). After exposure to 368 nm light for 8 h, the Cu(I) functional state could be readily observed in the pattern set by the photomask (**Figure 4-4**E, iii). Re-oxidation provided a fish with a soft polyMOC body and a tough MIN skeleton, the covalent component of which could be isolated by dissolving away the polyMOC component with ethylene diamine (**Figure 4-4**E, iv). Notably, the isolated fish skeleton is composed of a covalent, end-linked PEG network; given the liquid-like nature of the PEG network components this shape could only otherwise be generated using a fish skeleton-shaped mold or complex viscosity modification/processing techniques. Our approach provides a way to utilize the dynamic polyMOC as a scaffold to hold the liquid PEG components in place for subsequent covalent 11 crosslinking. Given that covalent PEG gels of defined shapes are widely used as biomaterials, the approach described here could find broad applications in 3D bioprinting and related fields. Rather than re-oxidizing the material after covalent network formation, further photoreduction using a 365 nm UV LED light source enabled the deposition of Cu(0) in irradiated regions. We reasoned that this phenomenon could provide a novel way to pattern metallic copper onto soft materials. To demonstrate this concept, a 2.1 cm square slab of *c*-Gel containing **A2** and **B4** (**Figure 4-4**F, i) was switched to the Cu(I) state to form a covalent network. A photomask was applied (**Figure**

4-4F, ii) and the sample was exposed to the UV-LED until a metallic pattern was apparent (~2 h, **Figure 4-4**F, iii). Removal of the polyMOC provided a covalent PEG network with a film of Cu(0) in a circuit-shaped pattern embedded on its surface (**Figure 4-4**F, iv). Notably, the resistance of the Cu(0) regions of this material was ~1000-fold lower than in non-irradiated regions. Though this work serves as a proof-of-principle, we believe that with further engineering and optimization the switchability of *c*-Gel could open new avenues for the fabrication of integrated soft-material circuits that could have applications in biometrics, sensing, and soft robotics.

The results provided above represent, to our knowledge, the first examples of a multi-state switchable material capable of catalyzing a self-reinforcing reaction (MIN formation) and deposition of metal on a soft material in response to an external stimulus. Thus, the properties of each state of this material can be leveraged to create a complex object (i.e., a soft circuit board) using a simple apparatus (a UV lamp or LED and a photomask).

4.2.4 Application of *c*-Gel in Direct Ink Writing (DIW) additive manufacturing

Seeking further applications that highlight the synergistic interplay between redox states in the material, we were drawn to using MIN as a template material for DIW additive manufacturing. To fabricate covalently crosslinked networks via DIW 3D printing, gels composed of photocrosslinkable moieties is often employed, such as gelatin methacrylate (GelMA)[32–36], methacrylated hyaluronic acid (MeHA)[37], PEG diacrylate (PEGDA)[38] or composites thereof[39,40]. A post-print irradiation process is required to induce photocrosslinking. These methods tap into materials proven to be suitable towards DIW 3D printing in order to provide a template for the crosslinked network, but are also limited in that the properties of the final material are still influenced by those of the template material, as it is difficult to remove the large biopolymers from which the template is constructed. Template-free printing of crosslinkable soft matter can be achieved only through a more complex 3D printing setup (such as a modified extrusion 3D printer[41], or a resin 3D printer[42]), or printing into a sacrificial template[43,44]; but complexity in hardware in the former case and the challenge of maintaining flow stability in the latter case[43] limits the widespread application of either strategy. An extrudable templating material that can be

subsequently removed has the potential to broaden the scope of materials and properties accessible through DIW additive manufacturing.

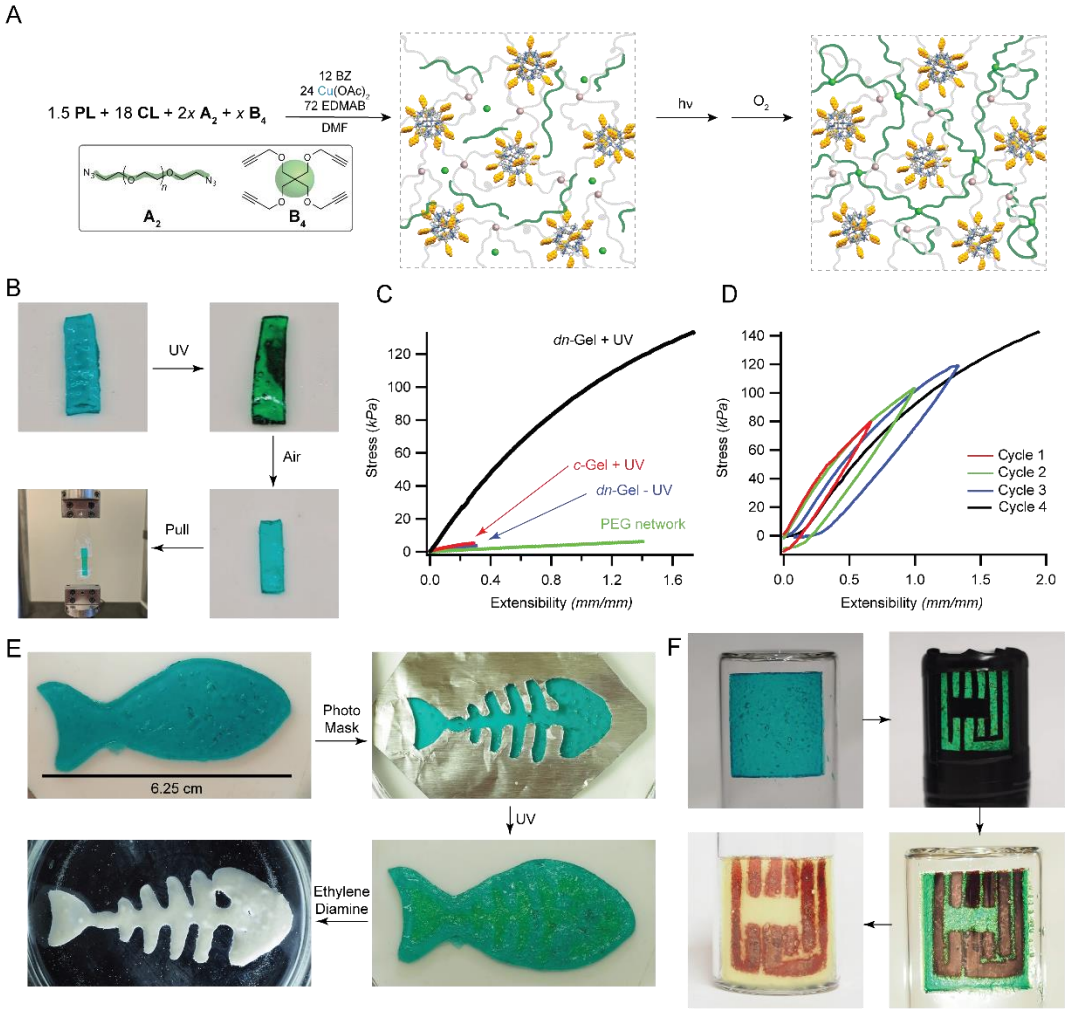

Figure 4-4 Metal-organic cage interpenetrating network (MIN) fabrication enabled by photo-induced switching of *c*-Gel. *a*, Synthesis of *c*-Gel (6.6 wt. %) in the presence of 2 kDa bis-azido-PEG **A2** and tetrakis-alkyne **B4**. Images of the material immediately after annealing (i), after irradiation with UV light to induce the CuAAC reaction (ii), and re-oxidation (iii) to provide a MIN *min*-Gel. In case ii,

some dark regions of Cu(0) were observed, which had no apparent effect on the subsequent MIN formation. *b*, Schematic depiction of the interpenetrating polyMOC and PEG supramolecular and covalent networks, respectively, within *min*-Gel. The covalent PEG network consists of linear strands (green) that can connect two junctions (green spheres) or be connected to the same junction. The latter "primary loop" defects reduce the network connectivity giving rise to double-network-like properties. *c*, Stress-strain plot from tensile testing showing the increased toughness of *min*-Gel compared to control samples. The observed enhancement of toughness is attributed to the IPN effect. *d*, Stress-strain curves showing hysteresis of *min*-Gel over 4 cycles. Strain rate = 1 mm/min; sample length = 5 mm. There was no resting period between cycles. *e*, A fish-shaped sample of *c*-Gel with **A2** and **B4** (i) is covered with an aluminum foil photomask (ii). Irradiation of the sample with a 365 nm UV lamp for 8 h leads to the formation of Cu(I) in irradiated regions (iii). Washing the sample with aqueous ethylene diamine allows for isolation of the newly formed PEG-based covalent network (iv). *f*, A rectangular sample of *c*-Gel (i) was first switched to the Cu(I)state to induce covalent network formation throughout the sample. Then, a photomask in the shape of a circuit was placed over the sample (ii), and the material was irradiated with a 365 nm UV LED to deposit Cu(0) in irradiated regions (iii). Washing the material with aqueous ethylene diamine allowed for isolation of the PEG covalent network with patterned Cu(0) regions (iv). Note: oxidation labels indicate the primary functional oxidation state of the material; they are not intended to imply that 100% of the Cu centers have a given oxidation state.

Given its rapid stress relaxation, we surmised that cGel could be extruded to form filaments that, in the presence of **A2** and **B4** (or any suitable CuAAC reactants), could be converted to MINs of a desired geometry following irradiation. As a proof-of-principle demonstration of this concept, we examined extrusion of *c*-Gel using an inexpensive (~$200) custom-built 3D printer with an attached syringe pump and heating element. *c*-Gel was extruded at a rate of 0.06 cm^3 /s at 60 °C to provide uniform 2 mm diameter filaments (**Figure 4-5**A, i). A multi-layered structure was

created by overlapping filaments of *c*-Gel that fused together over the course of 2h at room temperature (**Figure 4-5**A, ii and 12 iii). Using this approach, a raft-shaped object was printed (**Figure 4-5**B, i), irradiated, and re-oxidized to provide a MIN of the same shape (**Figure 4-5**B, ii). Extraction of the polyMOC provided a raft-shaped covalent PEG gel (**Figure 4-5**B, iii), demonstrating that *c*-Gel can support printing a mixture of **A2** and **B4** monomers and then, upon irradiation, it can catalyze their conversion to a covalent network.

A longstanding challenge in the field of additive manufacturing, particularly of soft gel materials, is the production of overhanging or bridging regions.[37,41,45–47] The state switching capability of *c*-Gel can overcome this challenge. By alternating filaments of *c*-Gel with and without **A2** and **B4** (**Figure 4-5**C), a lattice with several overhangs and bridges was produced (**Figure 4-5**D, i). Photoswitching to the Cu(I) state led to covalent network formation only in the filaments containing **A2** and **B4**. Extraction of the polyMOC components provided a covalent PEG lattice with the overhang and bridging regions preserved (**Figure 4-5**D, ii). This process was repeated with a second lattice featuring fewer overhangs (**Figure 4-5**D, iii and iv). It should be noted that in these examples, (diphenyl(2,4,6-trimethylbenzoyl) phosphine oxide) (TPO) was used as a photoinitiator rather than benzophenone. We found that TPO can be used to access the Cu(I) state of *c*-Gel without further reduction to Cu(0), which allows for the use of excess initiator, reducing the light-induced switching and CuAAC reaction time to as little as 30 min.[48] This rapid CuAAC reaction precluded diffusion of the **A2** and **B4** components across filaments allowing access to well-resolved bridges and overhangs. Despite this advantage for covalent gel patterning, it should be noted that TPO-induced switching was not reversible (i.e., the polyMOC could not be reformed to generate a MIN after TPO-initiated photoreduction). The origin of this difference is the subject of ongoing investigations. Nevertheless, these results demonstrate that the unique state-switching of *c*-Gel can provide facile access to 3D printed gel geometries with overhangs and bridges, thus providing a complementary strategy for soft material and composite additive manufacturing.

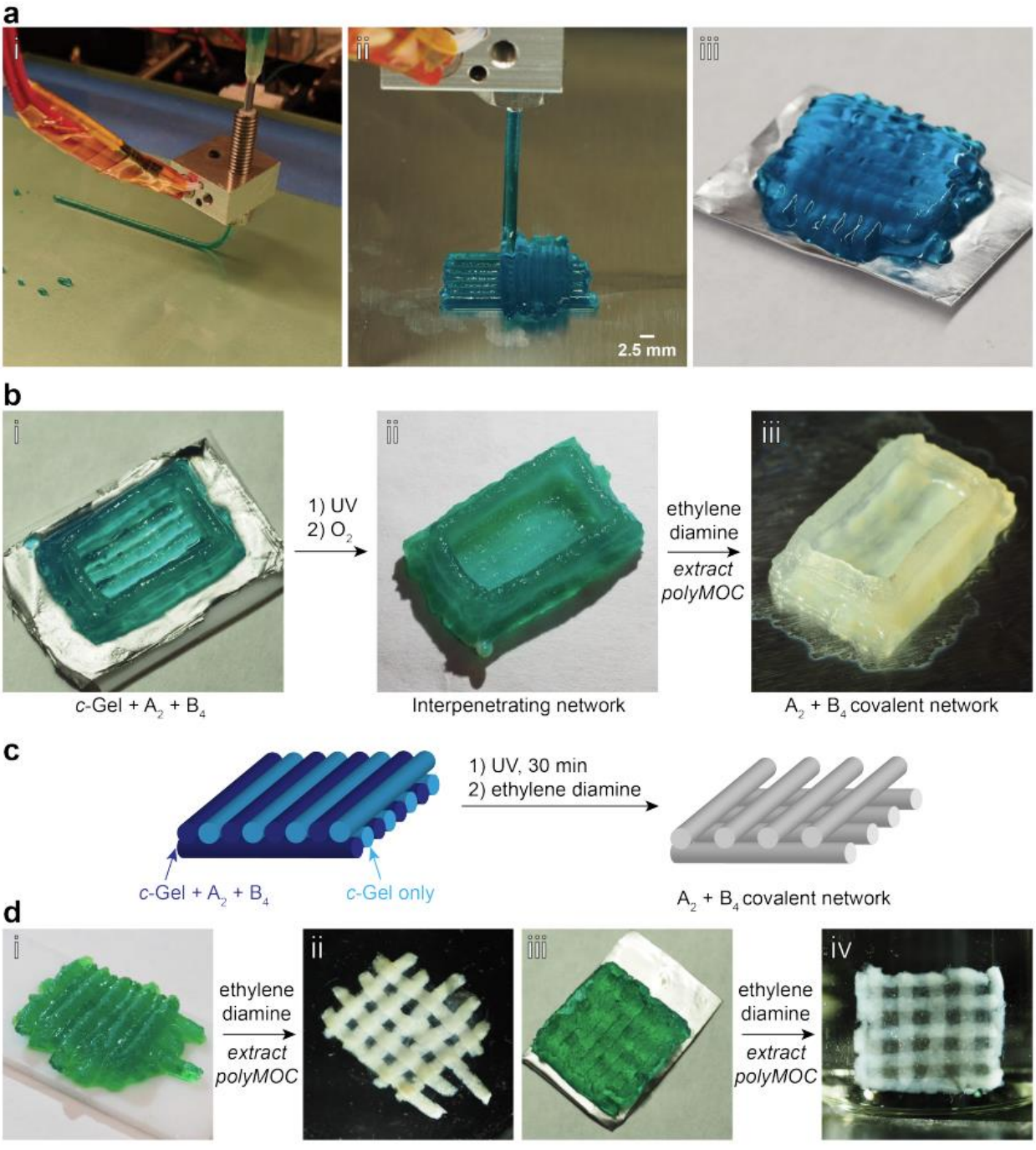

Figure 4-5 *c*-Gel-mediated additive manufacturing. A) *c*-Gel (6.6 wt. %) can be extruded to form a single uniform 2 mm diameter filaments (i and ii). Over the course of hours, the filaments fuse together generating a slab of material (iii). B) By overlaying filaments, *c*-Gel objects containing **A2** and **B4** can be fabricated (i).

Irradiation of the resulting object induces covalent network formation; re-oxidation converts the object into a dimensionally stable *min*-Gel (ii). Then, the polyMOC component of the newly fabricated objected can be removed with aqueous ethylene diamine, yielding an entirely covalent network with the same shape as the printed *c*-Gel (iii). C) Schematic of lattice structures that can be fabricated by alternating *c*-Gel with and without **A2** and **B4** components. D) Images of *c*-Gel lattices before (i and iii) and after (ii and iv) extraction of the polyMOC components. The resulting covalent PEG networks preserve the overhanging and bridging regions of the 3D printed lattice

4.3 Experimental

4.3.1 Rheology

Frequency sweep, amplitude sweep, and stress-relaxation experiments were performed using a TA Instruments Discovery HR-2 rheometer. An 8 mm parallel plate geometry was used to engage the samples. Sample discs were 8 mm in diameter with a thickness of 1.5 mm. Samples were made either using a Teflon mold or a circular punch using a 1.5 mm thick sheet of sample. Amplitude sweeps were performed on newly prepared materials to ensure that the strain % was in the linear viscoelastic regime. Frequency sweep experiments were performed from 0.1 to 100 rad/s at 1% strain. Stress relaxation experiments were carried out at 2% strain. The stress relaxation curves were fitted to a stretched exponential function (see below), to extract the characteristic relaxation time, t, of the material:

$$G(t) = G_0 * e^{\left(\frac{-t}{\tau}\right)^{\alpha}}$$

Experiments were performed at room temperature (25 °C). For samples only containing DMF, solvent loss was assumed to be negligible during measurements that were shorter in duration than 10 min. For longer-term measurements, the samples were covered in mineral oil to reduce evaporation and de-swelling induced by moisture adsorption.

4.3.2 Nuclear magnetic resonance spectroscopy (NMR)

^{1}H NMR spectra were recorded using either a 300 or 500 MHz Varian Inova or a 400 or 600 MHz Bruker AVANCE NMR spectrometer. The instrument used for each individual experiment is indicated below where NMR chemical shifts are listed. The NMR spectra were referenced to the relevant residual solvent peak. Chemical shifts are reported as parts per million (ppm) and splitting patters are designated as follows: s (singlet), d (doublet), t (triplet), q (quadruplet), m (multiplet), and b (broad).

4.3.3 Ultraviolet visible light (UV-vis) spectroscopy

UV-vis spectra were collected using an Implen NP80 nanophotometer using the 0.07 mm path length. The small path length helps avoid excessive scattering by opaque samples and accounts for the fact that gels cannot be diluted. For liquid samples, a drop of liquid was used. For gel samples, a small piece of gel (~1 mm^3) was compressed between the arm and sample window.

4.3.4 Small angle X-ray scattering

SAXS and WAXS experiments were conducted at the Advanced Photon Source (APS) at Argonne National Laboratory (Sector 12-ID-b beamline). 13.3 keV X-rays were used. Silver behenate was used as the standard. An exposure time of 0.5 s was used for all samples. The scattering data were recorded as 2D and converted to 1D plots via radial averaging. The sample to detector distance was 2001.5 mm for SAXS and 414.884 mm for WAXS. The cage-to-cage spacing is calculated from the center of each cage, which is 2π/q. The form factor of a solid spherical particle was used to calculate the radius (R) of the particle:

$$P(q) \propto \frac{[\sin(qR) - qR\cos(qR)]^2}{(qR)^6}$$

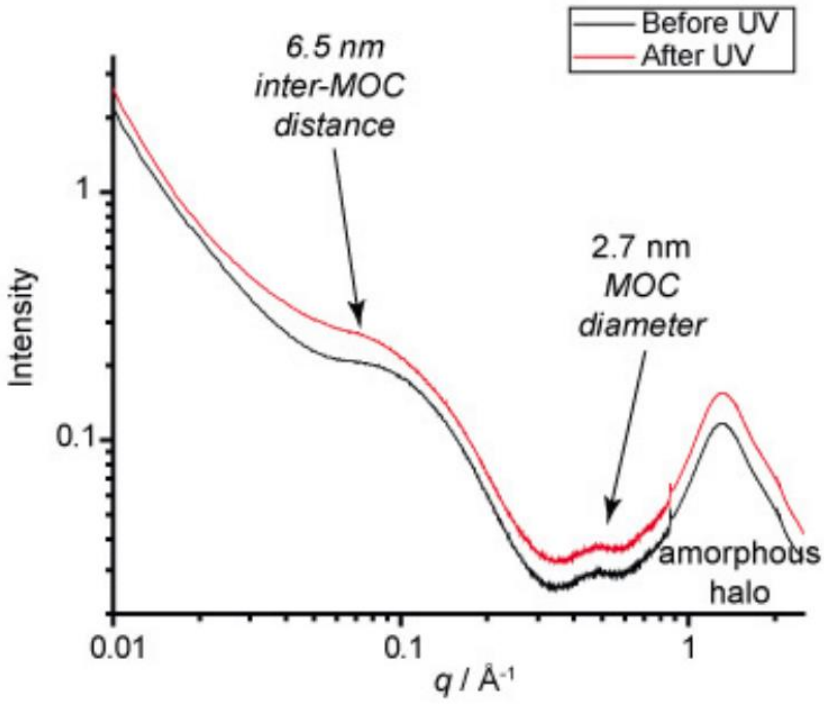

Figure 4-6 SAXS/WAXS profiles of *min*-Gel before and after irradiation (which forms an interpenetrating covalent PEG network) and re-oxidation. The similar profiles indicate that the formation of the covalent PEG network does not disrupt the Cu-polyMOC network.

4.3.5 Preparative gel permeation chromatography (Prep-GPC)

When indicated below, newly synthesized polymers were purified using a Japan Analytical Industry (JAL) Co. LaboACE Recycling Preperative HPLC (LC-5060) employing either JAIGEL-2.5HR (20 mm diameter x 600 mm length) and a JAIGEL-2HR (20 mm diameter x 600 mm length) or JAIGEL-2.5H-40 (40 mm diameter x 600 mm length) and a JAIGEL-2.5H-40 (40 mm diameter x 600 mm length)) columns. Samples were dissolved in $CHCl_3$ and filtered through a 0.2 μm PTFE filter before injection. $CHCl_3$ was used as the eluent.

4.3.6 Materials

Solvents were purchased from Millipore Sigma and were used as received unless otherwise noted. Dry solvents (e.g., DMF) were used when synthesizing $Cu_{24}L_{24}$ polyMOCs. All other chemicals were used as received unless otherwise noted. Isophthalic acid, 5-hydroxy-isophthalic acid, PEG4.6k, PEG20k, potassium carbonate, sodium azide, tosyl chloride, triethylamine, sodium azide, diphenyl(2,4,6-trimethylbenzoyl) phosphine oxide (TPO), ethyl 4-(dimethylamino) benzoate (EDMAB), and 7-hydroxycoumarin were used as purchased from Millipore Sigma. Benzophenone was purchased from Oakwood Chemical. Copper (II) acetate monohydrate was purchased from Strem Chemicals. Deuterated solvents were purchased from Cambridge Isotope Laboratories. Four-arm PEG10k was used as purchased from SINOPEG Inc. 5-((6-((2-oxo-2H-chromen-7-yl) oxy) hexyl) oxy) isophthalic acid (**CL**) and tetrakis(prop-2ynyloxymethyl) methane (**B4**) were synthesized according to literature procedures.

4.3.6.1 Synthesis of *m*-BDC-terminated linear polymer (PLL)

4.3.6.1.1 Bis-tosyl-PEG4.6k

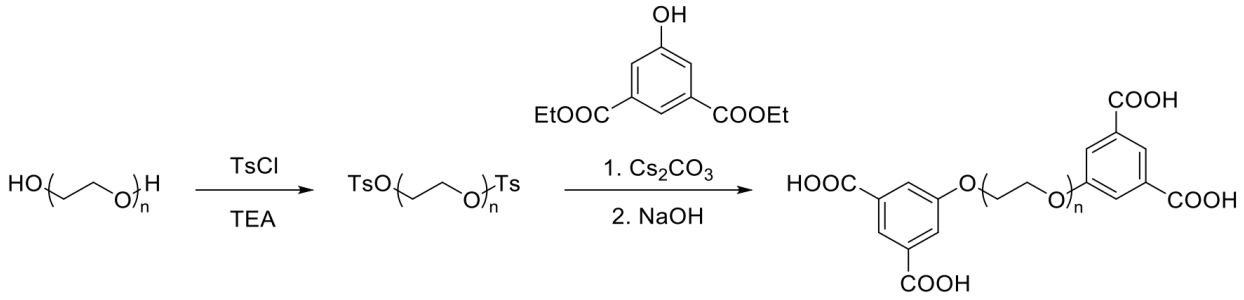

was prepared according to a modified literature procedure. 4 Polyethylene glycol (number-average molecular weight = 4.6 k) (4.6 g, 1.0 mmol, 1 eq) was added to a dry 40 mL vial. The vial was sealed with a septum and placed under a N_2 atmosphere by vacuum/backfilling with N_2 for three times. 15 mL of anhydrous dichloromethane (DCM) was then added via syringe. The mixture was stirred until the PEG was fully dissolved. Next Sure-Seal™ dry triethylamine (682 µL, 4.0 mmol, 5 eq) was added via syringe. Tosyl chloride (760 mg, 4.0 mmol, 4 eq) was added to a separate vial and was placed under a N_2 atmosphere via vacuum/backfilling with N_2 for three times. The tosyl

chloride was dissolved in 5 mL of anhydrous DCM. The resulting solution was added dropwise to the PEG solution. Upon completion of the addition, the reaction was stirred overnight at room temperature. The solution was then diluted with 200 mL of DCM and the organic layer was washed three times with water. The organic layer was then dried with Na_2SO_4, filtered, and the solvent was removed under vacuum yielding 4.1 g of a white solid (83% yield). ^{1}H NMR (500 MHz, CDCl3) δ 7.74 (d, 4H), 7.30 (d, 4H), 4.19 – 4.03 (t, 4H), 3.59 (b), 2.40 (s, 6H).

4.3.6.1.2 Bis-diethyl 5-hydroxyisophthalate-PEG4.6k

Bis-tosyl-PEG4.6k (500 mg, 0.11 mmol, 1.0 eq), Cs_2CO_3 (211 mg, 0.65 mmol, 6.0 eq), and diethyl-5-hydroxyisophthalate (104 mg, 0.44 mmol, 4.0 eq) were added to an oven-dried 40 mL vial. The vial was sealed with a septum and the mixture was placed under a nitrogen atmosphere via vacuum/backfilling with N_2 for three times. 5 mL of anhydrous DMF was added to the mixture via syringe. The vial was then heated to 80 °C in an aluminum-heating block for 24 h. After the reaction was allowed to cool to room temperature, 6 the solution was added dropwise into cold diethyl ether. The resulting white solid precipitate was collected via filtration and washed with additional ether. After the precipitate was dried, it was redissolved in minimal $CHCl_3$ and subjected to purification via dialysis or prep-GPC. 401 mg of a white solid was obtained (74% yield). ^{1}H NMR (600 MHz, CDCl3) δ 8.23 (s, 2H), 7.73 (s, 4H), 4.35 (q, 8H), 4.18 (t, 4H), 3.85 (t, 4H), 3.60 (b), 1.37 (t, 12H).

4.3.6.1.3 PLL

Bis-diethyl 5-hydroxyisophthalate-PEG4.6k (401 mg, 0.08 mmol, 1.0 eq) was dissolved in 10 mL of 1 M NaOH and the solution was stirred for 5 h. The solution was then diluted with 40 mL of 1 M HCl and the aqueous layer was extracted three times with DCM. The organic layers were then combined and dried over Na_2SO_4, filtered, and the solvent was removed *in vacuo*. 341 mg of a white solid was obtained (86% yield). ^{1}H NMR (600 MHz, $CDCl_3$) δ 8.32 (s, 2H), 7.80 (d, 4H), 4.23 (t, 4H), 3.89 (d, 4H), 3.64 (b).

4.3.6.2 Synthesis of PL

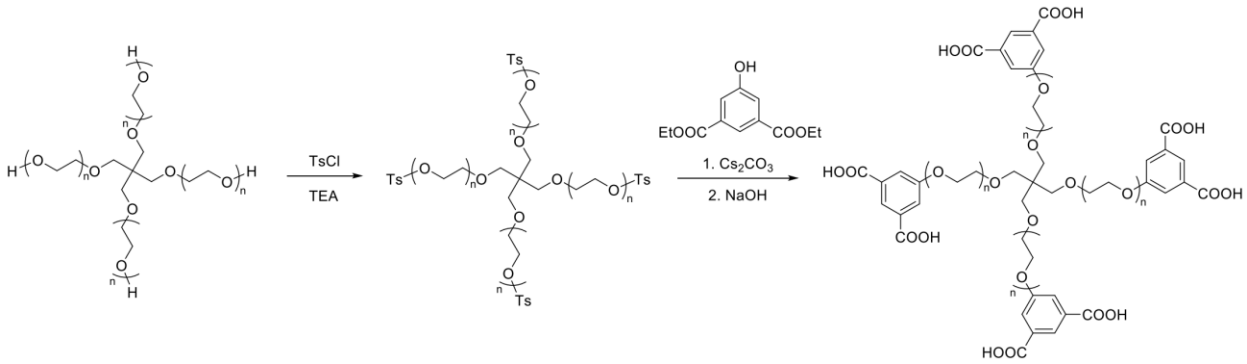

4.3.6.2.1 Tetra-Tosyl-PEG10k

Four-arm polyethylene glycol (number-average molecular weight = 10 k) (1.0 g, 0.1 mmol, 1 eq) was added to a dry 20 mL vial. The vial was sealed with a septum and placed under a nitrogen atmosphere by vacuum/backfilling with N_2 for three times. 5 mL of anhydrous DCM was then added via syringe. The mixture was stirred until the PEG was fully dissolved. Next dry triethylamine (138 μL, 1.5 mmol, 15 eq) was added to the PEG solution via syringe. Tosyl chloride (190 mg, 1.0 mmol, 10 eq) was added to a separate vial and placed under a N_2 atmosphere via vacuum/backfilling with N_2 for three times. 2.5 mL of anhydrous DCM was added and the resulting tosyl chloride solution was added dropwise via syringe to the PEG solution. After the addition, the reaction mixture was stirred overnight at room temperature. The mixture was then added dropwise into cold diethyl ether to provide a white precipitate that was filtered and washed with additional diethyl ether. 850 mg of a white solid was obtained. It should be noted that though complete conversion to the product was observed by ^{1}H NMR, some tosyl chloride and triethylamine salts remained in the sample. Regardless, the material was used in the next step without further purification. ^{1}H NMR (500 MHz, CDCl3) δ 7.78 (d, 8H), 7.34 (d, 8H), 4.14 (t, H), 4.01 – 3.44 (b), 3.40 (s, 8H), 2.44 (s, 12H).

4.3.6.2.2 Tetra-diethyl 5-hydroxyisophthalate-PEG10k

Tetra-tosyl-PEG10k (850 mg, 0.08 mmol, 1.0 eq), Cs_2CO_3 (390 mg, 1.2 mmol, 15.0 eq), and diethyl-5-hydroxyisophthalate (228 mg, 0.96 mmol, 10.0 eq) were placed in an oven-dried 40 mL

vial. The vial was sealed with a septum and the mixture was placed under a N_2 atmosphere via vacuum/backfilling with N_2 for three times. 5 mL of anhydrous DMF were added via syringe. The vial was then heated to 80 °C in an aluminum-heating block for 24 h. The reaction mixture was allowed to cool to room temperature. Afterward, the mixture was added dropwise into cold diethyl ether providing the product as a white precipitate. The precipitate was filtered and washed with additional diethyl ether. After drying, the precipitate was redissolved in minimal $CHCl_3$ and subjected to purification via prep-GPC. 540 mg of a white solid was obtained (62% yield). ^{1}H NMR (500 MHz, CDCl3) δ 8.27 (s, 4H), 7.76 (d, 8H), 4.39 (q, 16H), 4.21 (t, 8H), 3.88 (t, 8H), 3.63 (b), 3.40 (s, 8H), 1.40 (t, 24H).

4.3.6.2.3 PL

Bis-diethyl 5-hydroxyisophthalate-PEG4.6k (540 mg, 0.05 mmol, 1.0 eq) was dissolved in 10 mL of 1 M NaOH and the resulting solution was stirred at room temperature for 5 h. The solution was then diluted with 40 mL of 1 M HCl and the aqueous layer was extracted three times with DCM. The organic layers were then combined and dried over Na_2SO_4, filtered, and the solvent was removed in vacuo. 440 mg of a white solid was obtained (83% yield). ^{1}H NMR (400 MHz, CDCl3) δ 8.32 (s, 4H), 7.80 (d, 8H), 4.23 (t, 8H), 3.89 (t, 8H), 3.64 (b), 3.41 (s, 8H).

4.3.6.3 Preparation of Bis-azido-PEG2k (A2)

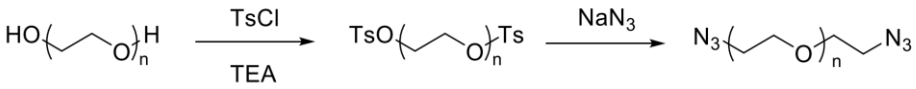

4.3.6.3.1 Bis-tosyl-PEG2k

Polyethylene glycol (number-average molecular weight = 2.0 k) (2.0 g, 1.0 mmol, 1 eq) was added to a dry 40 mL vial. The vial was sealed with a septum and placed under a nitrogen atmosphere by vacuum/backfilling with N_2 for three times. 15 mL of anhydrous DCM was then added via syringe. The mixture was stirred until the PEG was completely dissolved. Next, 682 µL (4.0 mmol, 5 eq) of dry triethylamine was added via syringe. Tosyl chloride (760 mg, 4.0 mmol, 4 eq) was added to

a separate vial and placed under a N_2 atmosphere via vacuum/backfilling with N_2 for three times. The tosyl chloride was then dissolved in 5 mL of anhydrous DCM and the solution was added dropwise via syringe to the PEG solution. After the addition, the reaction was stirred overnight at room temperature. Then, the solution was diluted with 200 mL of DCM and the organic layer was washed three times with water. The organic layer was then dried over Na_2SO_4, filtered, and the solvent was removed under vacuum. 1.8 g of a white powder was obtained. The crude product was used directly in the next reaction (Note: ^{1}H NMR analysis of the crude material indicated complete conversion to the desired tosylate).

4.3.6.3.2 Bis-azide-PEG2k

Bis-tosyl-PEG2k (1.8 g, 0.9 mmol, 1.0 eq) was added to a 20 mL vial and dissolved in 5 mL of anhydrous DMF. NaN3 was added (260 mg, 4.0 mmol, 4.44 eq) and the reaction was stirred for 24 h. After 24 h, the reaction was diluted with 100 mL of ethyl acetate and the resulting mixture was washed five times with water. The organic layer was dried over Na_2SO_4, filtered, and concentrated to 10 mL volume. The oily liquid was then precipitated into cold diethyl ether, filtered, and washed with more diethyl ether providing a white powder in 91% yield. ^{1}H NMR (600 MHz, $CDCl_3$) δ 3.64 (b), 3.39 (t, 4H).

4.3.7 Preparation of *c*-Gel with benzophenone and ethyl 4-(dimethylamino)benzoate (EDMAB)

Samples of *c*-Gel were prepared using 6.6 wt % of polymer. **PL** (20 mg, 1.9 μmol, 1.0 eq) **CL** (9.6 mg, 22.5 μmol, 12 eq), ethyl 4-(dimethylamino) benzoate (17.4 mg, 0.090 mmol, 48 eq) and benzophenone (2.7 mg, 15.0 μmol, 8.0 eq) were dissolved in 150 μL of DMF. Separately, Cu(OAc)2•H2O (5.74 mg, 14.4 μmol, 16.0 eq) was dissolved in 150 μL of DMF with some heating. The copper acetate solution was then added to the polymer and ligand solution. The gelled mixture was stirred with a spatula until the blue color was homogenous. The vial was then briefly centrifuged to force all of the material to the bottom of the vial. The vial was then capped and heated to 60 °C for 4 h providing a blue gel.

4.3.8 Preparation of *c*-Gel for 3D printing/extrusion experiments

PL (66.0 mg, 6.3 μmol, 1.0 eq) **CL** (32.1 mg, 75 μmol, 12 eq), ethyl 4- (dimethylamino)benzoate (58.1 mg, 0.30 mmol, 48 eq) and benzophenone (9.1 mg, 50 μmol, 8.0 eq) were dissolved in 500 μL of DMF with slight heating. Separately, Cu(OAc)2•H2O (20.0 mg, 100 μmol, 16.0 eq) was dissolved in 500 μL of DMF with some heating. The copper solution was then added to the polymer and ligand solution. The gelled mixture was stirred with a spatula until the blue color was homogenous. The vial was then heated to 60 °C for 15 minutes. Using a spatula, the gel was then transferred into the top of a 1 mL Norm-Ject syringe with the plunger removed. The bottom of the syringe was capped with a septum and the material was lightly 9 centrifuged to force the gel to the bottom of the syringe. The plunger was replaced and the gel was allowed to anneal overnight at room temperature.

4.3.9 Preparation of *min*-Gel

PL (16.7 mg, 1.6 μmol, 1.0 eq) **CL** (8.0 mg, 19 μmol, 12 eq) benzophenone (2.3 mg, 12.5 μmol, 8.0 eq), ethyl 4-(dimethlyamino) benzoate (16.5 mg, 86 μmol, 48 eq), bisazide-PEG2k (33.5 mg, 16.7 μmol, 10.7 eq), and tetrakis(prop-2ynyloxymethyl) methane (2.4 mg, 8.4 μmol, 5.4 eq) were dissolved in 125 μL of DMF with some slight heating. Separately, $Cu(OAc)_2•H_2O$ (5.0 mg, 25.1 μmol, 16.0 eq) was dissolved in 125 μL of DMF with some heating. The copper acetate solution was added to the polymer solution and the gelled mixture was stirred with a spatula until the blue color was homogenous. The gel was then placed in a Teflon mold, sealed with binder clips, and allowed to anneal at room temperature for at least 6 h. For larger molds this recipe was linearly scaled as needed.

4.3.10 Photoreduction of *c*-Gel

0.3 mL of *c*-Gel was prepared in a glass vial, which was sealed with a cap that had a septum. The vial was purged with N_2 for 10 min. Then, the sample was exposed to irradiation from a benchtop UV lamp (Sankyo DENKT Blacklight blue, FL8BLB-368 8W Bulb, 368 nm light) at a distance of 25 cm. The sample was irradiated for a total of 4 h. After 1h, the sample (which was a mixture of green liquid and blue gel) was briefly vortexed and before irradiation for an additional hour. A

clear green liquid was obtained (the Cu(I) state). After UV irradiation for an additional 2 h, the green Cu(I) state converted to a brown liquid (the Cu(0) state). Notably, we observed that clean switching from Cu(II) to Cu(I) was only possible using a (sub)stoichiometric amounts of copper acetate. When excess copper acetate is present, its rapid reduction to Cu(0) is observed, which attests to the need for assembled $Cu_{24}L_{24}$ MOCs possessing coumarin-base ligands to avoid over-reduction.

4.3.11 Photocrosslinking of *c*-Gel to form *min*-Gel

A strip of *c*-Gel (2 cm long, 0.5 cm wide, and 0.12 cm thick) containing **A2** and **B4** was placed against the wall of a glass vial. The vial was purged with N_2 for 10 min. The vial was then irradiated until the sample was green (generally < 8 h) at a distance of 25 cm from a UV lamp (368 nm). When using a photomask, the sample was placed on a piece of Teflon in a plastic petri dish and the aluminum foil photo mask was carefully placed on top. The petri dish was sealed with Teflon tape and electrical tape. The dish was purged by carefully poking a hole in the top with a needle and introducing N_2 for 20 minutes. Then, the sample was irradiated with 368 nm UV light at a 10 distance of 25 cm away for the desired amount of time, (generally < 8 h until the pattern could clearly be seen). After irradiation, the sample was exposed to air.

4.3.12 Removal of polyMOC network from MOC-interpenetrating network (*min*-Gel) material

min-Gel was placed in a vial, which was then filled with 10% aqueous ethylene diamine solution. The vial was gently stirred on a plate shaker for 30 min. The solution becomes blue and slightly cloudy during this process while the sample becomes white. This procedure was repeated for three times. After the third wash, the material was washed three times with dimethylacetamide (DMA). The resulting clear gel was the covalent PEG network created through the photoreduction-induced CuAAC reaction. This gel was then tested via uniaxial tensile testing. The gel was allowed to dry until it was roughly the same weight as the other samples (accounting for the removal of the c-Gel network) to ensure a similar wt % polymer.

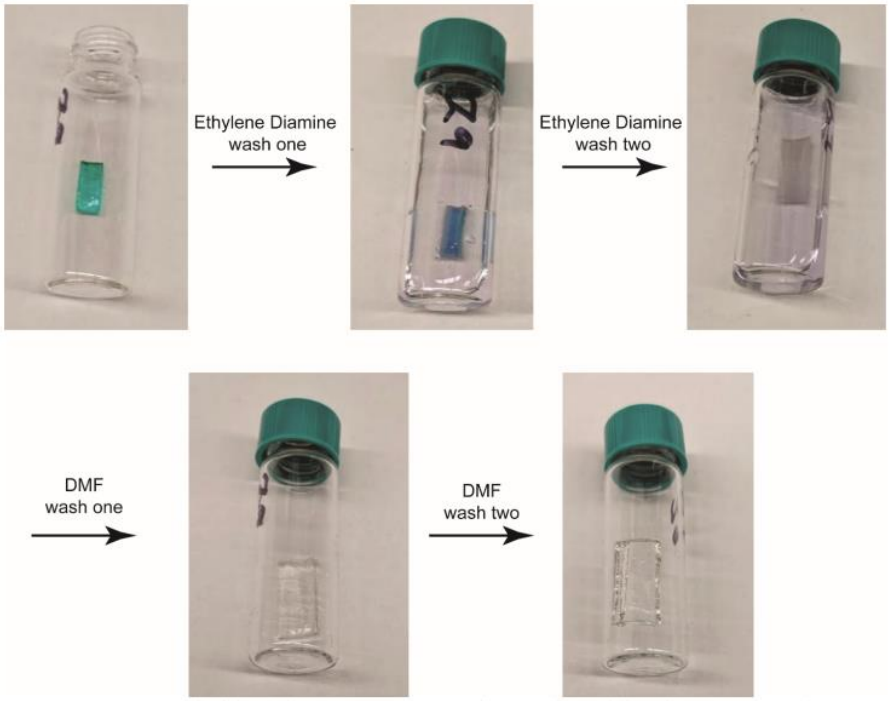

Figure 4-7 Removal of the polyMOC component of min-Gel providing the **A2** + **B4** covalent PEG network.

4.3.13 Photo patterning Cu(0)

A slab of *c*-Gel (square, 2.1 cm side, and 0.12 cm thick) containing **A2** and **B4** was placed against the wall of a 20 mL glass vial against the wall. The vial threads were lined with Teflon and sealed with a cap with a septum. The vial was then purged with N_2 for 20 min. After this time, the cap and the septum were sealed with electrical tape. Care was taken to avoid the introduction of air as the Cu(0) layer formed was observed to be quite thin and it can be readily oxidized. The gel was 14 then exposed to the UV lamp at a distance of 25 cm for 20 MΩ) for the background polymer with no Cu(0) patterned. The deposited copper layer is thin, so care must be taken to ensure the sample is handled carefully as to not break the copper layer. Non-zero resistance is thought to be from the discontinuity (i.e., breaks) in the copper layer, the insulating nature of the polymer backing, as well as the very thin nature of the Cu(0) layer.

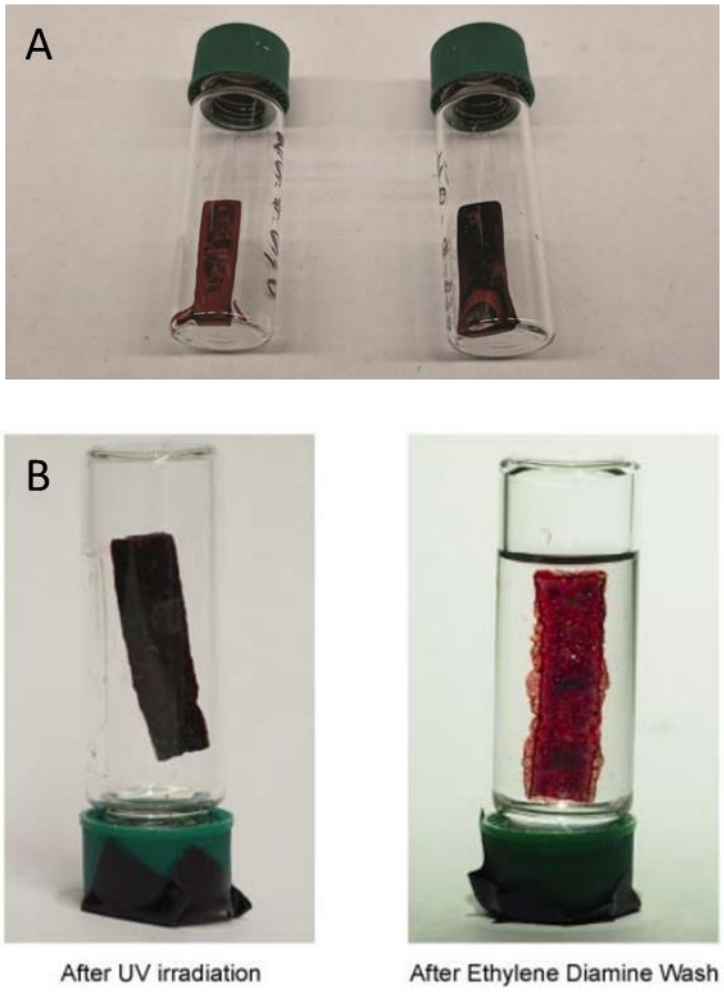

Figure 4-8 *a*. Image of *min*-Gels after 30 min of UV irradiation with a UV-LED source. The presence of Cu(0) is readily observed. *b*. *min*-Gel sample which has been irradiated to deposit Cu(0) onto the surface. The sample was then washed with 2:9:9 ethylene diamine:water:methanol until no more blue color was observed (~2 h).

4.3.14 3D printing

3D printing studies were conducted using a modified Anet A8 3D printer. The extruder carriage was removed and replaced with a 3D printed one (www.thingiverse.com/thing:2514659) onto which a customized 3D printed syringe pump was attached. The extruder motor was used to drive

the syringe pump. An Air-Tite 14-gauge needle was cut to 3 cm long, and the tip was smoothed with a stone. The extruder nozzle was removed from the heating block and the needle was inserted into the heater throat. The Z-Endstop was moved to the top of the Z axis to accommodate the extra height of the syringe pump. No change was made to the wiring. The Marlin 1.1 firmware was modified to accommodate for the physical changes and was uploaded to the printer board (Follow these instructions when flashing firmware for the first time on the Anet board: www.instructables.com/id/HOW-TO-FIX-ANET-BRICKED-BOARD-USING-AN-ARDUINO-UNO/; with Marlin running on the board, it can be re-flashed by connecting to the computer via USB). The Repetier-Host software was used to control the printer. A Norm-Ject 1mL syringe loaded with the gel was attached on the syringe pump and 3D printing was achieved by running a hand-written G-code. The gel was extruded at 60 °C at a rate 15 of 0.001 mL/s. This extrusion rate was calculated based on the minimum travel speed of the 3D printer, which is 0.3mm/s.

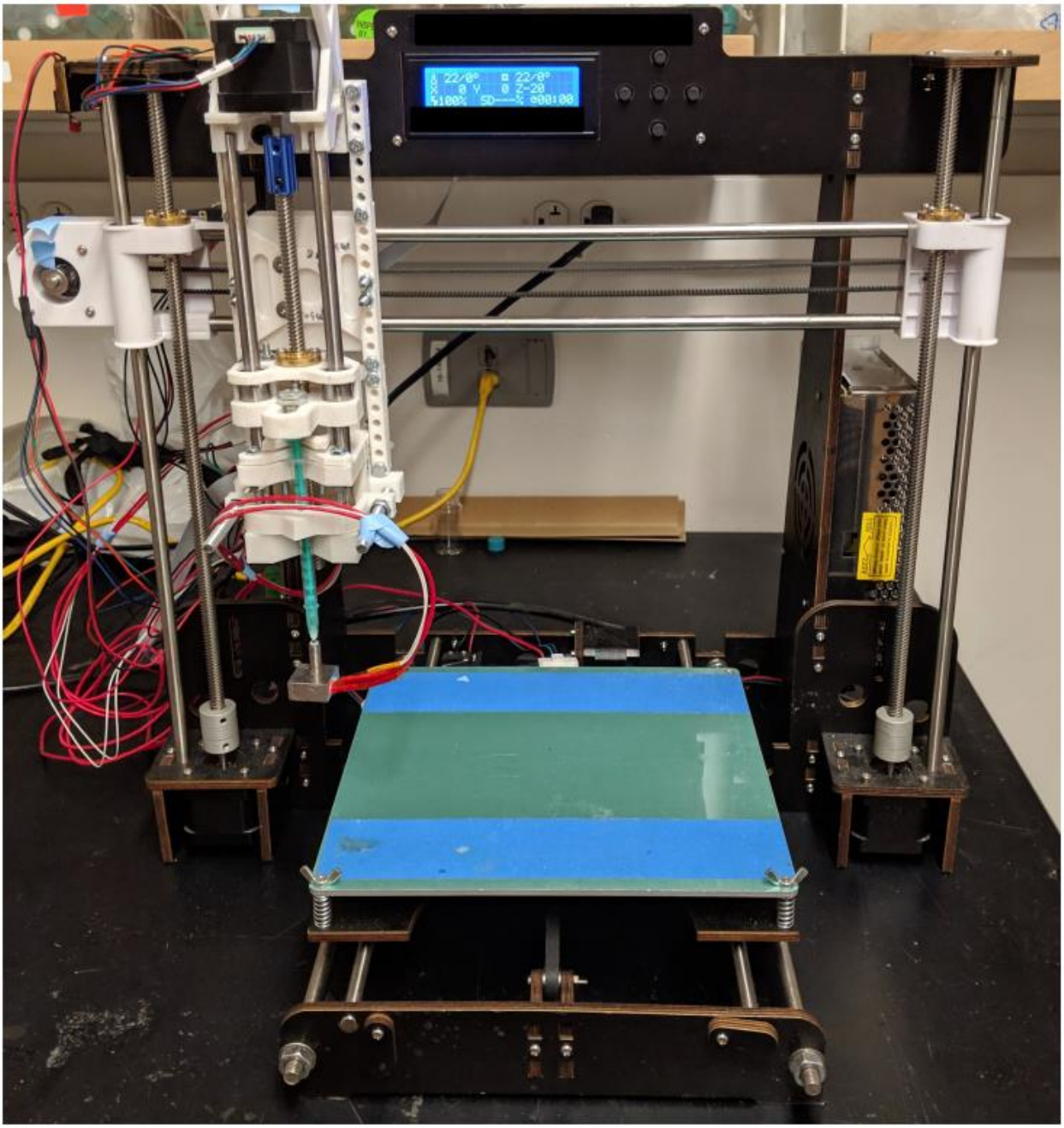

Figure 4-9 Image of the custom-built 3D printer used to extrude the gels

4.4 Supplement

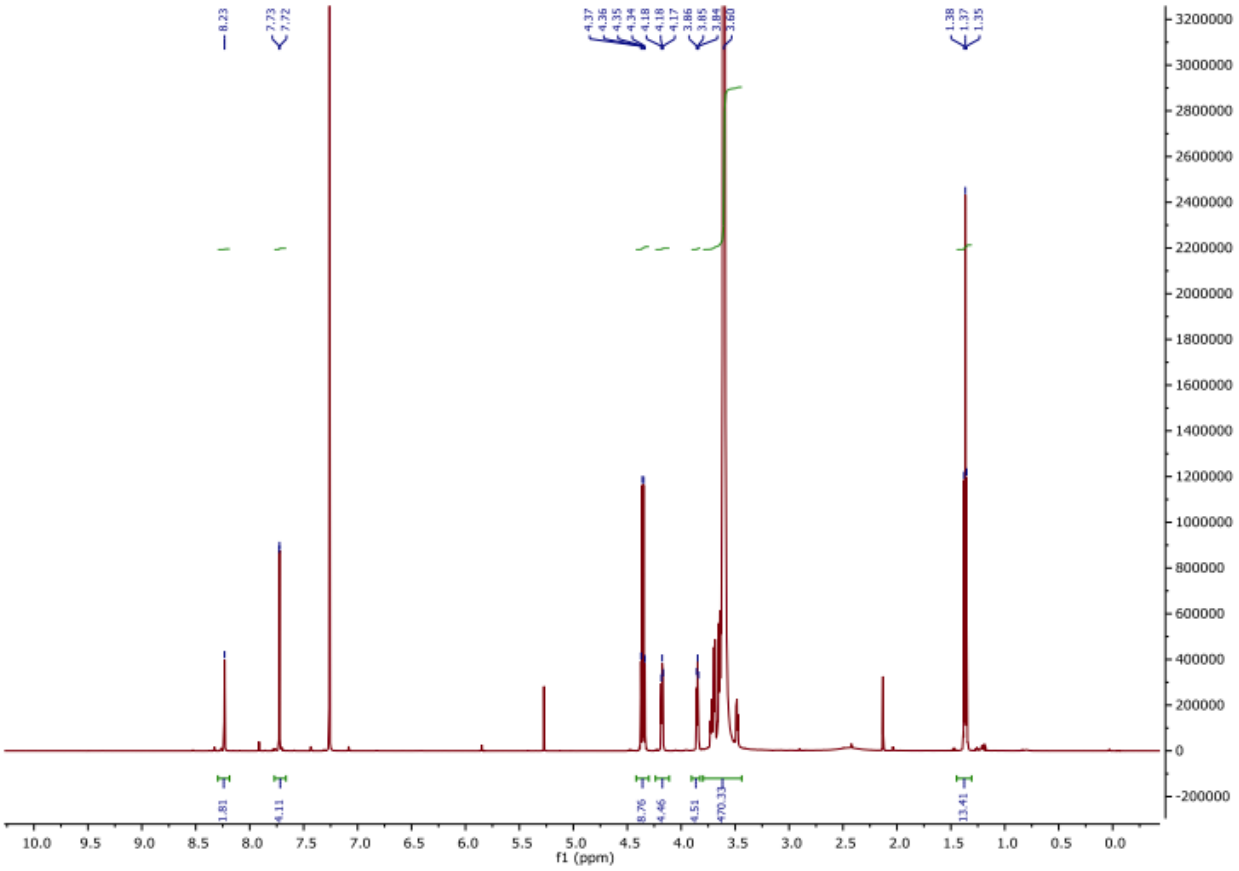

Figure 4-10 ^{1}H NMR ($CDCl_3$, 600 MHz) spectrum of bis-diethyl 5-hydroxyisophthalate-PEG4.6k.

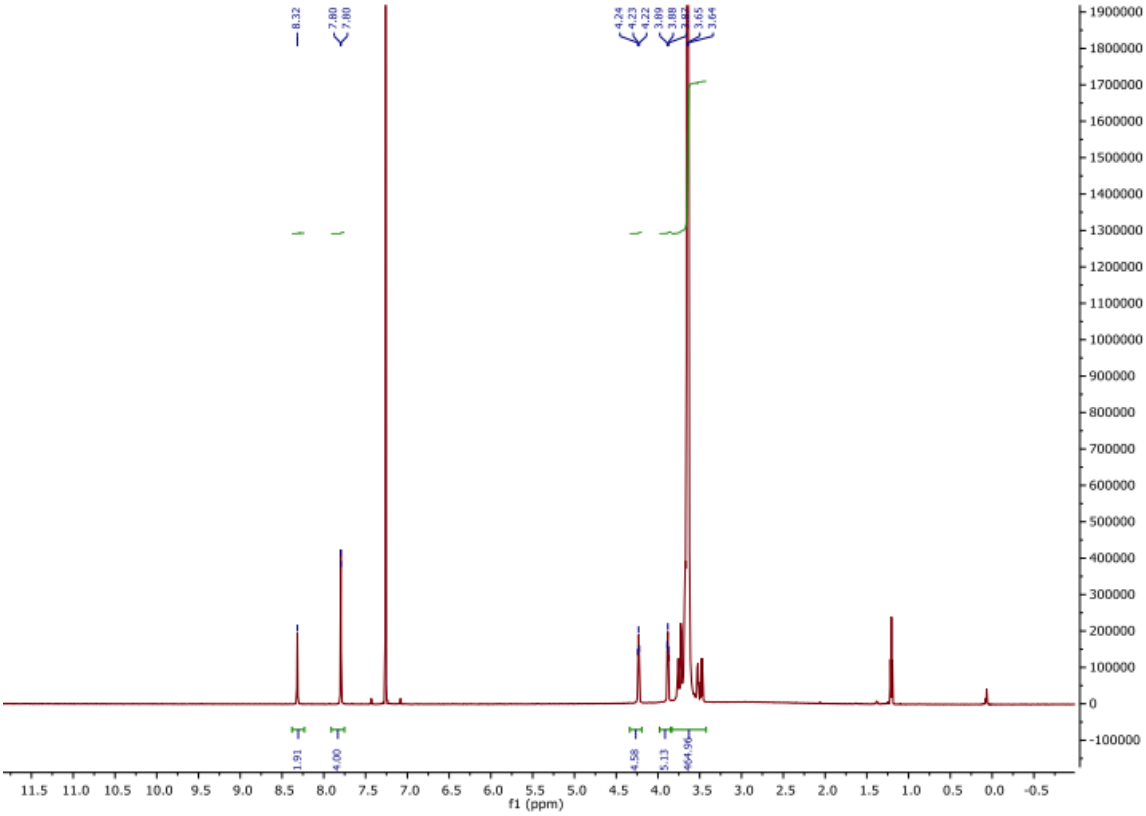

Figure 4-11 ^{1}H NMR ($CDCl_3$, 600 MHz) spectrum of bis-*m*-BCD-PEG4.6k (**PLL**)

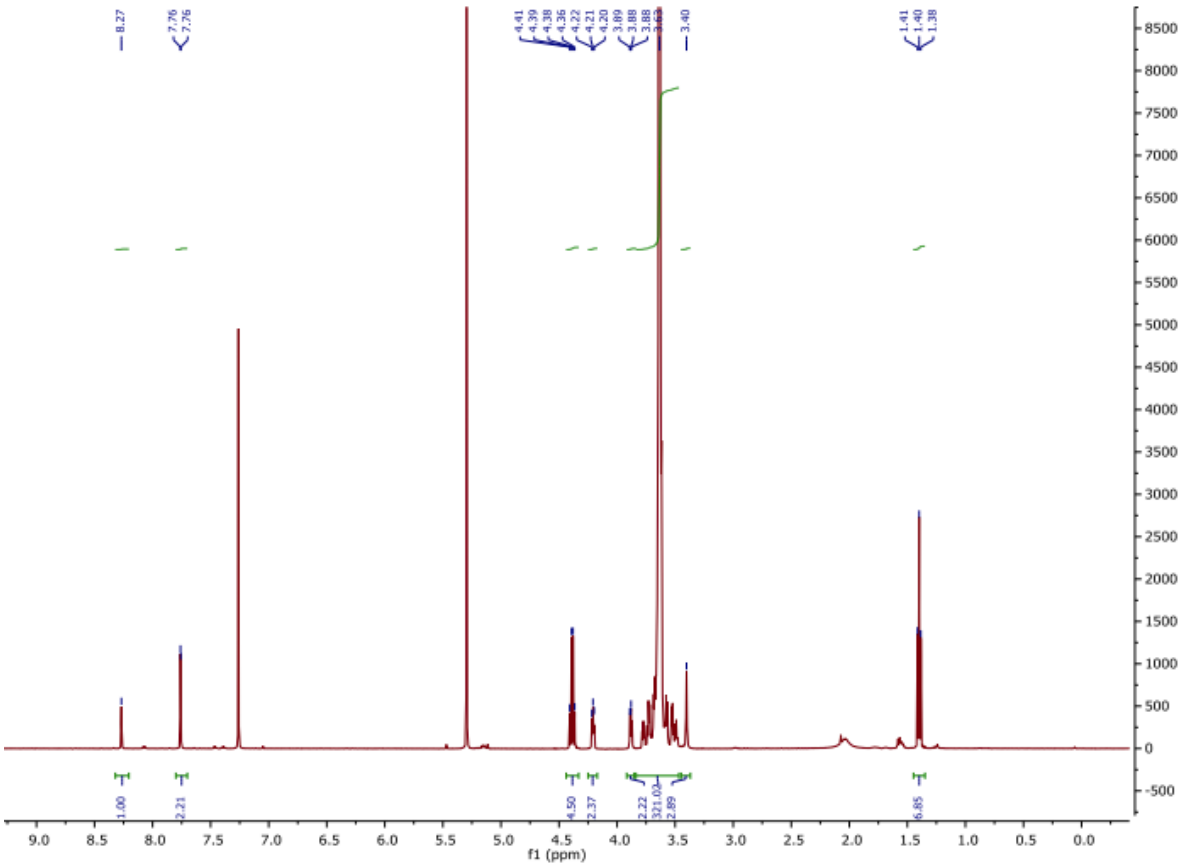

Figure 4-12 ^{1}H NMR ($CDCl_3$, 500 MHz) spectrum of tetra-diethyl 5-hydroxyisophthalate PEG10k.

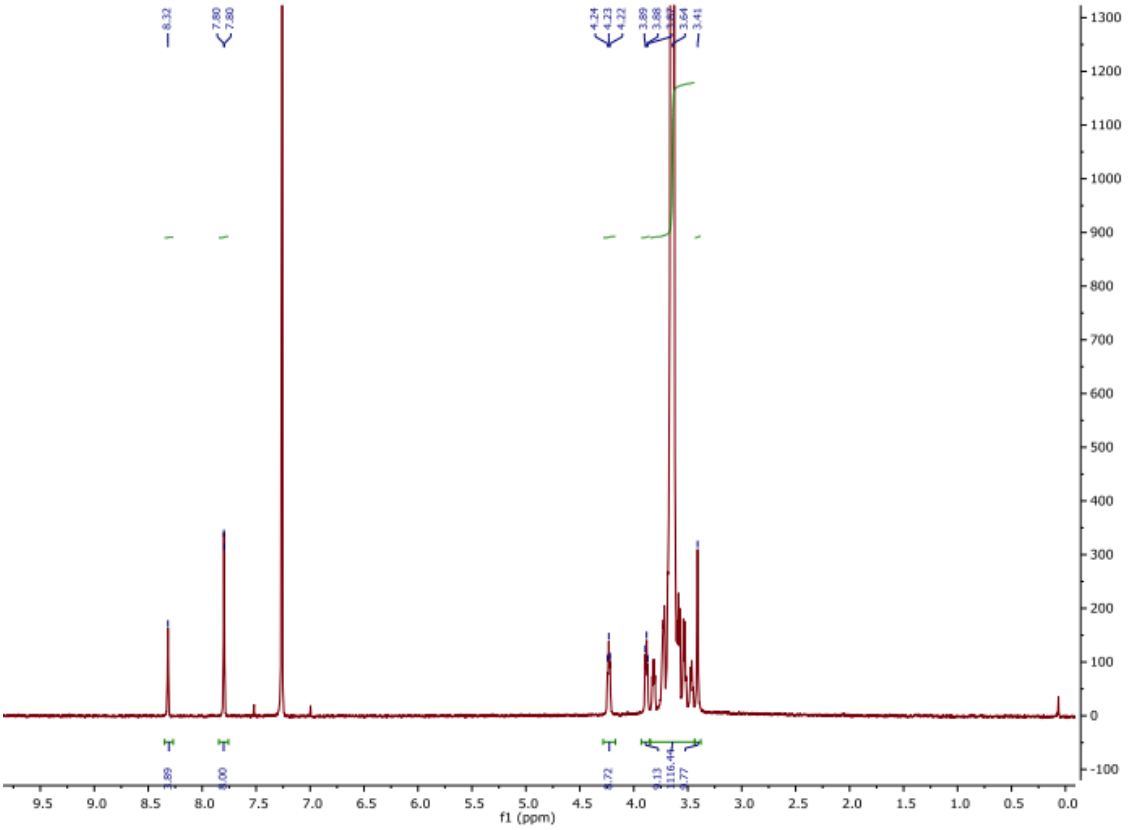

Figure 4-13 ^{1}H NMR ($CDCl_3$, 400 MHz) spectrum of tetra-*m*-BCD-PEG10k (**PL**)

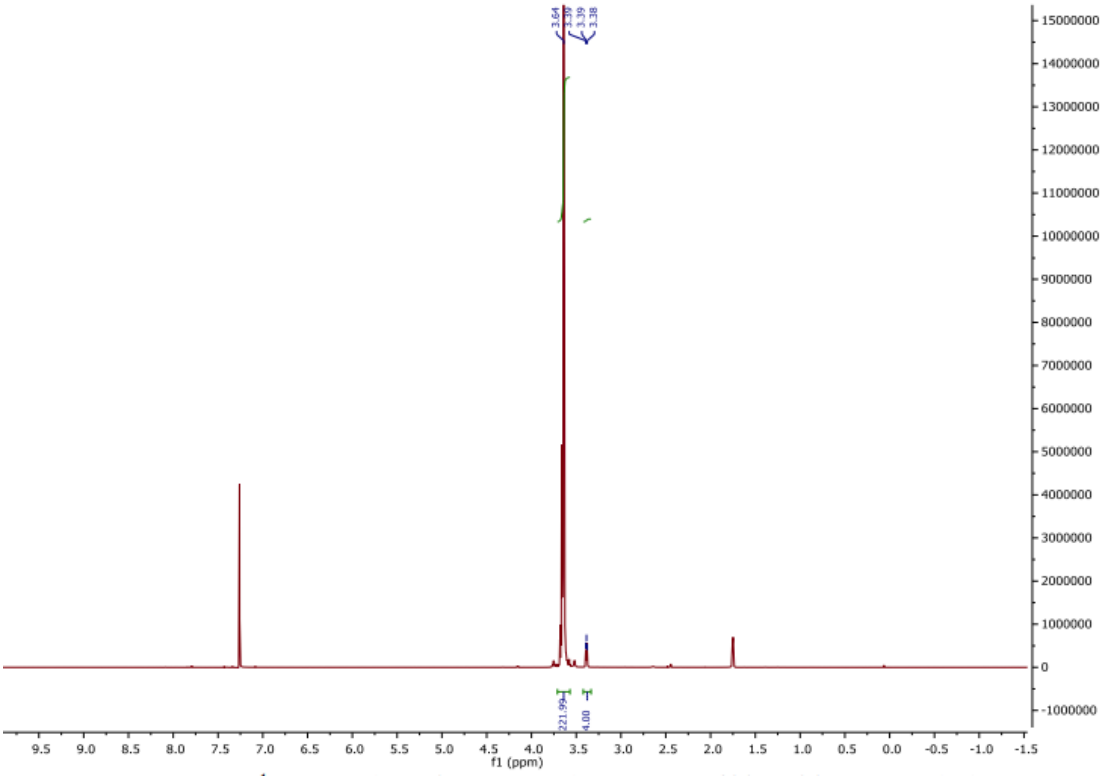

Figure 4-14 ^{1}H NMR (CDCl3, 600 MHz) spectrum of bis-azide-PEG4.6k (**A2**)

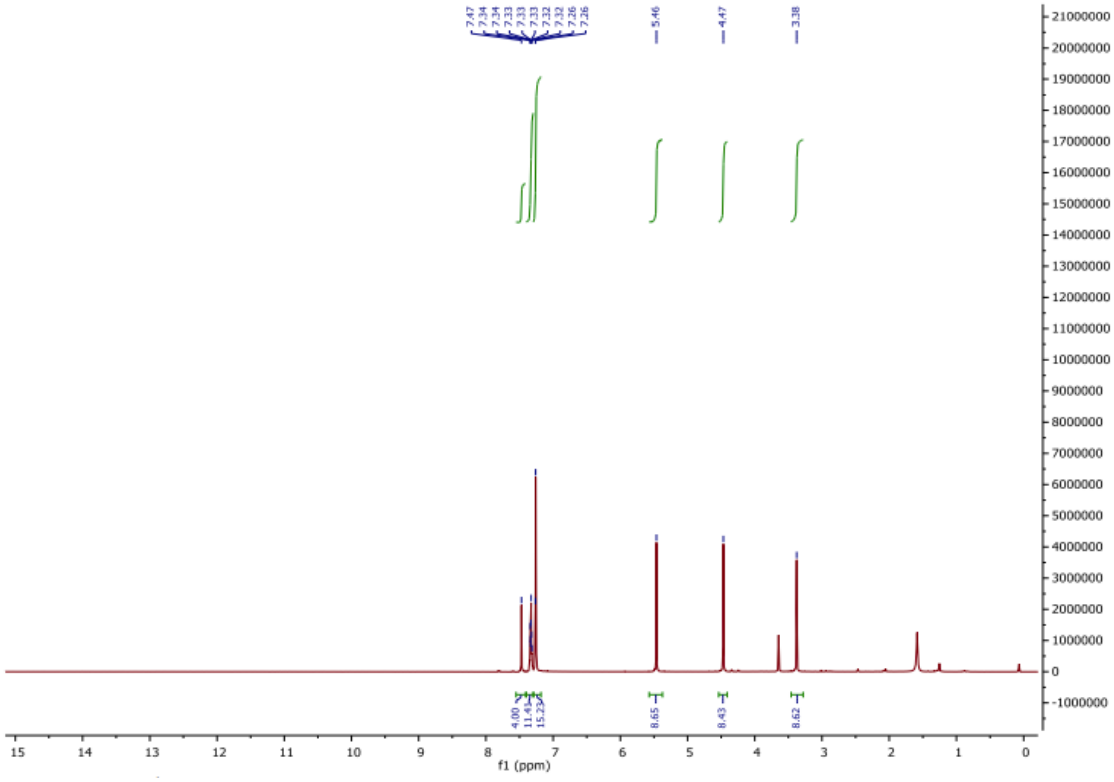

Figure 4-15 ^{1}H NMR ($CDCl_3$, 600 MHz) spectrum of 4,4'-(((2,2-bis(((1-benzyl-1H-1,2,3-triazol-4-yl)methoxy)methyl)propane-1,3-diyl)bis(oxy))bis(methylene))bis(1-benzyl-1H-1,2,3-triazole

References

(1) Wojtecki, R. J.; Meador, M. A.; Rowan, S. J. Using the Dynamic Bond to Access Macroscopically Responsive Structurally Dynamic Polymers. *Nat. Mater. 2011 101* **2010**, *10* (1), 14–27. https://doi.org/10.1038/nmat2891.

(2) Yan, X.; Wang, F.; Zheng, B.; Huang, F. Stimuli-Responsive Supramolecular Polymeric Materials. *Chem. Soc. Rev.* **2012**, *41* (18), 6042–6065. https://doi.org/10.1039/C2CS35091B.

(3) Datta, S.; Saha, M. L.; Stang, P. J. Hierarchical Assemblies of Supramolecular Coordination Complexes. *Acc. Chem. Res.* **2018**, *51* (9), 2047–2063. https://doi.org/10.1021/ACS.ACCOUNTS.8B00233.

(4) Li, M.; Chen, L. J.; Cai, Y.; Luo, Q.; Li, W.; Yang, H. B.; Tian, H.; Zhu, W. H. Light-Driven Chiral Switching of Supramolecular Metallacycles with Photoreversibility. *Chem* **2019**, *5* (3), 634–648. https://doi.org/10.1016/J.CHEMPR.2018.12.006.

(5) Ji, X.; Yao, Y.; Li, J.; Yan, X.; Huang, F. A Supramolecular Cross-Linked Conjugated Polymer Network for Multiple Fluorescent Sensing. *J. Am. Chem. Soc.* **2013**, *135* (1), 74–77. https://doi.org/10.1021/ja3108559.

(6) Ogden, W. A.; Guan, Z. Recyclable, Strong, and Highly Malleable Thermosets Based on Boroxine Networks. *J. Am. Chem. Soc.* **2018**, *140* (20), 6217–6220. https://doi.org/10.1021/jacs.8b03257.

(7) Accardo, J. V.; Kalow, J. A. Reversibly Tuning Hydrogel Stiffness through Photocontrolled Dynamic Covalent Crosslinks. *Chem. Sci.* **2018**, *9* (27), 5987–5993. https://doi.org/10.1039/C8SC02093K.

(8) Gu, Y.; Zhao, J.; Johnson, J. A. Polymer Networks: From Plastics and Gels to Porous Frameworks. *Angew. Chemie Int. Ed.* **2020**, *59* (13), 5022–5049. https://doi.org/10.1002/anie.201902900.

(9) Stuart, M. A. C.; Huck, W. T. S.; Genzer, J.; Müller, M.; Ober, C.; Stamm, M.; Sukhorukov, G. B.; Szleifer, I.; Tsukruk, V. V.; Urban, M.; Winnik, F.; Zauscher, S.; Luzinov, I.; Minko, S. Emerging Applications of Stimuli-Responsive Polymer Materials. *Nat. Mater. 2010 92* **2010**, *9* (2), 101–113. https://doi.org/10.1038/nmat2614.

(10) Li, L.; Scheiger, J. M.; Levkin, P. A.; Li, L.; Scheiger, J. M.; Levkin, P. A. Design and Applications of Photoresponsive Hydrogels. *Adv. Mater.* **2019**, *31* (26), 1807333. https://doi.org/10.1002/ADMA.201807333.

(11) Worrell, B. T.; McBride, M. K.; Lyon, G. B.; Cox, L. M.; Wang, C.; Mavila, S.; Lim, C. H.; Coley, H. M.; Musgrave, C. B.; Ding, Y.; Bowman, C. N. Bistable and Photoswitchable States of Matter. *Nat. Commun. 2018 91* **2018**, *9* (1), 1–7. https://doi.org/10.1038/s41467-018-05300-7.

(12) Fiore, G. L.; Rowan, S. J.; Weder, C. Optically Healable Polymers. *Chem. Soc. Rev.* **2013**, *42* (17), 7278–7288. https://doi.org/10.1039/C3CS35471G.

(13) Lendlein, A.; Jiang, H.; Jünger, O.; Langer, R. Light-Induced Shape-Memory Polymers. *Nat. 2005 4347035* **2005**, *434* (7035), 879–882. https://doi.org/10.1038/nature03496.

(14) Xie, T. Tunable Polymer Multi-Shape Memory Effect. *Nat. 2010 4647286* **2010**, *464* (7286), 267–270. https://doi.org/10.1038/nature08863.

(15) Goor, O. J. G. M.; Hendrikse, S. I. S.; Dankers, P. Y. W.; Meijer, E. W. From Supramolecular Polymers to Multi-Component Biomaterials. *Chem. Soc. Rev.* **2017**, *46* (21), 6621–6637. https://doi.org/10.1039/C7CS00564D.

(16) Del Barrio, J.; Horton, P. N.; Lairez, D.; Lloyd, G. O.; Toprakcioglu, C.; Scherman, O. A. Photocontrol over Cucurbit[8]Uril Complexes: Stoichiometry and Supramolecular Polymers. *J. Am. Chem. Soc.* **2013**, *135* (32), 11760–11763. https://doi.org/10.1021/ja406556h.

(17) Freeman, R.; Han, M.; Álvarez, Z.; Lewis, J. A.; Wester, J. R.; Stephanopoulos, N.; McClendon, M. T.; Lynsky, C.; Godbe, J. M.; Sangji, H.; Luijten, E.; Stupp, S. I. Reversible Self-Assembly of Superstructured Networks. *Science* **2018**, *362* (6416), 808–813. https://doi.org/10.1126/science.aat6141.

(18) Gu, Y.; Alt, E. A.; Wang, H.; Li, X.; Willard, A. P.; Johnson, J. A. Photoswitching Topology in Polymer Networks with Metal–Organic Cages as Crosslinks. *Nat. 2018 5607716* **2018**, *560* (7716), 65–69. https://doi.org/10.1038/s41586-018-0339-0.

(19) Wang, Y.; Gu, Y.; Keeler, E. G.; Park, J. V.; Griffin, R. G.; Johnson, J. A. Star PolyMOCs with Diverse Structures, Dynamics, and Functions by Three-Component Assembly. *Angew. Chemie* **2017**, *129* (1), 194–198. https://doi.org/10.1002/ange.201609261.

(20) Li, J. R.; Zhou, H. C. Bridging-Ligand-Substitution Strategy for the Preparation of Metalg-Organic Polyhedra. *Nat. Chem.* **2010**, *2* (10), 893–898. https://doi.org/10.1038/NCHEM.803.

(21) Eddaoudi, M.; Kim, J.; Wachter, J. B.; Chae, H. K.; O'Keeffe, M.; Yaghi, O. M. Porous Metal-Organic Polyhedra: 25 Å Cuboctahedron Constructed from 12 Cu2(CO2)4 Paddle-Wheel Building Blocks [17]. *Journal of the American Chemical Society*. American Chemical Society 2001, pp 4368–4369. https://doi.org/10.1021/ja0104352.

(22) Larsen, R. W. How Fast Do Metal Organic Polyhedra Form in Solution? Kinetics of [Cu 2(5-OH-Bdc)2L2]12 Formation in Methanol. *J. Am. Chem. Soc.* **2008**, *130* (34), 11246–11247. https://doi.org/10.1021/ja802605v.

(23) Klán, P.; Wirz, J. Photochemistry of Organic Compounds : From Concepts to Practice. **2009**, 563.

(24) Romero, N. A.; Nicewicz, D. A. Organic Photoredox Catalysis. *Chem. Rev.* **2016**, *116* (17), 10075–10166. https://doi.org/10.1021/ACS.CHEMREV.6B00057.

(25) Buono-Core, G.; Iwai, K.; Chow, Y. L.; Koyanagi, T.; Kaji, A.; Hayami, J.-I. Sensitized Photolysis of Bis(Acetylacetonato)Copper(II); General Reaction Pattern. *https://doi.org/10.1139/v79-002* **2011**, *57* (1), 8–16. https://doi.org/10.1139/V79-002.

(26) Chow, Y. L.; Buono-Core, G. E. Triplet-State Benzophenone-Sensitized Photoreduction of Bis(Acetylacetonato)Copper(II): The Generation and Stability of Copper(I) Complexes. *https://doi.org/10.1139/v83-146* **2011**, *61* (5), 795–800. https://doi.org/10.1139/V83-146.

(27) Bae, J.; Baek, K.; Yuan, D.; Kim, W.; Kim, K.; Zhou, H.-C.; Park, J. Reversible Photoreduction of Cu(<scp>ii</Scp>)–Coumarin Metal–Organic Polyhedra. *Chem. Commun.* **2017**, *53* (66), 9250–9253. https://doi.org/10.1039/C7CC04799A.

(28) Henglein, A. Formation and Absorption Spectrum of Copper Nanoparticles from the Radiolytic Reduction of Cu(CN)2-. *J. Phys. Chem. B* **2000**, *104* (6), 1206–1211. https://doi.org/10.1021/JP992950G.

(29) Gong, J. P. Why Are Double Network Hydrogels so Tough? *Soft Matter*. The Royal Society of Chemistry June 8, 2010, pp 2583–2590. https://doi.org/10.1039/b924290b.

(30) Sun, J. Y.; Zhao, X.; Illeperuma, W. R. K.; Chaudhuri, O.; Oh, K. H.; Mooney, D. J.; Vlassak, J. J.; Suo, Z. Highly Stretchable and Tough Hydrogels. *Nat. 2012 4897414* **2012**, *489* (7414), 133–136. https://doi.org/10.1038/nature11409.

(31) Mougin, A.; Repain, V.; Ferre, J.; Jamet, J. P.; Gierak, J.; Mailly, D.; Chappert, C.; Mathet, V.; Warin, P.; Chapman, J. N.; Magn, T.; Terris, D.; Folks, L.; Weller, D.; E Baglin, J. E.; Kellock, A. J.; Rothui-zen, H.; Vettiger, P.; Phys Lett, A.; Devolder, J. T.; Chen, Y.; Cambril, E.; Bernas, H.; Dietzel, A.; Berger, R.; Grimm, H.; Schug, C.; Bruenger, W. H.; Dzionk, C.; Letzkus, F.; Springer, R.; Loeschner, H.; Platzgummer, E.; Stengl, G.; An-ders, S.; Bandic, Z. Z.; Rettner, C. T.; Terris, B. D.; Eichhorn, H.; Boehm, M.; Adam, D.; Jian Ping Gong, B.; Katsuyama, Y.; Kurokawa, T.; Osada, Y.; Gong, J. P.; Katsuyama, Y.; Kurokawa, T.; Osada, Y.; Gong Presto, J. P. Double-Network Hydrogels with Extremely High Mechanical Strength. *Adv. Mater.* **2003**, *15* (14), 1155–1158. https://doi.org/10.1002/ADMA.200304907.

(32) Skardal, A.; Zhang, J.; McCoard, L.; Xu, X.; Oottamasathien, S.; Prestwich, G. D. Photocrosslinkable Hyaluronan-Gelatin Hydrogels for Two-Step Bioprinting. *Tissue Eng. - Part A* **2010**, *16* (8), 2675–2685. https://doi.org/10.1089/ten.tea.2009.0798.

(33) Pereira, R. F.; Bártolo, P. J. 3D Bioprinting of Photocrosslinkable Hydrogel Constructs. *Journal of Applied Polymer Science*. John Wiley and Sons Inc. December 1, 2015. https://doi.org/10.1002/app.42458.

(34) Liu, W.; Heinrich, M. A.; Zhou, Y.; Akpek, A.; Hu, N.; Liu, X.; Guan, X.; Zhong, Z.; Jin, X.; Khademhosseini, A.; Zhang, Y. S. Extrusion Bioprinting of Shear-Thinning Gelatin Methacryloyl Bioinks. *Adv. Healthc. Mater.* **2017**, *6* (12). https://doi.org/10.1002/adhm.201601451.

(35) Lee, B. H.; Shirahama, H.; Cho, N. J.; Tan, L. P. Efficient and Controllable Synthesis of Highly Substituted Gelatin Methacrylamide for Mechanically Stiff Hydrogels. *RSC Adv.* **2015**, *5* (128), 106094–106097. https://doi.org/10.1039/c5ra22028a.

(36) Lim, K. S.; Schon, B. S.; Mekhileri, N. V.; Brown, G. C. J.; Chia, C. M.; Prabakar, S.; Hooper, G. J.; Woodfield, T. B. F. New Visible-Light Photoinitiating System for

Improved Print Fidelity in Gelatin-Based Bioinks. *ACS Biomater. Sci. Eng.* **2016**, *2* (10), 1752–1762. https://doi.org/10.1021/acsbiomaterials.6b00149.

(37) Ouyang, L.; Highley, C. B.; Rodell, C. B.; Sun, W.; Burdick, J. A. 3D Printing of Shear-Thinning Hyaluronic Acid Hydrogels with Secondary Cross-Linking. *ACS Biomater. Sci. Eng.* **2016**, *2* (10), 1743–1751.

(38) Montheil, T.; Maumus, M.; Valot, L.; Lebrun, A.; Martinez, J.; Amblard, M.; Noël, D.; Mehdi, A.; Subra, G. Inorganic Sol-Gel Polymerization for Hydrogel Bioprinting. *ACS Omega* **2020**. https://doi.org/10.1021/acsomega.9b03100.

(39) Skardal, A.; Zhang, J.; Prestwich, G. D. Bioprinting Vessel-like Constructs Using Hyaluronan Hydrogels Crosslinked with Tetrahedral Polyethylene Glycol Tetracrylates. *Biomaterials* **2010**, *31* (24), 6173–6181. https://doi.org/10.1016/j.biomaterials.2010.04.045.

(40) Bertassoni, L. E.; Cecconi, M.; Manoharan, V.; Nikkhah, M.; Hjortnaes, J.; Cristino, A. L.; Barabaschi, G.; Demarchi, D.; Dokmeci, M. R.; Yang, Y.; Khademhosseini, A. Hydrogel Bioprinted Microchannel Networks for Vascularization of Tissue Engineering Constructs. *Lab Chip* **2014**, *14* (13), 2202–2211. https://doi.org/10.1039/c4lc00030g.

(41) Ouyang, L.; Highley, C. B.; Sun, W.; Burdick, J. A.; Ouyang, L.; Highley, C. B.; Burdick, J. A.; Sun, W. A Generalizable Strategy for the 3D Bioprinting of Hydrogels from Nonviscous Photo-Crosslinkable Inks. *Adv. Mater.* **2017**, *29* (8), 1604983.

(42) Echalier, C.; Levato, R.; Mateos-Timoneda, M. A.; Castaño, O.; Déjean, S.; Garric, X.; Pinese, C.; Noël, D.; Engel, E.; Martinez, J.; Mehdi, A.; Subra, G. Modular Bioink for 3D Printing of Biocompatible Hydrogels: Sol–Gel Polymerization of Hybrid Peptides and Polymers. *RSC Adv.* **2017**, *7* (20), 12231–12235. https://doi.org/10.1039/C6RA28540F.

(43) O'Bryan, C. S.; Bhattacharjee, T.; Niemi, S. R.; Balachandar, S.; Baldwin, N.; Ellison, S. T.; Taylor, C. R.; Sawyer, W. G.; Angelini, T. E. Three-Dimensional Printing with Sacrificial Materials for Soft Matter Manufacturing. *MRS Bull.* **2017**, *42* (8), 571–577. https://doi.org/10.1557/mrs.2017.167.

(44) Lee, A.; Hudson, A. R.; Shiwarski, D. J.; Tashman, J. W.; Hinton, T. J.; Yerneni, S.; Bliley, J. M.; Campbell, P. G.; Feinberg, A. W. 3D Bioprinting of Collagen to Rebuild Components of the Human Heart. *Science* **2019**, *365* (6452), 482–487. https://doi.org/10.1126/science.aav9051.

(45) Shi, L.; Carstensen, H.; Hölzl, K.; Lunzer, M.; Li, H.; Hilborn, J.; Ovsianikov, A.; Ossipov, D. A. Dynamic Coordination Chemistry Enables Free Directional Printing of Biopolymer Hydrogel. *Chem. Mater.* **2017**, *29* (14), 5816–5823. https://doi.org/10.1021/acs.chemmater.7b00128.

(46) Hsiao, L. C.; Badruddoza, A. Z. M.; Cheng, L. C.; Doyle, P. S. 3D Printing of Self-Assembling Thermoresponsive Nanoemulsions into Hierarchical Mesostructured Hydrogels. *Soft Matter* **2017**, *13* (5), 921–929. https://doi.org/10.1039/C6SM02208A.

(47) Hong, S.; Sycks, D.; Chan, H. F.; Lin, S.; Lopez, G. P.; Guilak, F.; Leong, K. W.; Zhao, X. 3D Printing of Highly Stretchable and Tough Hydrogels into Complex, Cellularized Structures. *Adv. Mater.* **2015**, *27* (27), 4035–4040. https://doi.org/10.1002/adma.201501099.

(48) Adzima, B. J.; Tao, Y.; Kloxin, C. J.; DeForest, C. A.; Anseth, K. S.; Bowman, C. N. Spatial and Temporal Control of the Alkyne–Azide Cycloaddition by Photoinitiated Cu(II) Reduction. *Nat. Chem. 2011 33* **2011**, *3* (3), 256–259. https://doi.org/10.1038/nchem.980.